

TEMPORAL ASYMMETRY OF FLUCTUATIONS IN NONEQUILIBRIUM
STEADY STATES

by

Carlo Paneni

School of Biomolecular and Physical Sciences

Nanoscale Science and Technology Centre

Faculty of Science, Environment, Engineering and Technology

GRIFFITH UNIVERSITY

Brisbane, Australia

A THESIS

SUBMITTED IN FULFILMENT OF THE REQUIREMENTS OF THE DEGREE
OF DOCTOR OF PHILOSOPHY

April 2007

GRIFFITH UNIVERSITY

Nanoscale Science and Technology Centre

This work has not previously been submitted for a degree or diploma in any university. To the best of my knowledge and belief, the thesis contains no material previously published or written by another person except where due reference is made in the thesis itself.

Carlo Paneni

Nanoscale Science and Technology Centre
School of Biomolecular and Physical Sciences

Abstract

We conduct a comprehensive and systematic study of the temporal asymmetries of the fluctuations in properties of nonequilibrium, deterministic and reversible systems. Our motivation stems from the theories that predict asymmetry of fluctuation paths in stochastic dynamics. However, stochastic descriptions are an approximation in the sense that real systems obey deterministic reversible dynamics (at the classical level). In order to understand if the predicted asymmetry is an artifact of the stochastic model, we consider the results from studies of deterministic reversible systems composed of many particles.

In order to examine these systems we used molecular dynamics simulations. We thoroughly investigate the presence of temporal asymmetry in the fluctuations of various properties in nonequilibrium, microscopic simulated systems, which are reversible and deterministic. We consider systems undergoing steady state Couette shear flow, and colour diffusion.

For the first time we provide light on the particular path by which irreversibility emerges from microscopic reversible dynamics out of equilibrium. Asymmetry appears to be more accentuated in the larger the fluctuations.

To assess the generality of temporal asymmetries in such deterministic systems, we consider identification of temporal asymmetries using differences of cross correlation functions: we establish from theoretical arguments and numerical evidence that a microscopic system undergoing colour diffusion exhibits asymmetry in a number of cross correlation functions. Furthermore we prove that some particular cross correlation functions have necessarily to be symmetric for a reversible and deterministic system to be regarded as “physical”.

We then demonstrate how to mathematically express the fluctuation paths as a correlation function. We verify with strong numerical evidence that this equivalence holds for a simulated system. In light of this link between the asymmetry of correlation functions and that of fluctuation paths, we explain the presence of asymmetry in fluctuation paths via the transient time correlation formalism. We therefore give the first theoretical justification of the emergence of asymmetry in the fluctuations of microscopic deterministic and reversible systems.

In this manner we are able to provide a sound theory to explain and characterize asymmetries in the fluctuations of mesoscopic systems. Finally we briefly outline possible future research directions.

Acknowledgments

First of all, I would like to thank my supervisor, A/Prof. Debra Bernhardt. She has been the best advisor and teacher I could have wished for. She has been instrumental in every phase of this work, due to her knowledge and ability. I could not have hoped for a better mentor for my doctorate – her kindness, attention, guidance and encouraging assistance have constituted the most precious support.

I would like to express my gratitude and appreciation to A/Prof. Lamberto Rondoni, who has provided support, insight and guidance constantly during this research. His scientific ideas have been a fundamental element in carrying out this project. His kindness and his generous assistance have guided me throughout these three years, and have helped the research to reach unanticipated results.

I would like to acknowledge and thank the following people for their help:

A/Prof. Peter J. Daivis and Prof. John F. Dobson for useful comments and invaluable suggestions.

Sarah Brookes for the assistance in the work.

Dr Andrej Panjkov, Dr Stephen R. Williams, Prof Denis J. Evans, Emil Mittag and Dr Owen G. Jepps, from whom I have learnt a great deal.

Dr Owen G. Jepps (again) and Benjamin V. Cuning, for proofreading various chapters of this thesis, and particular to Ben for his efforts and assistance in putting together the manuscript.

Dr Peter J. Johnston, my co-supervisor, for his support, and assistance in the layout of this work.

Dr. Genmiao Wang for his preliminary experimental tests.

All my friends and family for their support.

I would like to express my gratitude to Massimiliano Marianelli, whose wisdom has guided me to the decision to undertake this PhD, and whose friendship has accompanied me everyday.

Finally I want to thank my girlfriend Mina Ohara, for her loving support and for always being by my side.

Table of Contents

Statement of originality	ii
Abstract	iii
Table of Contents	vii
List of Tables.....	ix
List of Figures and Illustrations	x
 CHAPTER 1: INTRODUCTION	 1
1.1 Background	1
1.2 Influence of fluctuations in the development of nanoscale devices.....	7
1.3 Motivation	9
1.4 Thesis Organization	11
 CHAPTER 2: MOLECULAR DYNAMICS SIMULATIONS AND IDENTIFICATION OF FLUCTUATION PATHS	 14
2.1 General Features of Molecular Dynamics Simulations	14
2.1.1 Interaction Potential	14
2.1.2 Periodic boundary conditions	16
2.1.3 Force Field Nonequilibrium Molecular Dynamics	18
2.1.4 Thermostats.....	18
Couette Flow	22
Colour Diffusion	24
Fluctuation Paths	27
2.4.1 First Definition of Fluctuation Path	28
2.4.2 Second Definition of Fluctuation Path.....	31
Third Definition of Fluctuation Path	32
2.5 Average and most probable paths	37
 CHAPTER 3: INITIAL NUMERICAL EXPERIMENTS: SHEAR FLOW	 39
3.1 Selection of parameters for simulation study	39
3.1.1 Qualitative observation of asymmetry	46
3.2 Quantitative observation of asymmetry	60
3.3 Conclusions	79
 CHAPTER 4: INITIAL NUMERICAL EXPERIMENTS: COLOUR DIFFUSION	 81
4.1 Basic setup of the numerical experimental environment.	81
4.2 Numerical results	86
4.2.1 Fluctuation paths of colour flux	87
4.2.2 Pressure fluctuation paths	102
4.3 Conclusions	108
 CHAPTER 5: FLUCTUATION PATHS, CORRELATION FUNCTIONS AND NONLINEAR RESPONSE THEORY.	 110
5.1 Building of the fluctuation paths as cross correlation functions of symmetric properties.....	110
5.2 Properties of Correlation Functions.	113
5.3 Nonlinear response theory.....	118

5.4 Numerical Results	121
5.5 Conclusions	133
5.6 Appendix	134
CHAPTER 6: CONCLUSIONS.....	1388
REFERENCES.....	14040

List of Tables

Table 3-1 Means (μ) and standard deviations (σ) of shear stress (P_{xy}), pressure (P), Internal Energy (E) and potential energy (U) as a function of the shear stress (γ) from 10^5 time steps runs. Errors are given when available.	43
Table 4-1 Mean μ and standard deviation σ of colour flux J_x and pressure P from 10 runs of 5×10^5 time steps for different colour fields F_C	84
Table 5-1 Properties of correlation functions $C(z, t) = \langle A(z+t)B(z) \rangle$	114
Table 5-2 Mean μ and standard deviation σ of color current J_c from 10 runs with corresponding standard errors (three times the standard deviation of the means out of the runs).	122

List of Figures and Illustrations

Figure 2-1 Representation of periodic boundary conditions and minimum image convention.	17
Figure 2-2 Representation of shearing periodic boundaries and minimum image convention.	22
Figure 2-3 Illustration of construction of the peak fluctuation path (First Definition).	29
Figure 2-4 Illustration of construction of the peak and trough fluctuation paths (second definition).	33
Figure 2-5 Illustration of construction of the peak and trough fluctuation paths (third definition).	34
Figure 2-6 Construction of the fluctuation paths: troughs are converted to peaks.	35
Figure 2-7 Construction of the ensemble average fluctuation paths, averaging the fluctuation path centered in t_{STAT}	36
Figure 3-1 Average values of shear stress vs strain rate. The values of P_{xy} are obtained from simulations of at least 100 time units.	40
Figure 3-2 Sample values of shear stress (P_{xy}), pressure (P), Internal Energy (E) and potential energy (U) with shear stress γ equal to 1.	44
Figure 3-3 Sample values of shear stress (P_{xy}), pressure (P), Internal Energy (E) and potential energy (U) with shear stress γ equal to 3.	45
Figure 3-4 Histograms of shear stress (P_{xy}) peak and trough fluctuation paths at equilibrium ($\gamma = 0$) with a “bird’s eye” view parallel to the frequency axis, using the first definition of fluctuation path. The colours in the legend refer to the values of ϕ . The gold line is a line through the ridge of the histograms. .	49
Figure 3-5 Histograms of shear stress (P_{xy}) peak and trough fluctuation paths at equilibrium ($\gamma = 0$) with a “bird’s eye” view parallel to the frequency axis, using the second definition of fluctuation path. The colours in the legend refer to the values of ϕ . The gold line is a line through the ridge of the histograms.	50
Figure 3-6 Histogram of shear stress (P_{xy}) trough fluctuation paths for various strain rates ($\gamma=0, 1, 2, 3$) using the first definition of fluctuation path. The colours in the legend refer to the values of ϕ . The gold line is a line through the ridge of the histograms.	51

- Figure 3-7 Histograms of shear stress (P_{xy}) trough fluctuation paths: synoptic plot for $\gamma = 0, 1, 2, 3, 4$ with “bird’s eye” view parallel to the frequency axis, using the first definition of fluctuation path. The colours in the legend refer to the values of φ . The gold line is a line through the ridge of the histograms. 52
- Figure 3-8 Histogram of shear stress (P_{xy}) trough fluctuation paths for various strain rates ($\gamma=0, 1, 2, 3$) using the second definition of fluctuation path. The colours in the legend refer to the values of φ . The gold line is a line through the ridge of the histograms. 54
- Figure 3-9 Histograms of shear stress (P_{xy}) trough fluctuation paths for $\gamma = 0, 1, 2, 3, 4$ with “bird’s eye” view parallel to the frequency axis, using the second definition of fluctuation path. The colours in the legend refer to the values of φ . The gold line is a line through the ridge of the histograms. 55
- Figure 3-10 Histograms of internal energy E peak fluctuation paths: synoptic plot for $\gamma = 0, 1, 2, 3, 4$ with a “bird’s eye” view parallel to the frequency axis, using the first definition of fluctuation path. The colours in the legend refer to the values of φ . The gold line is a line through the ridge of the histograms. 57
- Figure 3-11 Histograms of potential energy U first definition peak fluctuation paths: synoptic plot for $\gamma = 0, 1, 2, 3, 4$ with a “bird’s eye” view parallel to the frequency axis. The colours in the legend refer to the values of φ . The gold line is a line through the ridge of the histograms. 58
- Figure 3-12 Histograms of first definition pressure p peak fluctuation paths: synoptic plot for $\gamma = 0, 1, 2, 3, 4$ with “bird’s eye” view parallel to the frequency axis. The colours in the legend refer to the values of φ . The gold line is a line through the ridge of the histograms. 59
- Figure 3-13 Average and most probable (the crest of the previous histograms) fluctuation paths of shear stress for various fields (first definition)..... 61
- Figure 3-14 Measure of asymmetry of average and most probable fluctuation paths of shear stress for various fields (first definition). 61
- Figure 3-15 Average (A) and most probable (B) fluctuation path of shear stress P_{xy} with $T_{hr} = \mu - 2.5\sigma$. These are averages of 10 runs with error bars given by the standard error in the mean (which are often so small that they are not distinguishable in the plot). 63
- Figure 3-16 α_t of average (A and C) and most probable (B and D) FP of shear stress P_{xy} with $T_{hr} = \mu - 2.5\sigma$. These are averages of 10 runs with error bars

given by the standard error in the mean (which are often so small that they are not distinguishable in the plot).	64
Figure 3-17 Construction of the second definition peak fluctuation path with reference to t_d and t_r	65
Figure 3-18 Autocorrelation function for the shear stress P_{xy} . These are averages of 10 runs with error bars given by the standard error in the mean (which are often so small that they are not distinguishable in the plot).	66
Figure 3-19 $\langle \delta_t \rangle$ of average fluctuation path of shear stress P_{xy} with $T_{hr} = \mu - 2.5\sigma$ in linear regime. These are averages of 10 runs with error bars given by the standard error in the mean (which are often so small that they are not distinguishable in the plot).	67
Figure 3-20 $\langle \delta_t \rangle$, with $t=0.05$ of average fluctuation path of shear stress P_{xy} with $T_{hr} = -2.5\sigma + \mu$ (red circles) and $T_{hr} = -1.5\sigma + \mu$ (orange squares) vs the shear flow γ , in the linear regime. The values of $\langle \delta_t \rangle$ for a threshold equal to -4.4 are shown as green diamonds.	68
Figure 3-21 Average fluctuation path of P_{xy} together with its profile with the periodic oscillations due to the shearing boundaries removed for $\gamma = 1$ (A) and their α_t 's (B).	71
Figure 3-22 Average fluctuation path of P_{xy} together with its profile with the periodic oscillations due to the shearing boundaries removed for $\gamma = 2$ (A), $\gamma = 3$ (B) and $\gamma = 4$ (C).	72
Figure 3-23 α_t of average fluctuation path of P_{xy} together with its profile with the periodic oscillations due to the shearing boundaries removed, for various high fields.	73
Figure 3-24 Average (A) and most probable (B) fluctuation path of shear stress P_{xy} with $T_{hr} = \mu - 1.5\sigma$. These are averages of 10 runs with error bars given by the standard error in the mean (which are often so small that they are not distinguishable in the plot).	74
Figure 3-25 α_t of Average (A) and most probable (B) fluctuation path of shear stress P_{xy} with $T_{hr} = \mu - 1.5\sigma$. These are averages of 10 runs with error bars given by the standard error in the mean (which are often so small that they are not distinguishable in the plot).	75
Figure 3-26 Average fluctuation path of pressure p , with $T_{hr} = \mu + 2.5\sigma$. These are averages of 10 runs with error bars given by the standard error in the mean (which are often so small that they are not distinguishable in the plot). ...	76

- Figure 3-27 α_t of Average fluctuation path of pressure p with $T_{hr} = \mu + 2.5\sigma$.
 These are averages of 10 runs with error bars given by the standard error in the mean (which are often so small that they are not distinguishable in the plot).. A shows the equilibrium and high field values, while B shows samples of linear regime). 76
- Figure 3-28 Maximum frequency value peak fluctuation path of pressure p , with $T_{hr} = \mu + 2.5\sigma$. These are averages of 10 runs with error bars given by the standard error in the mean (which are often so small that they are not distinguishable in the plot). 77
- Figure 3-29 α_t of Most probable fluctuation path of pressure P ($T_{hr} = \mu + 2.5\sigma$).
 These are averages of 10 runs with error bars given by the standard error in the mean (which are often so small that they are not distinguishable in the plot). A shows high values of γ , B the linear regime..... 78
- Figure 3-30 δ_t , with $t=0.05$ of average fluctuation path of pressure P with $T_{hr} = 2.5\sigma - \mu$ (red circles) and $T_{hr} = 1.5\sigma - \mu$ (red circles) vs the shear flow γ , in the linear regime. The lines are linear fits through the data showing a γ^2 dependence of δ_t 79
- Figure 4-1 A) Average values of colour flux J_x vs colour field F_C . B) A closer view of the linear regime. The values of J_x are obtained from 10 sets of simulations of $5 \cdot 10^5$ time steps each. Error bars equal to the standard deviation out of the ten runs are plotted, but are generally too small to be seen on the graph. The dashed line is a least squares fit through the data for $F_C = 0, 1, 2, 3$. It has a regression coefficient of 0.99289 83
- Figure 4-2 Sample values of colour flux J_x with colour field $F_C=0, 1, 2, 3, 5$ 85
- Figure 4-3 Sample values of pressure P with colour field $F_C=0, 1, 2, 3, 5$ 86
- Figure 4-4 Histograms of colour flux (J_x) peak and trough fluctuation paths at equilibrium $F_C=0$ with threshold T_{hr} set to 2.5 times the standard deviation below and above the mean with a “bird’s eye” view parallel to the frequency axis. The colours in the legend refer to the values of $\log_{10}(\varphi)$. The gold line is a line through the ridge of the histograms. 88
- Figure 4-5 Histogram of colour flux (J_x) peak fluctuation paths for $F_C=0, 1, 2, 3$ with threshold $T_{hr}=\mu+2.5\sigma$. The colours in the legend refer to the values of $\log_{10}(\varphi)$. The gold line is a line through the ridge of the histograms. 89
- Figure 4-6 Histograms of colour flux (J_x) peak fluctuation paths with $F_C = 0, 1, 2, 3, 5$, threshold $T_{hr} = +\mu - 2.5\sigma$, with a “bird’s eye” view

parallel to the frequency axis. The colours in the legend refer to the values of $\log_{10}(\varphi)$. The gold line is a line through the ridge of the histograms..... 90

Figure 4-7 Most probable fluctuation path of colour flux J_x with $T_{hr} = \mu + 2.5\sigma$. These are averages of 10 runs with error bars given by the standard error in the mean. 91

Figure 4-8 Average fluctuation path of colour flux J_x with $T_{hr} = \mu + 2.5\sigma$. These are averages of 10 runs with error bars given by the standard error in the mean (which are often so small that they are not distinguishable in the plot). ... 92

Figure 4-9 $\langle \delta_t \rangle$ of average fluctuation path of J_x with $T_{hr} = \mu + 2.5\sigma$. These are averages of 10 runs with error bars given by the standard error in the mean (which are often so small that they are not distinguishable in the plot)..... 93

Figure 4-10 α_t of most probable fluctuation path of J_x with $T_{hr} = \mu + 2.5\sigma$. These are averages of 10 runs with error bars given by the standard error in the mean. 94

Figure 4-11 α_t of average fluctuation path of J_x with $T_{hr} = \mu + 2.5\sigma$. These are averages of 10 runs with error bars given by the standard error in the mean (which are often so small that they are not distinguishable in the plot)..... 95

Figure 4-12 Autocorrelation function $C(J_x, t) = \langle J_x(\Gamma) J_x(S'\Gamma) \rangle$ for colour flux J_x . These are averages of 10 runs with error bars given by the standard error in the mean (which are often so small that they are not distinguishable in the plot). 97

Figure 4-13 δ_t , with $t=0.05$ of average fluctuation path colour flux J_x with $T_{hr} = 2.5\sigma + \mu$ (red circles) and $T_{hr} = -2.5\sigma + \mu$ (orange squares) in function of the colour field F_C , in the linear regime..... 98

Figure 4-14 Histograms of colour flux (J_x) trough fluctuation paths for $F_C = 0, 1, 2, 3, 5$ with threshold $T_{hr} = \mu - 2.5\sigma$, with a “bird’s eye” view parallel to the frequency axis. The colours in the legend refer to the values of $\log_{10}(\varphi)$. The gold line is a line through the ridge of the histograms..... 99

Figure 4-15 Average (A) and most probable (B) trough fluctuation path of colour flux J_x , with $T_{hr} = \mu - 2.5\sigma$. These are averages of 10 runs with error bars given by the standard error in the mean. 100

Figure 4-16 α_t of Average (A) and most probable (B) fluctuation path of colour field J_x with $T_{hr} = \mu - 2.5\sigma$. These are averages of 10 runs with error bars given by the standard error in the mean (which are often so small that they are not distinguishable in the plot). 101

- Figure 4-17 Histograms of pressure P peak fluctuation paths for $\gamma=0, 1, 2, 3, 4$ with a “bird eye” view parallel to the frequency axis. The colours in the legend refer to the values of $\log_{10}(\varphi)$. The gold line is a line through the ridge of the histograms. 102
- Figure 4-18 Maximum frequency value peak fluctuation path of pressure P, with $T_{hr} = \mu + 2.5\sigma$ $T_{hr} = \mu - 2.5\sigma$. These are averages of 10 runs with error bars given by the standard error in the. 103
- Figure 4-19 α_t of Most probable fluctuation path of pressure P with $T_{hr} = \mu + 2.5\sigma$ as averages of 10 runs with error bars. $T_{hr} = \mu - 2.5\sigma$. These are averages of 10 runs with error bars given by the standard error in the mean (which are often so small that they are not distinguishable in the plot). . 104
- Figure 4-20 Average fluctuation path of pressure P, with $T_{hr} = \mu + 2.5\sigma$ These are averages of 10 runs with error bars given by the standard error in the mean (which are often so small that they are not distinguishable in the plot). 105
- Figure 4-21 α_t of average fluctuation path of pressure P with $T_{hr} = \mu + 2.5\sigma$ These are averages of 10 runs with error bars given by the standard error in the mean (which are often so small that they are not distinguishable in the plot). 106
- Figure 4-22 $\langle \delta_t \rangle$, with $t=0.05$ of average fluctuation path of pressure P with $T_{hr} = 2.5\sigma + \mu$ as a function of the square of the colour field F_c in the linear regime. The line is a linear fit through the data showing linear dependence of $\langle \delta_t \rangle$ on F_c^2 107
- Figure 5-1 A schematic illustration of the existence of asymmetry in systems where correlations decay and $\left. \frac{d^n C(z,t)}{dt^n} \right|_{z,t=0} \neq 0$, for any of $n = 1, 3, 5, \dots$ 117
- Figure 5-2 A: Average fluctuation path of the color current from 10 steady state runs with error bars (equal to the standard deviation of the means). B: δ_t for the average fluctuation path of the color current from 10 runs with error bars (equal to the standard error of the mean). 123
- Figure 5-3 Cross correlation function of color current J_c and pressure P obtained from an average of 10 runs with error bars (equal to the standard error of the mean) with color field $F_c=2$. B: Comparison between the profile of the cross correlation with $F_c=2$ and with $F_c=0$, that is at equilibrium, where the profile is constantly equal to zero. C: Coefficient of asymmetry X_t^{ODD} , for $F_c=2$, that shows asymmetry out of equilibrium. 125

- Figure 5-4 Autocorrelation function of color current J_c average of 10 runs with error bars (equal to the standard error of the mean) with color field F_c 127
- Figure 5-5 Values of $X(z, t)$, which measures the departure of the cross correlation function $C_{J_c, J_c}(z+t) = \langle J_c(z) J_c(z+t) \rangle$ from symmetric behaviour, and values of X_t^{ODD} which measures the departures from anti-symmetric behaviour of $C_{J_c, \dot{J}_c}(z+t) = \langle J_c(z) \dot{J}_c(z+t) \rangle$ and $C_{J_c, P}(z+t) = \langle J_c(z) P(z+t) \rangle$. All data are computed as average of 10 runs with error bars (equal to the standard error of the mean) with color field $F_c = 2$ 128
- Figure 5-6 Correlation function of color current J_c with its derivative as average of 10 runs with error bars (equal to the standard error of the mean) with color field $F_c=2$ 129
- Figure 5-7 The values of $\langle \delta_t \rangle$ of the average fluctuation path of color current as averages of 10 transient runs with error bars (equal to the standard error of the mean), calculated using the right hand side of equation (5.1.11) with $z=3$, and compared to the value obtained using a steady state expression..... 131
- Figure 5-8 $\langle \delta_t \rangle$ as a function of the field F_c at arbitrary time $t = 0.1$ close to the peaks of the $\langle \delta_t \rangle$, with $T_{hr} = \mu + 2.5\sigma$. Error bars are equal to the standard error out of the 10 runs. 132
- Figure 5-9 A: $\langle \delta_t \rangle$ of fluctuation path with $T_{hr} = \mu + 2.5\sigma$ for various N . B: $\langle \delta_t \rangle$ at arbitrary time $t=0.1$ close to the peaks of the $\langle \delta_t \rangle$'s. These are averages of 4 runs with error bars given by the standard error in the mean.....133

Chapter One: INTRODUCTION

1.1 Background

In contrast to theories of equilibrium systems, there are many aspects of nonequilibrium processes that are not thoroughly understood. Nonequilibrium statistical mechanics aims to provide a better insight into such nonequilibrium phenomena. One important task is to provide a deeper insight into irreversibility, that is in the emergence of irreversible behaviour in gross systems that are composed of molecules driven by reversible dynamics. It is an issue that has captured interest since the dawn of statistical mechanics [1]: whilst loosely embedded in a fundamental and implicit sense since the conception of statistical mechanics, the understanding of irreversibility is still being refined [2-5].

The understanding of how irreversibility emerges from reversible dynamics has become even more relevant, driven by the development of novel powerful numerical and experimental tools and with the finer detailing demanded by nanoscale science. For example fluctuations that have been predicted in studies of the emergence of irreversibility [6], and are not observable in the thermodynamic limit, become observable over measurable periods of time in small systems [7] [8]. This fact has been shown to have consequences in the mechanisms of action of molecular machines, and the manipulation of biomolecules [9-13].

Classical thermodynamics proves to be an inadequate framework to explain the emergence of irreversibility and to describe nonequilibrium systems. A classic

thermodynamic description, which is concerned with the energy exchange processes of macroscopic systems at equilibrium, neglects fluctuations, which are generally negligible in macroscopic systems. It is only under specific conditions that fluctuations have to be taken into account to describe phenomena of macroscopic systems. This is the case of the opalescence of light in a fluid at its critical point and of the blue color of the sky, which is a result of light scattering [14]. As a system's dimensions decrease, fluctuations need to be taken into account to provide an adequate model of the system. Specifically, in a nonequilibrium microscopic system, fluctuations explain and imply phenomena that may be in contradiction with the gross thermodynamic description.

The recent development of the powerful computational tool of nonequilibrium molecular dynamics simulations has provided a numerical-experimental framework to directly access nonequilibrium microscopic systems. This instrument allows the validation of theories by directly providing positions and momenta of the molecules that form the microscopic system; coordinates that, due to practical issues, are not feasible to obtain from a real –as opposed to computer simulated– experiment. As a consequence of the progresses of nonequilibrium simulation techniques, in particular through the implementation of artificial thermostats [15-19], molecular dynamics simulations have allowed the modelling of nonequilibrium steady states, in which the systems under investigation are driven out of equilibrium under the effect of an external field. This field does work on the system and would cause it to continually heat up; however the steady state is obtained by appropriate elimination of heat from

the system, which, in a computer simulation, is achieved by the effect of artificial thermostats.

In this context a milestone such as the fluctuation theorems (FT) [20] has been achieved and has pushed research into novel directions [6,8,11-13,21-29]. For the first time the ratio between the probability of a trajectory and its time reversal has been quantified. Intuitions that underpinned the very roots of the development of statistical mechanics since the time of Boltzmann have for the first time been translated into an exact mathematical formula, furthering comprehension of irreversibility at the molecular level.

Thanks to the modern manipulation technology, such as optical tweezers, the fluctuation theorem and some related theories have been experimentally tested [7,8,11-13].

In this quest for a more accurate and theoretically sound understanding of the emergence of irreversibility from microscopic deterministic and reversible dynamics, interest has been focused on exceptional fluctuations. Despite occurring rarely, large fluctuations are responsible for many physical processes, such as earthquakes, nucleation at phase transitions, mutations in DNA sequences, and failures of electronic devices [30,31] and can shed some light on the emergence of the irreversible behaviour of macroscopic systems from reversible microscopic dynamics. Referring to [30,31], the interest towards the study of exceptional fluctuations has risen in consideration of the recent discovery of the potential creative role large fluctuations can assume: they can be exploited to enhance signals in nonlinear systems and improve signal processing through stochastic resonance [32-34] and give

rise to unidirectional transport in periodic structures (ratchets) [35-37,38]. Then followed the development of a broad theoretical framework to deal with exceptional fluctuations in stochastic systems, known as large deviation theory [39-49].

In particular, theories for nonequilibrium thermodynamic stationary states [50,51] predict a break in symmetry in the exceptional fluctuations towards and away from a nonequilibrium steady state for stochastic systems. That is, it can be shown that for properties that fluctuate, there will be a different time dependence as the property rises to a peak value, than there is as it departs from this value [52-54]. This is referred to as time asymmetry, or temporal asymmetry.

Onsager [55,56] predicted a relationship between the fluctuations in equilibrium systems and the decay paths for systems relaxing from a nonequilibrium initial state near equilibrium. Onsager and Machlup extend that work to consider paths between nonequilibrium states [57,58]. These theories assume that the fluctuations are Gaussian and therefore symmetric. More recently various approaches have been used to extend Onsager-Machlup fluctuation theory to the nonequilibrium and non-linear domain [59-65]. In this case the fluctuations are predicted to be asymmetric.

Ultimately the development of such extensions revolves around the break down of the principle of detailed balance out of equilibrium; the principle regards stochastic systems and requires that the transition between any two states takes place with equal frequency in either directions at equilibrium [66]. The principle of detailed balance does not apply to nonequilibrium steady states: it is shown not to hold for examples of stochastic systems [67,68], and nonequilibrium extensions of it have been recently attempted [68].

All these fluctuation theories predict the emergence of asymmetry in the exceptional fluctuations of thermodynamic properties of nonequilibrium mesoscopic systems, modelled by stochastic processes. In particular, these theories lead to the introduction of a term in the "adjoint" hydrodynamic equations -the equations describing the fluctuations away from the nonequilibrium steady states-:

$$\partial_t \rho = \mathcal{D}^*(\rho) \quad (1.1)$$

which has no counterpart in the standard hydrodynamic equations -the equations describing the relaxation toward the nonequilibrium steady states:

$$\partial_t \rho = \mathcal{D}(\rho) \quad (1.2)$$

where \mathcal{D}^* is, in general, non local and different from $-\mathcal{D}$.

The mesoscopic theories apply to stochastic lattice gases that admit the hydrodynamic description. Such a theory is supposed to hold more generally, under some assumptions [51,69], if the mesoscopic evolution is given by a Markov process X_t , that represents the configuration of the system at time t .

Stochastically perturbed electrical circuits have been used as systems that are equivalent to a form of Brownian motion in a force field with weak white noise, and have provided experimental evidence of asymmetric fluctuations [70-80]. Yet the theories that predict asymmetry in exceptional fluctuations apply for stochastic systems, where the fluctuations are induced by white noise. Stochastic systems, such as forms of Brownian motion in a force field with weak white noise/ Langevin

dynamics, are effectively employed, but ultimately constitute an approximate –gross – description of aggregates of microscopic systems.

In order to really prove that such asymmetry in fluctuations should be a fairly ubiquitous feature of nonequilibrium fluctuations in nature, the following question should be addressed: would asymmetry in fluctuations of thermodynamic properties occur in models for microscopic systems, which are reversible and deterministic, and constitute the exact description of the basic constituents of matter?

In this attempt we were inspired by the work of [81]. Interest in verifying the presence of temporal asymmetry in deterministic and reversible systems is attested by other recent works [82,83].

Gamba and Rondoni consider this theory in the context of the nonequilibrium Lorentz gas [84]: a system that is deterministic and time reversible, but is chaotic.

The system consists of a two-dimensional lattice of hard scatterers and of non-interacting particles subject to a constant external force. The fluctuations of the current flow generated by a force field were examined. The experimental results appeared to be in contradiction with the stochastic theory, as no asymmetry in the macroscopic property fluctuation emerged. It is then reasonable to consider whether an analogous experiment, performed on a more realistic system would yield results that are consistent with the theory. The Lorentz gas in fact consists of hard particles, which could be regarded more as a set of independent experiments rather than a system composed of interacting particles.

Further to this question, it is not known whether fluctuations of thermodynamic fluxes other than mass current would match the theory. It is then unknown if other system properties, other thresholds and other forces would yield other results. There are then doubts regarding the adequacy of the current as a suitable environment for testing asymmetrical behaviours: the coupling of the effects of the necessary periodicity in space of the computer simulation and the homogeneity of the force driving the irreversible process of current flow could in principle have been taken into account to artificially force a symmetry of the fluctuations. Such a potential artificial symmetry could be avoided by focusing our attention on a model of a boundary driven process rather than on current flow. In fact real nonequilibrium experimental processes are boundary driven.

1.2 Influence of fluctuations in the development of nanoscale devices

Renewed interest in nonequilibrium statistical mechanics has developed in the recent years due to concurrent factors [14]: the fundamental motivation is the potential to understand, develop and ultimately exploit nanoscale devices. An example of microscopic systems that have garnered recent attention, owing to remarkable applications, are biological motors: these are systems that operate out of equilibrium and continuously dissipate energy and are responsible for converting chemical energy into work [10].

Nanoscale devices and systems behave differently to macroscopic systems, due in part to the significant effects of wall interactions [85]. Standard models of flow, e.g. Navier Stokes theory, no longer apply. Furthermore the systems of interest (see

above) are out of equilibrium and experience irreversible processes, and hence classical thermodynamics and equilibrium statistical mechanics are unsuitable to describe them. We therefore need to address the inadequacy of the traditional framework.

This capability and the desire to understand, develop and ultimately exploit nanoscale devices stem from two major technological and scientific achievements: the development of nonequilibrium molecular dynamics simulations and statistical mechanics, and the advancement of techniques to manipulate at the microscopic level.

Previously, the possibility of investigating the properties of small systems, such as their modalities of exchanging heat and work with their environment, was restricted by the absence of experimental methods. However the recent development of microscopic manipulation techniques has allowed a direct experimental access to nanoscale systems [7-10,86].

In this context, nonequilibrium statistical mechanics can advance the modelling of nonequilibrium processes. More specifically for our focus, emergence of temporal asymmetry in exceptional fluctuations could be responsible for a phenomenon of particular interest due to their potential technical and theoretical implications, such as the nonequilibrium current generation, as shown in references of [87]. Asymmetry in fluctuations of the noise (as all these theories regard stochastic systems, and asymmetry in fluctuations is driven by noise) can lead to net transport, even in absence of any other kind of asymmetry, in superconducting electronic devices [87]. Any symmetric noise, such as Gaussian noise, will not give rise to a net transport or to a net voltage. Yet dynamically asymmetric noise can do so. For example, temporal

asymmetry in voltage fluctuation should generate currents in superionic conductors.

As such, asymmetry in fluctuations can give rise to a net effect: reference [87]

suggests that such asymmetry in fluctuations should be a fairly ubiquitous feature of nonequilibrium fluctuations in nature.

1.3 Motivation

Our work aims to address the unanswered question: would asymmetry in fluctuations of thermodynamic properties occur in models for microscopic systems, which are reversible and deterministic, and constitute the exact description of the basic constituents of matter? In other words, is temporal asymmetry an artifact of a stochastic model, or is it a ubiquitous feature of real systems, that are deterministic and reversible?

The manifestation of asymmetry in these models is a manifestation of thermodynamic irreversibility. In this project we therefore start by verifying that such microscopic deterministic and reversible systems out of equilibrium exhibit temporal asymmetries in their fluctuations, as observed in the stochastic systems. This confirms that the asymmetry is not an artifact of the stochastic model and the stochastic (mesoscopic) description can therefore be seen as a reduced representation of the deterministic (microscopic) dynamics. In the attempt to establish a link between the microscopic and mesoscopic descriptions of matter, it is necessary to confirm that a globally irreversible behaviour can arise in systems formed by a great number of particles, that evolve according to reversible laws; the dynamics of the elementary constituents of matter are indeed reversible.

Furthermore, once the presence of temporal asymmetry is ascertained, it confirms, at least numerically, that fluctuations can give rise to a net effect in microscopic systems. In an effort to observe other manifestations of asymmetry in nonequilibrium deterministic and reversible systems and the generality of the phenomenon, we then consider the temporal asymmetry in cross correlation functions [61,88-94]. We show that there are choices of particular even functions, such as the correlation of a function with itself or with its derivative, for which it is possible to prove and show numerically that no asymmetry is present. On the other hand for other functions, as substantiated by our numerical results and confirmed by theory, the presence of asymmetry should be the general case. As well as considering temporal asymmetries in typical fluctuation paths, as was done previously [52,53,82], we also look at asymmetry in general time-correlation functions, i.e. we examine if Onsager-type relations, $\langle A(t)B(t-s) \rangle - \langle A(t)B(t+s) \rangle$, become nonzero out of equilibrium for these systems [67,95-98]. We provide some general arguments and present numerical results.

Ultimately, the drive towards the most significant part of this work, the proof of temporal asymmetry in nonequilibrium fluctuation, comes from [88]. In their formulation of a generalized Langevin equation for nonequilibrium steady states, the authors resort to a particular expression, in order to prove time reversal symmetry holds for the cross correlation function of a property with its derivative. This particular expression provided the formalism necessary to obtain our fundamental proof.

As, in general, nonequilibrium correlation functions are not symmetric about the time origin of the correlation function, we justify and explain the presence of temporal asymmetry in exceptional fluctuations via the transient time correlation function formalism. We are able to express fluctuation paths as a correlation function: due to this link between the asymmetry of correlation functions and that of fluctuation paths, we provide a sound argument to justify and characterize asymmetries in the fluctuations of mesoscopic systems. This allows us to prove that these asymmetries in fluctuation paths are not an artifact of the stochastic representation, but rather an intrinsic property of deterministic and reversible nonequilibrium systems that will be evident for systems of all magnitudes. Theoretically we prove that fluctuations can give rise to a net effect in nanoscale systems, as suggested by [87].

To substantiate our considerations, we resort once more to the use of nonequilibrium molecular dynamics simulations, which allows us to compute the global properties of physical systems by simulating the dynamics of their microscopic components.

1.4 Thesis Organization

The thesis is organised in six chapters. In this chapter we have provided a background and motivation for the problem we consider.

In Chapter two we describe Nonequilibrium Molecular Dynamics simulations: we describe the models that we put under scrutiny, Couette flow and colour diffusion [99]. Then we give the definitions of Fluctuation Path and explain how various

definitions can be taken account. At last we explain why attention is focused on average and, when computationally feasible, on most probable fluctuations.

Chapter 3 is an account of the initial experiments performed on systems undergoing shear stress in order to confirm the presence of temporal asymmetry in deterministic and reversible nonequilibrium system. Numerical results are presented for an extensive set of runs: fluctuations of shear stress, pressure, internal energy and potential energy are presented and their asymmetry is measured.

The paper that summarises these results is [52].

In Chapter 4 experiments are performed on the Weeks-Chandler-Andersen fluid in a nonequilibrium configuration analogue to that which provided negative results in the simulations of Gamba and Rondoni, that considered the asymmetry in fluctuations in the context of the nonequilibrium Lorentz gas under Colour Field. [81]. We analyze the fluctuations of the colour flux and of the pressure.

The simplified nature of the simulated system - composed of hard scatterers and of non-interacting particles- is taken into account to justify the unexpected result in [81].

The paper that summarises the results is [53].

Chapter 5 presents the most important and significant result of this project: we do not limit ourselves to an observation of a property that is predicted by stochastic reduced models of reality but we prove that asymmetry in fluctuation paths is an intrinsic characteristic of every system. Temporal asymmetries in correlation functions are observed. Their presence can be justified on the basis of requirements of “physically meaningful behaviour” of a system. Guided by these results, we express fluctuation

paths in form of correlation functions. The presence of temporal asymmetry of fluctuation paths, expressed as cross correlation functions, can be justified via transient time correlation function theory. Such justification rests on constituent properties of matter as this link between the asymmetry of correlation functions and that of fluctuation paths provides a sound theory to justify and characterize asymmetries in the fluctuations paths. This allows us to prove that these asymmetries in fluctuation paths are not an artifact of the stochastic representation, but an intrinsic property of deterministic and reversible nonequilibrium systems that will be evident in systems of all scales.

The paper that summarises the results is [54].

In chapter 6 we give a summary of the work and conclude highlighting the significance and possible applications of the work and the future developments.

Chapter Two: MOLECULAR DYNAMICS SIMULATIONS AND IDENTIFICATION OF FLUCTUATION PATHS

Nonequilibrium Molecular dynamics simulations have been carried out in order to identify temporal asymmetries. In this chapter we will describe nonequilibrium molecular dynamics simulations in sections 2.1, 2.2, and 2.3, and describe how we identify asymmetric paths by examination of fluctuation paths in sections 2.4, 2.4.2 and 2.4.3.

2.1 General Features of Molecular Dynamics Simulations

Molecular Dynamics (MD) simulations mimic nature and provide details of the dynamics of a system of particles that a natural experiment could not offer, often due to experimental inadequacies at the molecular level. They supply an exact description of the microscopic state of the system, that is, they supply the coordinates and momenta of all the constituent particles of the system and their behaviour as a function of time. This subsequently allows the thermodynamic properties of a system to be evaluated.

2.1.1 Interaction Potential

The nature of the interactions between the particles is selected by defining a potential.

The generic interaction potential of a system of molecules can be divided into terms depending on the coordinates of molecules grouped in different numbers:

$$V = \sum_i v_1(\mathbf{r}_i) + \sum_i \sum_{j>i} v_2(\mathbf{r}_i, \mathbf{r}_j) + \sum_i \sum_{j>i} \sum_{k>j>i} v_3(\mathbf{r}_i, \mathbf{r}_j, \mathbf{r}_k) + \dots \quad (2.1.1)$$

$\sum_i v_1(\mathbf{r}_i)$ expresses the effect of an external field whereas the subsequent terms

express the particle interactions.

The potential that has been employed to describe the particle interactions in this work is the Weeks-Chandler-Andersen potential [100]. This is a truncated form of the two-body Lennard-Jones potential:

$$V_{ij}^{LJ} = 4\varepsilon \left(\left(\sigma / r_{ij} \right)^{12} - \left(\sigma / r_{ij} \right)^6 \right) \quad (2.1.2)$$

where ε and σ are parameters that are specified for each particle i and j , r_{ij} is the separation between particle i and j . This selection provides a good model for some thermodynamic systems [85].

To obtain the Weeks-Chandler-Andersen potential, the Lennard-Jones potential is truncated at the position of minimum potential energy ($2^{1/6}\sigma$) and then shifted up such that the potential is zero at the cut-off radius:

$$V^{RLJ} = \begin{cases} V^{LJ}(r) + \varepsilon & r < r_{\min} \\ 0 & r_{\min} \leq r \end{cases} \quad (2.1.3)$$

where $r_{\min} = 2^{1/6}\sigma$ and $\varepsilon = -V^{LJ}(r_{\min})$.

The interactions are extremely short ranged and, as a result of this, the simulation takes significantly less CPU time than simulations of Lennard-Jones fluids. This selection also ensures that the potential and its first derivative are continuous.

This choice of interaction provides simple and efficient reversible dynamics. As long

as the dynamics are reversible, the specific nature is not of great relevance.

In the simulation studies, the dynamics are assumed to be classical. The forces on each particle are determined using this potential, and then the trajectories of the particles can be obtained by numerically integrating their equations of motion.

The size of the systems that can be simulated *via* MD is mainly limited by the computation time. With a small number of molecules (typically up to the order of 10^9), we have to simulate the behaviour of a macroscopic system (formed by numbers of molecules of the order of 10^{23}). Furthermore, since we wish to observe fluctuations, whose magnitude shrinks as $O\left(\frac{1}{\sqrt{N}}\right)$, we are restricted to quite small systems, in this work typically 10 to 100.

2.1.2 Periodic boundary conditions

Periodic boundary conditions are often introduced to make a small system more representative of a bulk system by removing boundary effects. The trajectories of the molecules are developed in an infinite bulk system formed by their periodically replicated images throughout space.

That is, we are studying a small sample which evolves as if it were surrounded by periodic images of itself. As the trajectory of a molecule develops in the original box, its periodic image in each replicated box evolves in the same way; when it leaves the original box it is replaced by one of its images, entering from the opposite face of the box.

To calculate the inter-particle force acting on a given particle in the primitive cell, the program detects the closest image of each of the other particles.

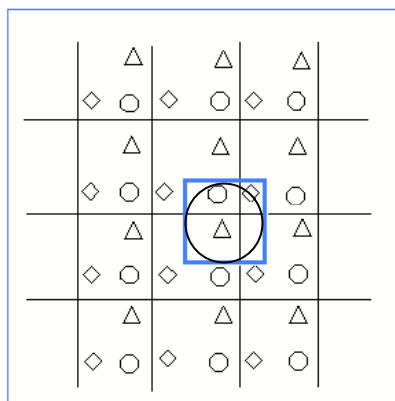


Figure 2-1 Representation of periodic boundary conditions and minimum image convention.

The closest image (or minimum image) of a particle can be inside the primitive cell or in one of the surrounding image cells (Figure 2-1).

Due to this periodic representation the range of the interactions must not exceed half the length of the elementary box, otherwise the images of the same particle could be taken into account more than once in the computation of the intermolecular forces.

This would introduce symmetries that are only due to the periodic boundary representation, and do not reflect any particular characteristics of a real thermodynamic system.

This is a simple model of a microscopic section of a bulk system. If a more accurate potential is selected, molecular dynamic simulations can provide results in agreement with experiments on real liquids as the number of particles in the primitive cell grows.

2.1.3 Force Field Nonequilibrium Molecular Dynamics

The generic system of particles subject to an external field is assumed to obey the dynamics given in the following equations [101], for force field nonequilibrium molecular dynamics:

$$\begin{aligned}\dot{\mathbf{q}}_i &= \frac{\mathbf{p}_i}{m_i} + \mathbf{C}_i F_e \\ \dot{\mathbf{p}}_i &= \mathbf{F}_i + \mathbf{D}_i F_e\end{aligned}\tag{2.1.4}$$

where F_e external field and \mathbf{C}_i and \mathbf{D}_i describe the coupling of the field to the system; \mathbf{q}_i are the laboratory coordinates of the particles; \mathbf{p}_i the peculiar momenta, that is the momenta relative to the streaming flow; \mathbf{F}_i forces on particle i due to the interaction with the other particles that form the liquid. The forces will do work on the system, causing it to heat

$$\dot{H}_0^{ad} = -JF_e V\tag{2.1.5}$$

where \dot{H}_0^{ad} is the heat production of the adiabatic system, V the volume and J the dissipative flux.

2.1.4 Thermostats

To obtain a steady state and avoid a constant heating of the system, it is necessary to extract this heat. If we were able to extract it in a reversible way, with a ‘large’ reservoir constantly in thermal equilibrium with the fluid, we would obtain Q^{rev} , that is the production of entropy. This reversible extraction of heat with a ‘large’ reservoir

in perpetual thermal equilibrium with the fluid, is mimicked by the effects of the artificial thermostats [15,17-19,102]. In the simulations performed here the Gaussian isokinetic thermostat is used, which keeps the kinetic temperature fixed. At equilibrium, the thermodynamic temperature, defined as:

$$\frac{1}{T} = \left. \frac{\partial S}{\partial U} \right|_{N,V} \quad (2.1.6)$$

and the kinetic temperature, defined as

$$\frac{d}{2} N k_B T = \frac{1}{2} \sum_{i=1}^N \frac{\mathbf{p}_i \cdot \mathbf{p}_i}{m_i} \quad (2.1.7)$$

are equivalent. It is not possible to state this out of equilibrium, except by postulating the local thermodynamic equilibrium: an approximation that may not be appropriate. Holding the kinetic temperature constant nevertheless fixes a convenient operational state variable so as to obtain a steady state [101]. The equations of motions are modified by the introduction of a damping term $\zeta \mathbf{p}_i$ in the following way:

$$\begin{aligned} \dot{\mathbf{q}}_i &= \frac{\mathbf{p}_i}{m_i} + \mathbf{C}_i F_e \\ \dot{\mathbf{p}}_i &= \mathbf{F}_i + \mathbf{D}_i F_e - \zeta \mathbf{p}_i \\ \zeta &= \frac{\sum_i \frac{\mathbf{F}_i \cdot \mathbf{p}_i}{m_i}}{\sum_i \frac{\mathbf{p}_i^2}{m_i}} + \frac{\sum_i \frac{\mathbf{D}_i \cdot \mathbf{p}_i}{m_i}}{\sum_i \frac{\mathbf{p}_i^2}{m_i}} F_e \end{aligned} \quad (2.1.8)$$

These equations of motion can be derived using Gauss' principle of least constraint [16,103]. Gauss' principle states that the trajectories actually followed by a conservatively constrained system are those which deviate as little as possible, in a

least square sense, from the unconstrained Newtonian trajectories. Provided the positions and velocities of a system are given, the actual accelerations are the ones that minimize the square of the curvature; or alternatively the ones that minimize the reactive forces. We show how these equations of motion are derived using Gauss' principle of least constraint [16,103], forcing the trajectories to deviate as little as possible, in a least square sense, from the unconstrained Newtonian trajectories. The constraint function for kinetic temperature can be written:

$$g(\mathbf{q}, \mathbf{p}, t) = \sum_{i=1}^N \frac{1}{2m_i} \mathbf{p}_i \cdot \mathbf{p}_i = K_0 \quad (2.1.8)$$

Differentiated with respect to time, it becomes:

$$G(\mathbf{q}, \mathbf{p}, \dot{\mathbf{p}}, t) = \sum_{i=1}^N \frac{1}{m_i} \mathbf{p}_i \cdot \dot{\mathbf{p}}_i = 0 \quad (2.1.9)$$

We minimize the curvature $\frac{1}{2} \left(\sum_{i=1}^N \dot{\mathbf{p}}_i - \mathbf{F}_i - \mathbf{D}_i F_e \right)^2$ with respect to the acceleration:

$$\sum_{k=1}^N \frac{\partial}{\partial \dot{\mathbf{p}}_k} \frac{1}{2} \left(\sum_{i=1}^N \dot{\mathbf{p}}_i - \mathbf{F}_i - \mathbf{D}_i F_e \right)^2 \cdot d\dot{\mathbf{p}}_k = 0 \quad (2.1.10)$$

and obtain:

$$\sum_{i=1}^N (\dot{\mathbf{p}}_i - \mathbf{F}_i - \mathbf{D}_i F_e) \cdot d\dot{\mathbf{p}}_i = 0 \quad (2.1.11)$$

where the $d\dot{\mathbf{p}}_i$ are not independent, as constrained by equation (2.1.8).

Differentiating the constraint equation (2.1.9) with respect to all the $\dot{\mathbf{p}}_i$, and summing, we have:

$$\sum_{i=1}^N \frac{1}{m_i} \mathbf{p}_i \cdot d\dot{\mathbf{p}}_i = 0 \quad (2.1.12)$$

We multiply equation (2.1.12) by an arbitrary coefficient ς , for simplicity assume m_i is the same for all i , and add it to equation (2.1.11) to obtain:

$$\sum_{i=1}^N (\dot{\mathbf{p}}_i - \mathbf{F}_i - \mathbf{D}_i F_e + \varsigma \mathbf{p}_i) \cdot d\dot{\mathbf{p}}_i = 0 \quad (2.1.13)$$

Due to the presence of the arbitrary Lagrange multiplier ς we can now write, for every i :

$$\dot{\mathbf{p}}_i - \mathbf{F}_i - \mathbf{D}_i F_e + \varsigma \mathbf{p}_i = 0 \quad (2.1.14)$$

So we take the dot-product of (2.1.14) with \mathbf{p}_i , sum over all i and substitute it into (2.1.9), and we can see that the Lagrange multiplier is the Gaussian thermostat for a system where m_i all are the same, and is consistent with equations

Error! Reference source not found.. The trajectories actually followed by our system are therefore those which deviate as little as possible, in a least square sense, from the unconstrained ones.

The equations of motion adopted for all our simulated systems will be all invariant under a time reversal mapping: $\mathbf{i}S'\mathbf{i}S'\Gamma = \Gamma$, where \mathbf{i} is the time reversal mapping operator. This is a key feature that our numerical framework has to exhibit. In the simulations, the equations of motion are integrated numerically using a 4th order Runge-Kutta method [104]. Lennard-Jones reduced units [85] will be used throughout this thesis.

2.2 Couette Flow

The first system selected to study the occurrence of temporal asymmetry in reversible deterministic systems was a system undergoing Couette flow [101]. This was selected primarily because it has been well characterized in the past.

This choice requires a modification of the periodic boundary conditions [105]. Our sample still evolves as if it were surrounded by periodic images of itself; however, each cell is shifted in the direction of the flow every time step by a quantity that is proportional to its coordinate perpendicular to the direction of the flow (Figure 2-2).

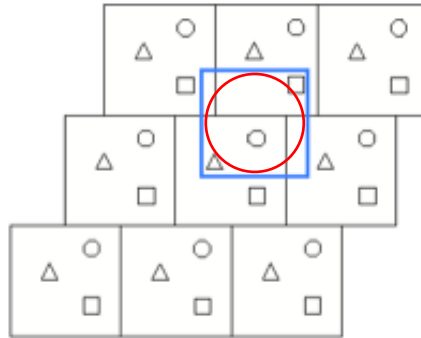


Figure 2-2 Representation of shearing periodic boundaries and minimum image convention.

The equations of motion that drive the trajectories of the particles are the SLLOD equations [106,107]:

$$\begin{aligned}\dot{\mathbf{q}}_i &= \frac{\mathbf{p}_i}{m_i} + \mathbf{i}\gamma q_{yi} \\ \dot{\mathbf{p}}_i &= \mathbf{F}_i - \mathbf{i}\gamma p_{yi}\end{aligned}\tag{2.2.1}$$

where \mathbf{q}_i are the laboratory coordinates of the particles; \mathbf{p}_i the peculiar momenta; \mathbf{F}_i

the internal forces (the forces that particle i suffers due to the interaction with the other particles that form the liquid); γ is the strain rate, which is applied in the y direction only.

The peculiar momentum can be written as:

$$\frac{\mathbf{p}_i}{m_i} = \dot{\mathbf{q}}_i - \mathbf{i} \gamma q_{yi} \quad (2.2.2)$$

from which it is easy to see that $\frac{\mathbf{p}_i}{m_i}$ is the velocity of the particle without the

streaming velocity of the layer of fluid in which its motion is embedded.

From the equations of motion, it is easy to see that:

$$m_i \ddot{\mathbf{q}}_i = \mathbf{F}_i + \gamma \delta(t) p_{yi} \mathbf{i} \quad (2.2.3)$$

where $\delta(t)$ is the Dirac delta function, which is zero if $t \neq 0$. These are clearly just Newtonian, with an added force at $t=0$.

The work done by the imposed strain, in an adiabatic condition such as the one described up to now, would cause a dissipation in the liquid that can be expressed as follows:

$$\dot{H}_0^{ad} = \frac{d}{dt} \left(\sum_i \frac{1}{2} \mathbf{p}_i \cdot \mathbf{p}_i / m_i + \Phi_i \right) = \left(\sum_i \dot{\mathbf{p}}_i \cdot \mathbf{p}_i / m_i - \mathbf{F}_i \cdot \dot{\mathbf{q}}_i \right) \quad (2.2.4)$$

where Φ_i is the i particle potential energy.

Introducing the SLLOD expressions for velocities and momenta, it is possible to express the dissipation in the following form:

$$\dot{H}_0^{ad} = - \sum_i \gamma \left(p_{xi} p_{yi} / m_i + F_{xi} q_{yi} \right) \quad (2.2.5)$$

We note that $\left(p_{xi} p_{yi} / m_i + F_{xi} q_{yi} \right) / V$, where V is the volume of the unit cell, is the

expression for the shear stress P_{xy} . Thus the SLLOD equations of motion generate a flow with the shear stress P_{xy} being the dissipative flux. As discussed in section 2.1, the Gaussian Isokinetic Thermostat serves the purpose of dissipating this heat allowing the system to reach a steady state. The SLLOD equations of motions are modified by the introduction of a (thermostatting) damping term $\varsigma \mathbf{p}_i$ in the following way:

$$\begin{aligned}\dot{\mathbf{q}}_i &= \frac{\mathbf{p}_i}{m_i} + \mathbf{i} \gamma q_{yi} \\ \dot{\mathbf{p}}_i &= \mathbf{F}_i - \mathbf{i} \gamma p_{yi} - \varsigma \mathbf{p}_i \\ \varsigma &= \frac{\sum_i (\mathbf{F}_i \cdot \mathbf{p}_i - \gamma p_{xi} p_{yi}) / m_i}{\sum_i (\mathbf{p}_i \cdot \mathbf{p}_i) / m_i}\end{aligned}\tag{2.2.6}$$

The SLLOD equations of motion with thermostat are time reversal invariant under the Kawasaki mapping $\mathbf{i}^{\mathcal{K}}$ [101], which inverts the sign of the component of the molecular momenta in the direction of the applied velocity profile and the sign of the perpendicular laboratory coordinate,

$$\mathbf{i}^{\mathcal{K}}(x_i, y_i, p_{xi}, p_{yi}) = (x_i, -y_i, -p_{xi}, p_{yi})\tag{2.2.7}$$

2.3 Colour Diffusion

The second system investigated is the model of colour diffusion. The system was selected to ensure that the effects of the non-autonomous periodic boundary conditions used in Couette flow did not influence the results. It also is more similar to the systems studied numerically by Gamba and Rondoni on their work on temporal

asymmetry [81].

The system's dynamics are driven by the *colour Hamiltonian* [99].

$$H = H_0 - \sum_{i=1}^N c_i q_{xi} F_C \quad (2.3.1)$$

where H_0 is the unperturbed Hamiltonian. The c_i are called colour charges. The property is named colour instead of charge to stress that H_0 is independent of the colour charges c_i . At equilibrium the dynamics are not effected by the colour charges of the particles. Also, colour charged particles do not interact due to their charge (unlike normal charged particles) but interact only with the external colour field

We select an equal number of positive and negative colour charges.

Given a system of N particles:

$$c_i = (-1)^i \quad (2.3.2)$$

with $i = 1, 2, \dots, N$.

The equations of motion defined by the colour Hamiltonian that drive the trajectories of the particles equations are:

$$\dot{\mathbf{q}}_i = \dot{\mathbf{p}}_i / m_i \quad (2.3.3)$$

$$\dot{\mathbf{p}}_i = \mathbf{F}_i + c_i F_C \mathbf{i} \quad (2.3.4)$$

and the adiabatic time derivative of the internal energy is:

$$\dot{H}_0^{ad} = F_C \sum_i c_i \dot{q}_{xi} \quad (2.3.5)$$

For simplicity, in the following we assume $m_i = m$, for all i .

Since $\dot{H}_0^{ad} = -JV F_C$, the dissipative flux can be identified as:

$$J = -\frac{1}{V} \sum_i c_i \dot{q}_{xi} \quad (2.3.6)$$

where V is the volume.

We define the colour current as:

$$J_x = \frac{1}{N} \sum_i c_i \dot{q}_{xi} \quad (2.3.7)$$

and note that the dissipative flux and the colour current are related by the following equation:

$$J = -\frac{N}{V} J_x \quad (2.3.8)$$

Unlike the case of shear flow, the momentum \mathbf{p}_i includes a streaming component. A realistic thermostating technique would ensure that this was subtracted.

Unfortunately the streaming velocity is not known *a priori*, so it must be approximated by the instantaneous value. The approximate peculiar momenta (the momenta without the streaming contribution due to the colour current of particles of the same colour) have the following expression:

$$\mathbf{p}_i^{Pecul} = \mathbf{p}_i - mc_i J_x \mathbf{i} = \mathbf{p}_i + mc_i J \frac{V}{N} \mathbf{i} \quad (2.3.9)$$

In order to obtain a steady state we constrain the kinetic temperature, defined as

$$\frac{(dN - (d+1))}{2} k_B T = \frac{1}{2} \sum_{i=1}^N \frac{\mathbf{p}_i^{Pecul} \cdot \mathbf{p}_i^{Pecul}}{m} \quad (2.3.10)$$

The colour equations of motions are modified by the introduction of a damping term $\zeta \mathbf{p}_i$ in the following way:

$$\dot{\mathbf{q}}_i = \frac{\mathbf{p}_i}{m} \quad (2.3.11)$$

$$\dot{\mathbf{p}}_i = \mathbf{F}_i + c_i F_C \mathbf{i} - \zeta \left(\mathbf{p}_i - c_i m J_x \mathbf{i} \right) \quad (2.3.12)$$

$$\zeta = \frac{\sum \mathbf{F}_i \cdot (\mathbf{p}_i - m c_i J_x \mathbf{i})}{\sum \mathbf{p}_i \cdot (\mathbf{p}_i - m c_i J_x \mathbf{i})} \quad (2.3.13)$$

However, for our theoretical analysis of Chapter 5, it is more convenient to constrain

$$\frac{1}{2} \sum_{i=1}^N \frac{\mathbf{p}_i \cdot \mathbf{p}_i}{m_i} = \frac{(dN - (d+1))}{2} k_B T. \text{ This is because there is no equilibrium distribution}$$

function consistent with the equations (2.3.10)-(2.3.13) with F_C set to zero. Therefore, in the theoretical analysis of Chapter 5 we adopt the following equations:

$$\dot{\mathbf{q}}_i = \frac{\mathbf{p}_i}{m} \quad (2.3.14)$$

$$\dot{\mathbf{p}}_i = \mathbf{F}_i + c_i F_C \mathbf{i} - \zeta \mathbf{p}_i \quad (2.3.15)$$

$$\zeta = \frac{\sum \mathbf{p}_i \cdot (\mathbf{p}_i + c_i F_C \mathbf{i})}{\sum \mathbf{p}_i \cdot \mathbf{p}_i} \quad (2.3.16)$$

Again these equations of motion can be derived using Gauss' principle of least constraint.

2.4 Fluctuation Paths

In this thesis, a number of different ways of defining fluctuation paths are used.

This is because some definitions are more useful or natural for the different analyses that were undertaken. If, for a given a definition, we obtain asymmetric fluctuation paths, we will have detected temporal asymmetry in our system.

2.4.1 First Definition of Fluctuation Path

This fluctuation path defined in this section is shown schematically in Figure 2-3.

When identifying large fluctuations or large deviations from a nonequilibrium steady state value of a property, a threshold (T_{hr}) that is to be crossed needs to be selected. It gives the first quantitative element that allows the definition of a fluctuation as a measurable property. A selection of different thresholds will necessarily result in different paths being identified as the fluctuation path. If we set the threshold high enough, we focus our attention exclusively on exceptional fluctuations: setting it 2.5 standard deviations above or below the mean serves this purpose. It is in the evolution of a property while it is approaching the threshold that we will consider constructing fluctuation paths. In this first definition we consider the approach to the threshold and its departure from it, as well as the period it is above it. Therefore, the second element that needs to be set, in order to define the fluctuation, is the time of observation of the fluctuation 2τ . Within the same definition of fluctuation, different selections of the two parameters identify different fluctuation paths.

Since the fluctuations occur above and below the mean (μ), we refer to two entities. If the threshold is set above the mean value ($T_{hr} - \mu > 0$), we consider “peak fluctuation paths”; otherwise ($T_{hr} - \mu < 0$) we consider “trough fluctuation paths”. For any peak

that crosses the threshold, the peak fluctuation path is the set of values that the property of interest assumes about the midpoint between the time instant in which the property crosses the threshold as the peak is approached, and the time instant in which the property crosses the threshold after passing through the threshold again, on the other side of the peak. It will have a total period of 2τ . The set is marked in black on Figure 2-3. The trough fluctuation path is defined similarly, but with respect to the trough.

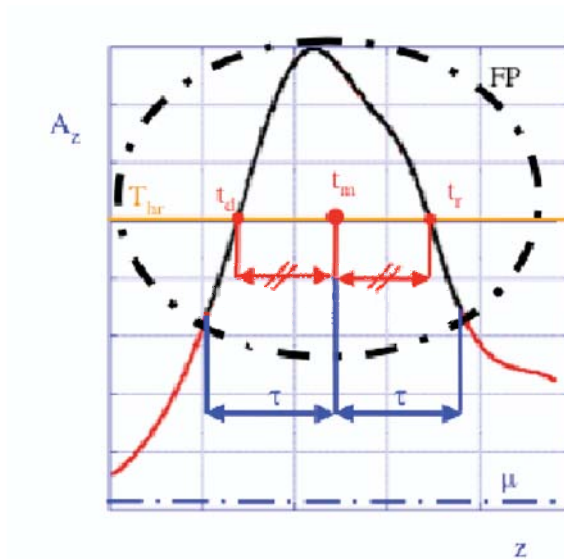


Figure 2-3 Illustration of construction of the peak fluctuation path (First Definition).

It will be useful to express this definition mathematically.

Let us call S^z the operator that defines the evolution of the system in time z from initial phase point Γ . So, given an observable $A_z = A(S^z\Gamma)$ with mean μ , we select

the time width of interest, $2\tau > 0$, and a threshold value $T_{hr} \neq \mu$. Then, for every t_d (see Figure 2-3) such that $A_{t_d} = T_{hr}$ and $(T_{hr} - \mu) \dot{A}_{t_d} > 0$, there will be a time t_r :

$$t_r = \min \left\{ z : z > t_d, A_z = T_{hr}, (T_{hr} - \mu) \dot{A}_z < 0 \right\} \quad (2.4.1)$$

and so a time t_m :

$$t_m = \frac{(t_d + t_r)}{2} \quad (2.4.2)$$

Therefore, we define the observable X_t , for $t \in [-\tau, \tau]$ as: $X_t = A_{t+t_m}$. The time-ordered set of values $\{X_t, \text{with } t \in [-\tau, 0]\}$ defines the path leading toward the peak or trough, or *deviation*. The time-ordered set of values $\{X_t, \text{with } t \in [0, \tau]\}$ defines the path leading away from the peak or trough, or *relaxation*. The combination of the two sets defines the fluctuation paths. Our attention will focus either on the conditional average over all fluctuations or the most probable fluctuation path in accordance with past studies [70,81]. The first case is computationally simpler.

To quantify the asymmetry, we define an asymmetry coefficient as follows. Given any fluctuation path of time width τ and threshold T_{hr} , we define the measure of asymmetry δ_t for $t \in [0, +\tau]$ as:

$$\delta_t = X_{-t} - X_t \quad (2.4.3)$$

and we denote the ensemble average of δ_t , $\langle \delta_t \rangle$. We note that here the ensemble is the set of fluctuation paths, and therefore this ensemble average, and others in Chapters 2-4 are over this set. The time-averaged and ensemble averaged measure of asymmetry α_t is given as:

$$\alpha_t = \left\langle \frac{1}{t} \int_0^t (X_{-z} - X_z) dz \right\rangle \quad (2.4.4)$$

In order to provide a better understanding of how asymmetry arises in the fluctuation path, α_t and $\langle \delta_t \rangle$, will be plotted for different values of $t \in [0, +\tau]$. Provided α_t or $\langle \delta_t \rangle$ are not null for every t , the fluctuation path is asymmetric.

α_t is particularly useful for the study on shear flow, as the averaging of the value of $(X_{-z} - X_z)$ minimises effects related to the periodical oscillations of the system values in the SLLOD algorithm due to the periodical sliding of the periodic images, as we will explain in the last section of Chapter 3.

2.4.2 Second Definition of Fluctuation Path

In our second approach to systematically generating fluctuation paths, we again define a threshold T_{hr} and monitor paths that go towards and away from this threshold value. The time interval 2τ over which the path is considered is a parameter that must be chosen. In contrast to the previous case, we do not include the period between t_d and t_r as part of the fluctuation path. Thus, for any peak that crosses the threshold, the peak fluctuation path is the concatenation of the set of values that the property under interest assumes just before reaching the threshold as the peak is approached, and the set of the values that the property assumes after passing through the threshold again, on the other side of the peak. These sets are marked in bold on Figure 2-4. Equal time intervals for the two sets are considered. The trough fluctuation path is defined similarly, but with respect to the trough. So given an observable $A_z = A(S^z \Gamma)$ with

mean μ , we select the time width of interest, $2\tau > 0$, and a threshold value $T_{hr} \neq \mu$.

Then, for every time t_d (see Figure 2-4) at which the value of the property reaches the threshold from the mean, such that $A_{t_d} = T_{hr}$ and $(T_{hr} - \mu) \dot{A}_{t_d} > 0$, there will be a

$t_r = \min \{z : z > t_d, A_z = T_{hr}, (T_{hr} - \mu) \dot{A}_z < 0\}$. So, we define the observable X_t , for

$t \in [-\tau, \tau]$ as: $X_t = A_{t_d+t}$, for $t \in [-\tau, 0]$ and $X_t = A_{t_r+t}$ for $t \in [0, \tau]$. The time-ordered

set of values $\{X_t, \text{with } t \in [-\tau, 0]\}$ defines the path leading toward the peak or trough

-or *deviation*-; the time-ordered set of values $\{X_t, \text{with } t \in [0, \tau]\}$ defines the path

leading away from the peak or trough -or *relaxation*-; the combination of the two sets

defines the fluctuation path. As in the previous section, our attention in the following

focuses either on the average or the most probable fluctuation path. This is what has

been considered also in past studies [81]. To quantify the asymmetry, we adopt the

same coefficient of asymmetry α_t and δ_t employed in Section 2.4.1 (see equation

(2.4.4) and (2.4.3)). Again α_t and δ_t will be plotted for $t \in [0, \tau]$.

2.4.3 Third Definition of Fluctuation Path

This definition of fluctuation path has been selected as it is amenable to representation as a cross correlation function, as discussed in Chapter 5. It is also, perhaps, the most natural way of classifying peaks or troughs. Following is its mathematical expression, accompanied by a graphical representation.

In our construction of the fluctuation path, we again define a threshold T_{hr} (in the example of the figure set equal to $2.5\sigma + \mu$) and a time interval τ , as shown in Figure

2-5. We consider the stationary points (maxima and minima) that exceed in absolute value the selected threshold T_{hr} . The time step at every such stationary point is referred to as t_{STAT} and we consider the ordered values that the property assumes for the time interval τ before t_{STAT} and for the time interval τ after t_{STAT} (refer to Figure 2-5).

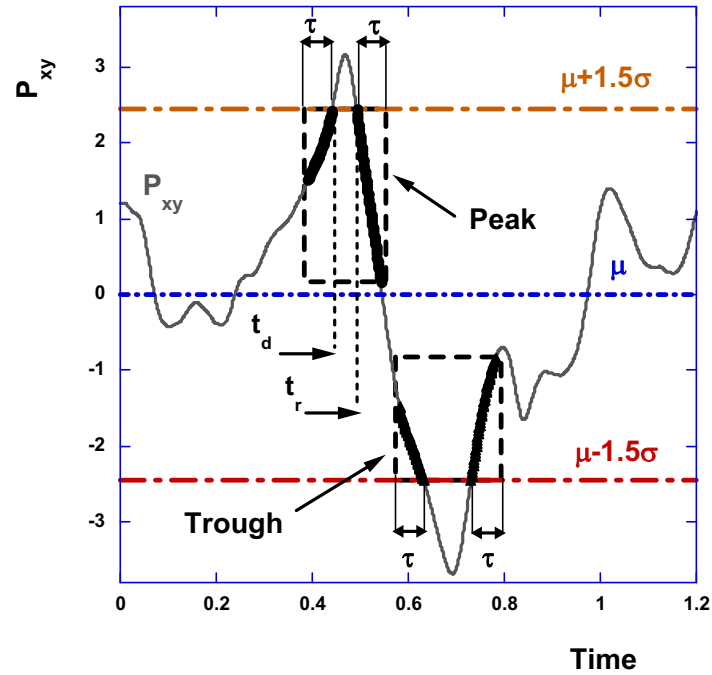


Figure 2-4 Illustration of construction of the peak and trough fluctuation paths (second definition).

For every t_{STAT} , the fluctuation path is the set of absolute values that the property under interest assumes in the 2τ interval about the stationary point (refer to Figure 2-6). More precisely, we define fluctuation path as the ordered array of absolute values that the property assumes in the interval $[t_{STAT} - \tau, t_{STAT} + \tau]$.

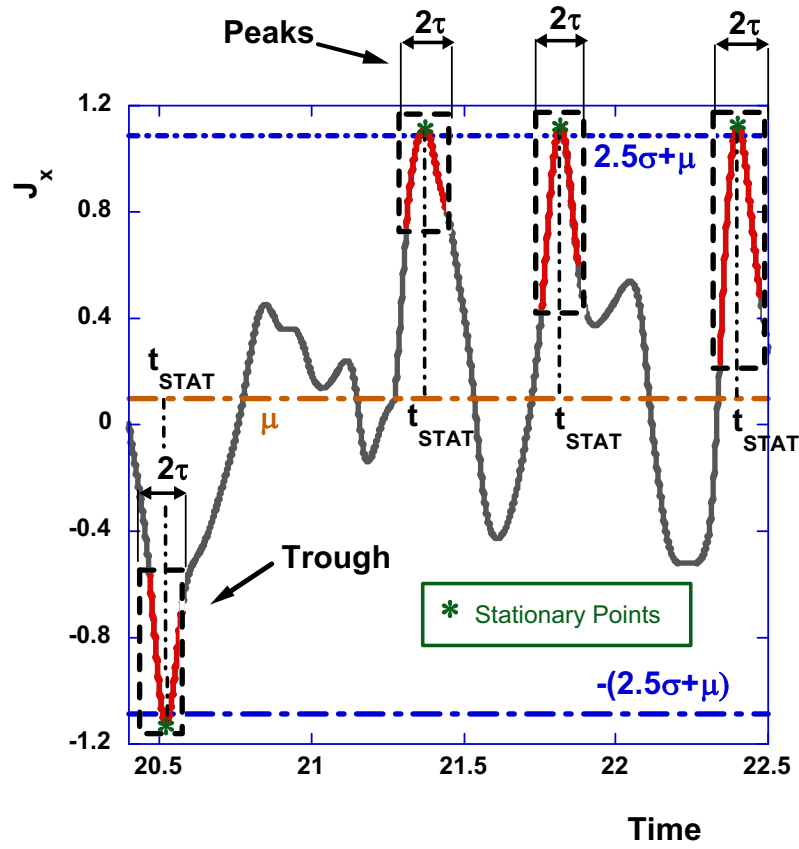


Figure 2-5 Illustration of construction of the peak and trough fluctuation paths (third definition).

As a result, given an observable $X_t = X(S^t \Gamma)$ with mean μ , we select the time width of interest, $\tau > 0$, and a positive threshold value $T_{hr} \neq \mu$. Then, for every t_{STAT} such that

$|X(t_{STAT})| > T_{hr}$ and $\dot{X}(t_{STAT}) = 0$, we define the observable Y_t , for $t \in [-\tau, +\tau]$ as:

$$Y_t = |X(t_{STAT} + t)| \text{ for } t \in [-\tau, +\tau].$$

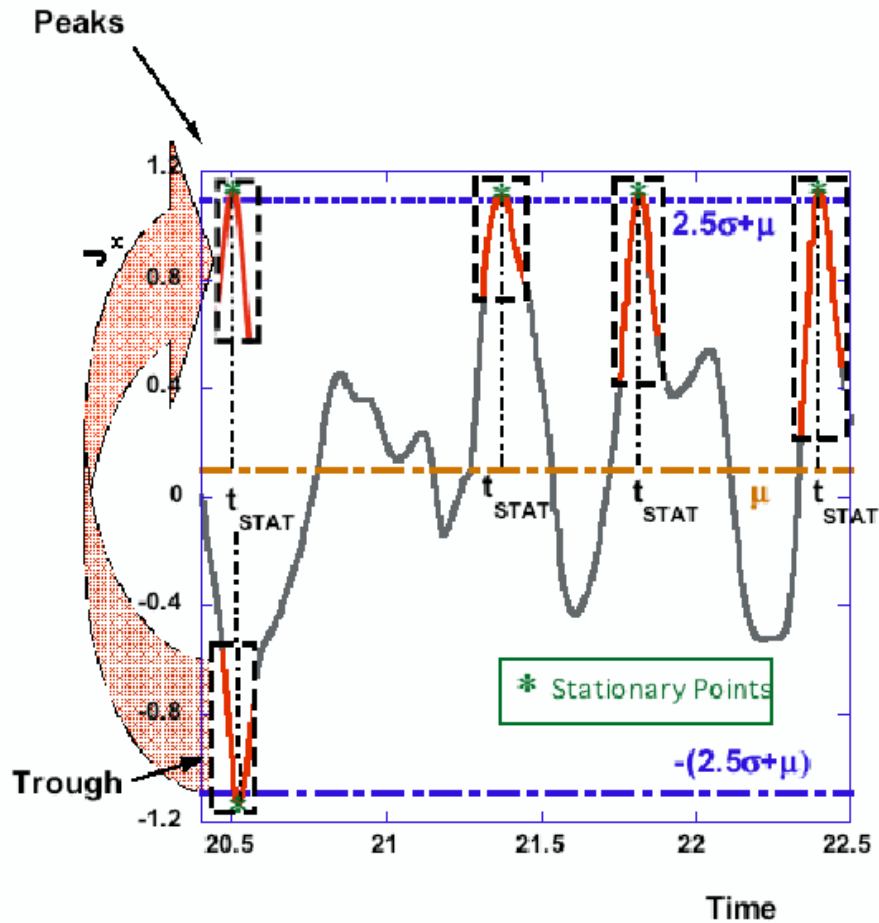


Figure 2-6 Construction of the fluctuation paths: troughs are converted to peaks.

The time-ordered set of values $\{Y_t, \text{ with } t \in [-\tau, 0]\}$ defines the path leading toward stationary point or the deviation. The time-ordered set of values $\{Y_t, \text{ with } t \in [0, \tau]\}$ defines the path leading away from the stationary point or the relaxation. The combination of the two sets defines the fluctuation paths. Our attention in the following focuses on the average fluctuation path.

Furthermore, for every t_{STAT} such that $|X_{t_{STAT}}| \geq T_{hr}$, $\dot{X}_{t_{STAT}} = 0$ and $\ddot{X}_{t_{STAT}} < 0$, we define

the observable $X_t^P = X(t_{STAT} + t)$ as “Peak”; while if $\ddot{X}_{t_{STAT}} > 0$ we define

$X_t^T = X(t_{STAT} + t)$ as “Trough”.

If the maximum of the peak ($X_{t_{STAT}}$) is over the threshold, we define it as over threshold peak; if it is smaller than minus the threshold, we define it as under threshold peak. In the same way, if the minimum of the trough ($X_{t_{STAT}}$) is under minus the threshold, we define it as under threshold trough; if it is over the threshold, define it as over threshold trough (refer to Figure 2-7).

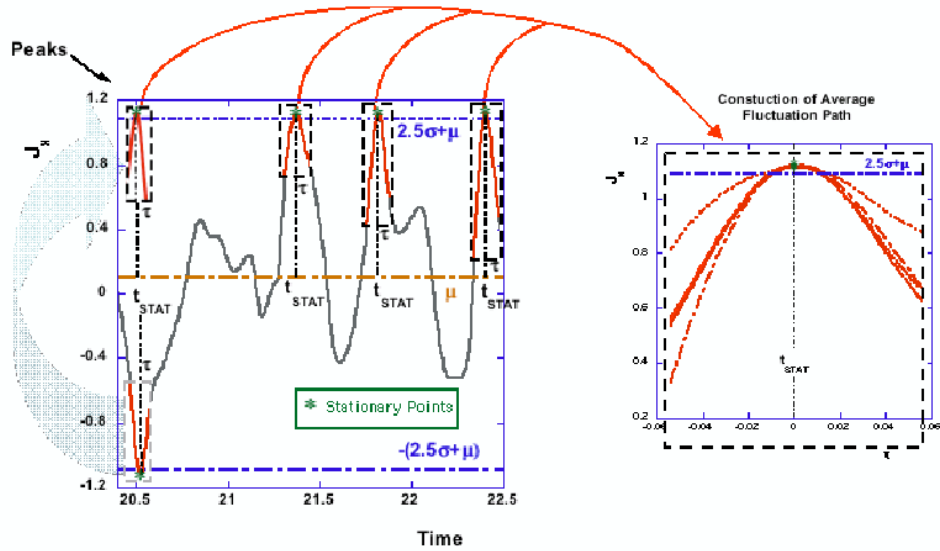


Figure 2-7 Construction of the ensemble average fluctuation paths, averaging the fluctuation path centered in t_{STAT} .

To quantify the asymmetry, we adopt δ_t of Section 2.4.1 (see equation (2.4.3)). As

for the previous definitions of fluctuation paths, $\langle \delta_t \rangle$ will be plotted for $t \in [0, \tau]$.

As our aim is the detection and study of temporal asymmetry, the previous are only three possible definitions of fluctuation paths. Each one of them has been adopted in different situations.

The first definition of fluctuation path has the appealing feature of not bounding any specific geometric feature in any specific point, as the subsequently adopted definitions do, yet it is computationally more cumbersome to obtain, due to the higher allocation of memory necessary not to discard any wide fluctuation. This was adopted only in the preliminary runs

The second definition of fluctuation path is computationally less demanding than the first one, yet both definitions are problematic to express in a mathematical formula that will allow us to prove asymmetry in fluctuation paths in a simple and effective way *via* transient time correlation function.

The third definition is instead amenable to representation as a cross correlation function and it is the most natural way of classifying peaks or troughs.

Again we note that, having chosen a definition, the detection of asymmetric fluctuation paths would constitute evidence of temporal asymmetry in our system.

2.5 Average and most probable paths

Any single fluctuation path of a finite system will naturally present asymmetry, even at equilibrium. In order to consider this, we need some way of examining an ensemble of fluctuation paths. In our simulations we consider the mean and the most likely fluctuation path. The most probable fluctuation paths are constructed by collecting the

property values on rectangular grids, with cells of width equal to the time step (in the direction of time). The height (in the direction of the observable) varied for every property and field, and was guided by computational time and memory allocation availability. We adopted the finest binning resolution possible on the available computational resources –aiming for a smooth enough histogram. Homogeneity in the binning resolution was obtained in the simulations that adopted the second definition of fluctuation path, which is less demanding in terms of memory allocation.

Evaluating the average is computationally more simple than evaluating the most probable one, and the computation of the latter has not always been possible. We note, however, that the most probable and the average fluctuation paths will coincide in the large N limit, when there is only one characteristic fluctuation path.

Chapter Three: INITIAL NUMERICAL EXPERIMENTS: SHEAR FLOW

In this chapter we monitor temporal asymmetries of fluctuation paths in a nonequilibrium microscopic shearing system using nonequilibrium molecular dynamics simulations described in Section 2.2.

3.1 Selection of parameters for simulation study

Two-dimensional molecular dynamics simulations have been carried on a primitive cell containing 8 particles with reduced (number) density equal to 0.8, kinetic temperature fixed at 1, and time step of 10^{-3} . The choice of such a small number of particles was made in order to be able to observe a considerable number of fluctuations. In the linear regime fluxes are coupled to their conjugate forces by linear transport relations. Numerical experiments are needed to determine the shear rates γ for which the system can be considered to be in the linear regime, as this varies for each combination of density, temperature and number of particles. We wish to explore fluctuation paths in the linear and nonlinear regime, where we expect a different behaviour. In order to do so, simulations with different imposed strain rates have been run. The average values of shear stress P_{xy} , the flux conjugated to the strain rate (γ), have then been plotted with respect to γ in Figure 3-1.

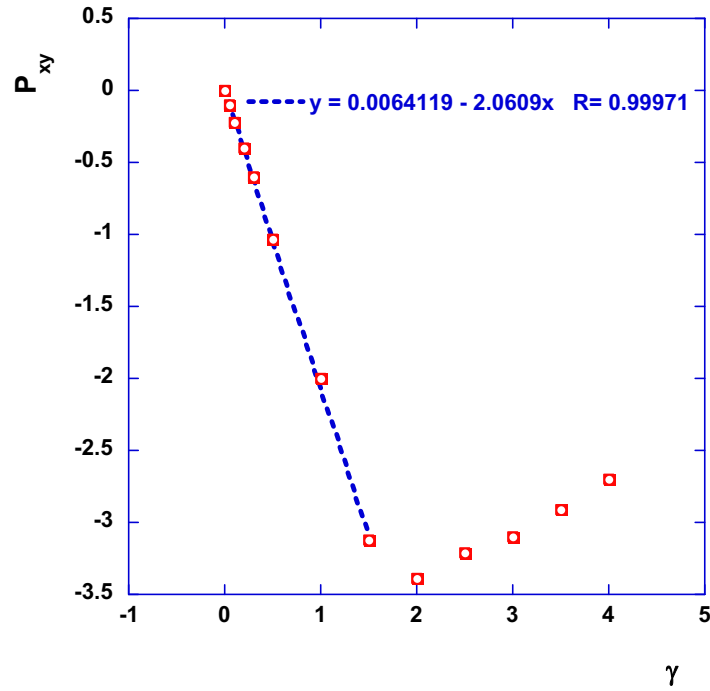


Figure 3-1 Average values of shear stress vs strain rate. The values of P_{xy} are obtained from simulations of at least 100 time units

The test run simulations showed that the domain with $\gamma \geq 2$ can confidently be considered to be out of the linear regime. Our data shows that a satisfactory linear approximation does not extend above values of the shear flow $\gamma \approx 1.5$. So we selected shear flow $\gamma = 0.05, 0.1, 0.2, 0.3, 0.5, 1, 1.5$ for the linear regime, and $\gamma = 2, 3, 4$ out of the linear regime. We note that at high strain rates, non-physical behaviour is observed in this model, due to the formation of a “string phase” produced by the thermostatting mechanism [108]. However in this work we are not concerned about this problem because our main aim is to describe the temporal behaviour of the fluctuation path of a generic reversible dynamical system and not to realistically model a physical system. Most importantly, equilibrium simulations ($\gamma = 0$) have been performed, in order to check the suitability of our experimental

framework to the task of detecting temporal asymmetry. This is predicted by equilibrium statistical mechanics for deterministic systems. It is also consistent with the nonequilibrium theories for fluctuations in stochastic models [50,51,55-58,69]. If our system exhibited asymmetric fluctuations at equilibrium, it could not be regarded as “physical” with respect to our property of interest or the numerical error must be too large and it could not be considered as suitable for the purposes of the project.

For these experiments, we chose a number of phase variables that fluctuated and were odd or even, such as shear stress, pressure, potential energy and total energy.

Shear stress P_{xy} , which is the flux coupled to the force that drives the system out of equilibrium in this system, was considered in most detail.

The project studies the fluctuations of the instantaneous values of thermodynamic properties around the steady state. We are interested in looking at the shapes of the peaks in the fluctuations - and in particular in the shapes of fluctuations that represent large deviations from the mean. In order to do this and following the work of Gamba and Rondoni [81], we examine the fluctuations that pass through a 'threshold' value of the property. To ensure that we are examining fluctuations with large deviations from the mean, we select the threshold value to be several standard deviations from the mean, consistent with earlier studies [50,51,69,83].

In order to identify fluctuation paths, the first step consisted of obtaining a rough estimate of means and standard deviations of the values of shear stress, pressure, potential energy and total energy for the selected values of shear flow

($\gamma = 0, 0.05, 0.1, 0.2, 0.3, 0.5, 1, 2, 2.5, 3, 3.5, 4$). These

approximate results have been obtained from simulations of 10^5 time steps runs. The

accuracy of means and standard deviations is not crucial; all we needed was to set the thresholds “far” from the mean, so that our analysis could focus on exceptional fluctuations. This corresponds to setting the threshold roughly several standard deviations from the mean. They are therefore presented in Table 3-1.

Table 3-1 Means (μ) and standard deviations (σ) of shear stress (P_{xy}), pressure (P), Internal Energy (E) and potential energy (U) as a function of the shear stress (γ) from 10^5 time steps runs. Errors are given when available.

γ	$\mu(P_{xy})$	$\sigma(P_{xy})$	$\mu(E)$	$\sigma(E)$	$\mu(U)$	$\sigma(U)$	$\mu(P)$	$\sigma(P)$
0	0 ± 0.012	1.63 ± 0.003	1.25	0.228	3.57	1.908	5.4 ± 0.074	1.8 ± 0.095
0.05	-0.1 ± 0.204	1.5 ± 0.157					5.73 ± 0.011	1.93 ± 0.015
0.1	-0.22 ± 0.066	1.54 ± 0.049					5.75 ± 0.013	1.93 ± 0.018
0.2	-0.4 ± 0.168	1.59 ± 0.086					5.81 ± 0.026	1.93 ± 0.034
0.3	-0.6 ± 0.136	1.6 ± 0.121					5.88 ± 0.02	1.9 ± 0.106
0.5	-1.03 ± 0.012	1.781 ± 0.003					6.064 ± 0.008	1.992 ± 0.003
1	-2.0 ± 0.204	2.3 ± 0.157	1.39	0.32	4.65	2.56	6.7 ± 0.176	2.5 ± 0.108
1.5	-3.1209							
2	-3.39 ± 0.066	3.49 ± 0.049	1.64	0.628	6.64	5.068	8.55 ± 0.078	4.31 ± 0.077
2.5	-3.2074							
3	-3.1 ± 0.168	3.35 ± 0.086	1.64	0.628	6.64	5.068	8.96 ± 0.093	4.43 ± 0.077
3.5	-2.9138							
4	-2.7 ± 0.136	3.1 ± 0.121	1.73	0.628	7.4	5.108	9.053 ± 0.093	4.35 ± 0.091

In order for us to determine on which side of the mean the threshold needs to be set so that it may be possible to observe exceptional fluctuations, more considerations are required. Figure 3-2 shows plots of samples of the properties under consideration obtained from a steady state simulation run with strain rate $\gamma=1$; the lines in red represent thresholds set 2.5 times above and below the mean of each property. Large fluctuations (several standard deviations from the mean) are only observed on one side of the mean for all these nonequilibrium simulations. The bias in the mean and deviations from the mean can be understood in all cases by considering the microscopic expressions for the properties considered; in addition the bias in the mean of properties that are odd under time reversal is predicted by the fluctuation theorems which also gives some quantitative information on the distribution [6]. Such bias in the deviation suggests we set the threshold below the mean for shear stress and above for all the other properties.

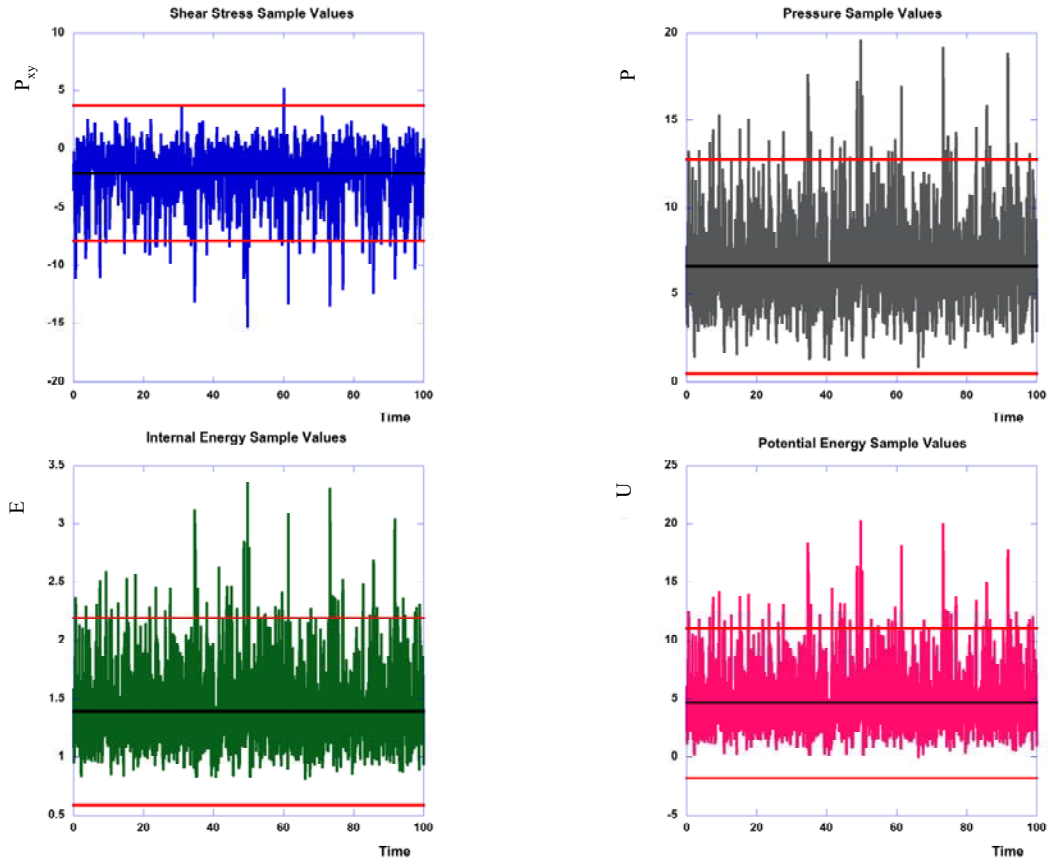


Figure 3-2 Sample values of shear stress (P_{xy}), pressure (P), Internal Energy (E) and potential energy (U) with shear stress γ equal to 1 (in the linear regime).

As the field increases, as we can see in Figure 3-3 for $\gamma=3$, the bias is even more evident and the need to follow the above method for the selection of the thresholds becomes ever more relevant, if we want to be able to observe any fluctuations at all. Of course the bias becomes less as the field is reduced through the linear regime and at equilibrium there is no bias in the mean or in deviations.

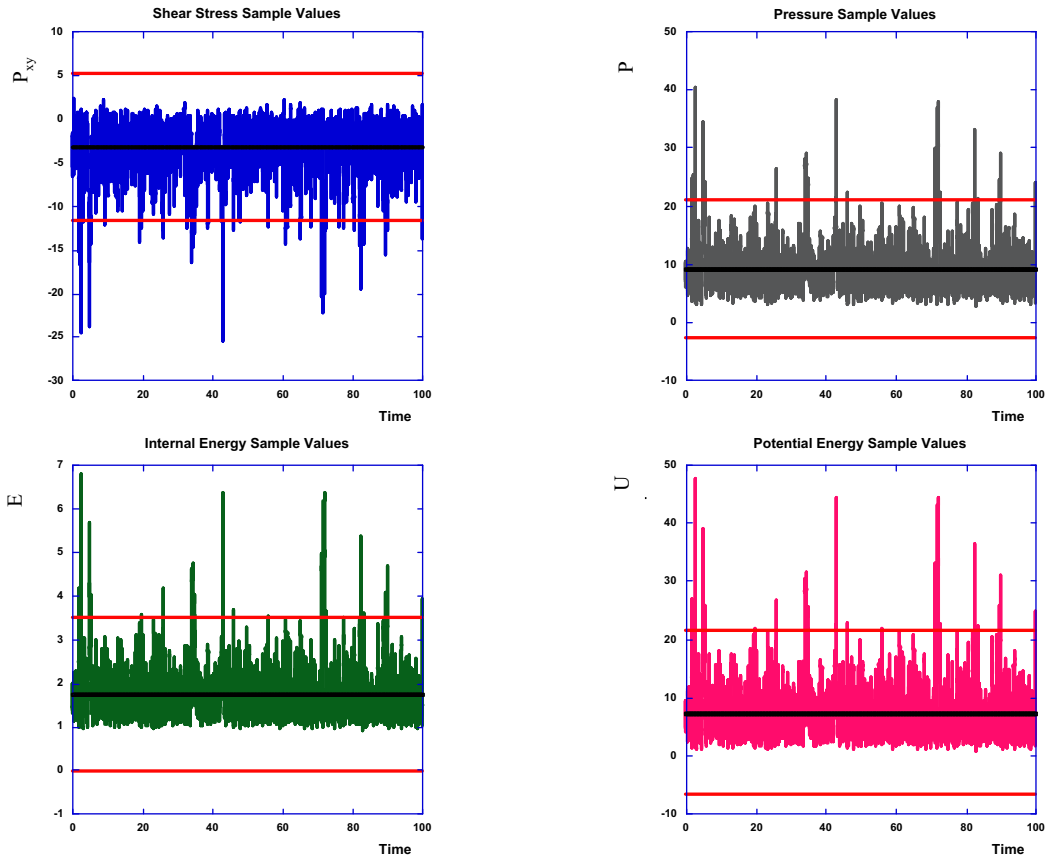


Figure 3-3 Sample values of shear stress (P_{xy}), pressure (P), Internal Energy (E) and potential energy (U) with shear stress γ equal to 3 (beyond the linear regime).

Once the appropriate threshold for the observation of exceptional fluctuations for each property has been set, it is necessary to select which scheme we will use to select fluctuations that will be collated to form “typical” fluctuation paths.

3.1.1 Qualitative observation of asymmetry.

On the basis of the data presented in Table 3-1, simulations of 3×10^8 time steps have been carried out for each strain rate $\gamma = 0, 1, 2, 3, 4$, to qualitatively monitor the fluctuation path of shear stress (P_{xy}), pressure (P), internal energy (E) and potential energy (U).

As previously stated, out of equilibrium, the distributions are biased to one side of the mean: above it for pressure, internal energy and potential energy, and below it for shear stress; this led us to focus our attention on peak fluctuation paths for pressure, internal energy and potential energy, and on trough fluctuation paths for shear stress P_{xy} . If at equilibrium our model exhibited temporally asymmetric fluctuations (larger than expected error bars), it must be an erroneous conclusion (due for example to the effect of numerical errors) and therefore it would not constitute an experimental environment that is suited to our task.

Furthermore at equilibrium we consider both peak and trough fluctuations of P_{xy} with thresholds set to $\mu + 2.5\sigma$ and $\mu - 2.5\sigma$ respectively. As P_{xy} is an odd property with respect to time reversal mapping $\mathbf{i}^{\mathcal{K}}$ (such that $\mathbf{i}^{\mathcal{K}}(x_i, y_i, p_{xi}, p_{yi}) = (x_i, -y_i, -p_{xi}, p_{yi})$) the peaks and troughs should be the mirror images of one another, if we want to claim physical behavior for our numerical experimental framework. By odd with respect to time reversal mapping $\mathbf{i}^{\mathcal{K}}$, we mean that P_{xy} behaves such that $P_{xy}(\Gamma) = -P_{xy}(\mathbf{i}^{\mathcal{K}}\Gamma)$, where Γ is a point in phase space.

Out of equilibrium ($\gamma \neq 0$) instead, the trough fluctuation paths corresponding to thresholds set to $\mu - 2.5\sigma$ are collected for shear stress; while the peak fluctuation paths corresponding to thresholds set to $\mu + 2.5\sigma$ are collected for the other quantities under observation. The fluctuation paths are collected for a time interval τ of duration 0.5 or 0.6 in Lennard-Jones units.

We will present and compare results obtained adopting the first and the second definition of fluctuation path (refer to Section 2.4.1 and Section 2.4.2) for shear stress (P_{xy}) and pressure (P). Once shown that shear stress (P_{xy}) and pressure (P) are temporally asymmetric irrespective of the choice of the definition of fluctuation path, we will then also present some samples of the results obtained for internal energy (E) and potential energy (U) adopting only the first definition of fluctuation, in order to show that temporal asymmetry is a general feature for nonequilibrium system properties.

We will display two-dimensional histograms of (first or second definition) fluctuation paths of P_{xy} , pressure P , internal energy E and potential energy U . The most probable fluctuation path (refer to Section 2.5) will be highlighted in gold.

These runs were “pilot studies”, constituting a preliminary test of adequacy of our numerical experimental model and a first detection of temporal asymmetry using a graphical basis: on account of such results it was possible to make the decision to proceed in further and more detailed analysis of the phenomenon.

As previously discussed, the first step was to test the adequacy of our numerical experimental framework at equilibrium ($\gamma = 0$). Figure 3-4 displays the peak and trough fluctuation path histograms for shear stress (P_{xy}) at equilibrium ($\gamma = 0$) obtained adopting the first definition of fluctuation path; φ is the relative probability (number of occurrences over most frequent occurrences), calculated dividing the height of the histogram by the maximum height. Peak and trough fluctuation paths (thresholds T_{hr} set 2.5 times the standard deviation above and below the average) are plotted synoptically. As to be expected, for a property at equilibrium, they are symmetric about the plane $P_{xy} = \mu(P_{xy}) = 0$. In addition, the fluctuation paths appear temporally symmetric. This confirms qualitatively that the model exhibits symmetric values of peak and trough fluctuation paths at equilibrium, as required. The same considerations can be made for the equilibrium peak and trough fluctuation path obtained from the second definition, as it can be see from Figure 3-5.

Figure 3-6 shows the histograms of the first definition trough fluctuation path of P_{xy} for $\gamma = 0, 1, 2, 3$. We can see how, starting from a temporally symmetric fluctuation at equilibrium $\gamma = 0$, the profiles appear to become asymmetric with γ turned on.

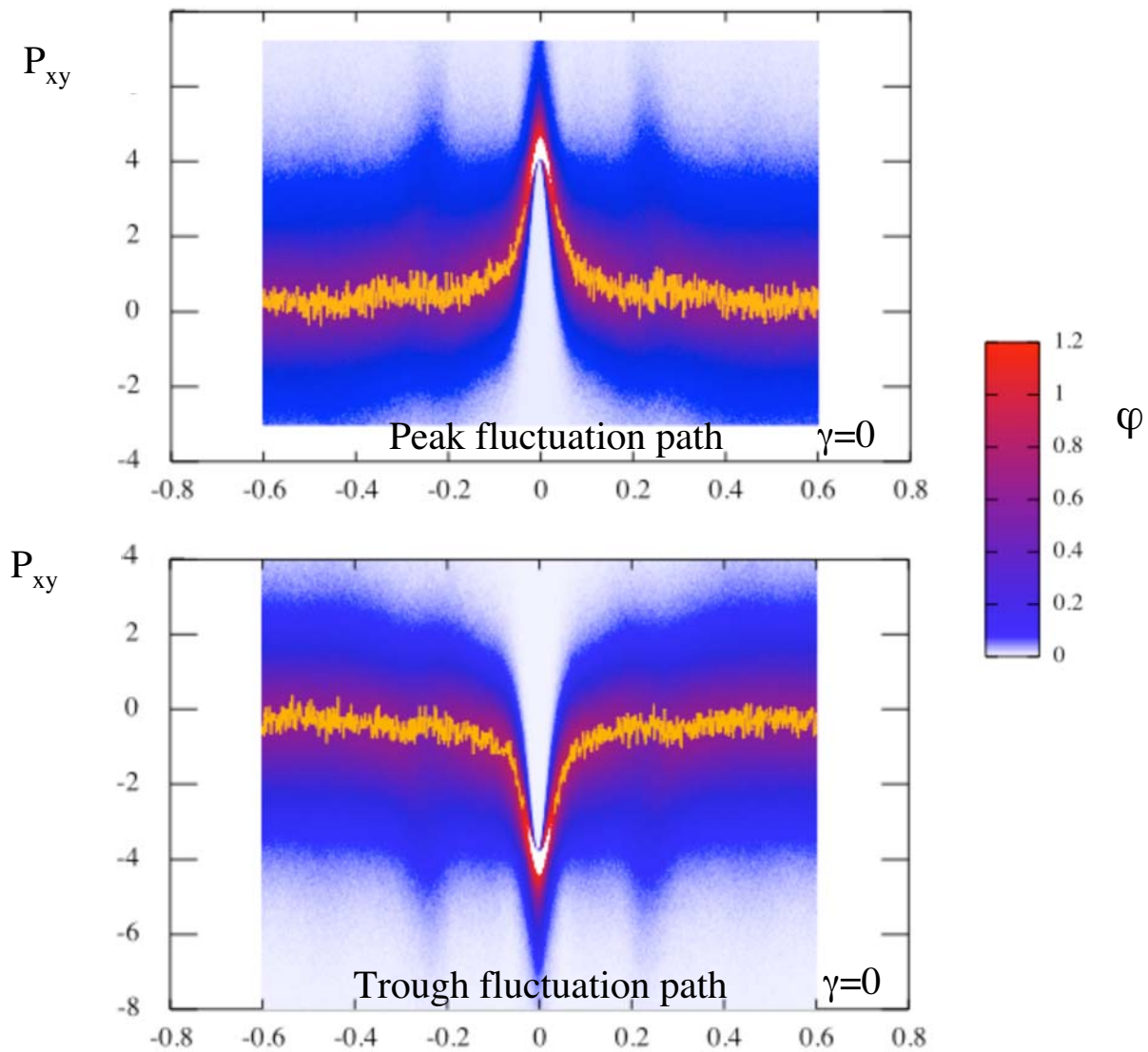


Figure 3-4 Histograms of shear stress (P_{xy}) peak and trough fluctuation paths at equilibrium ($\gamma = 0$) with a “bird’s eye” view parallel to the frequency axis, using the first definition of fluctuation path. The colours in the legend refer to the values of φ . The gold line is a line through the ridge of the histograms.

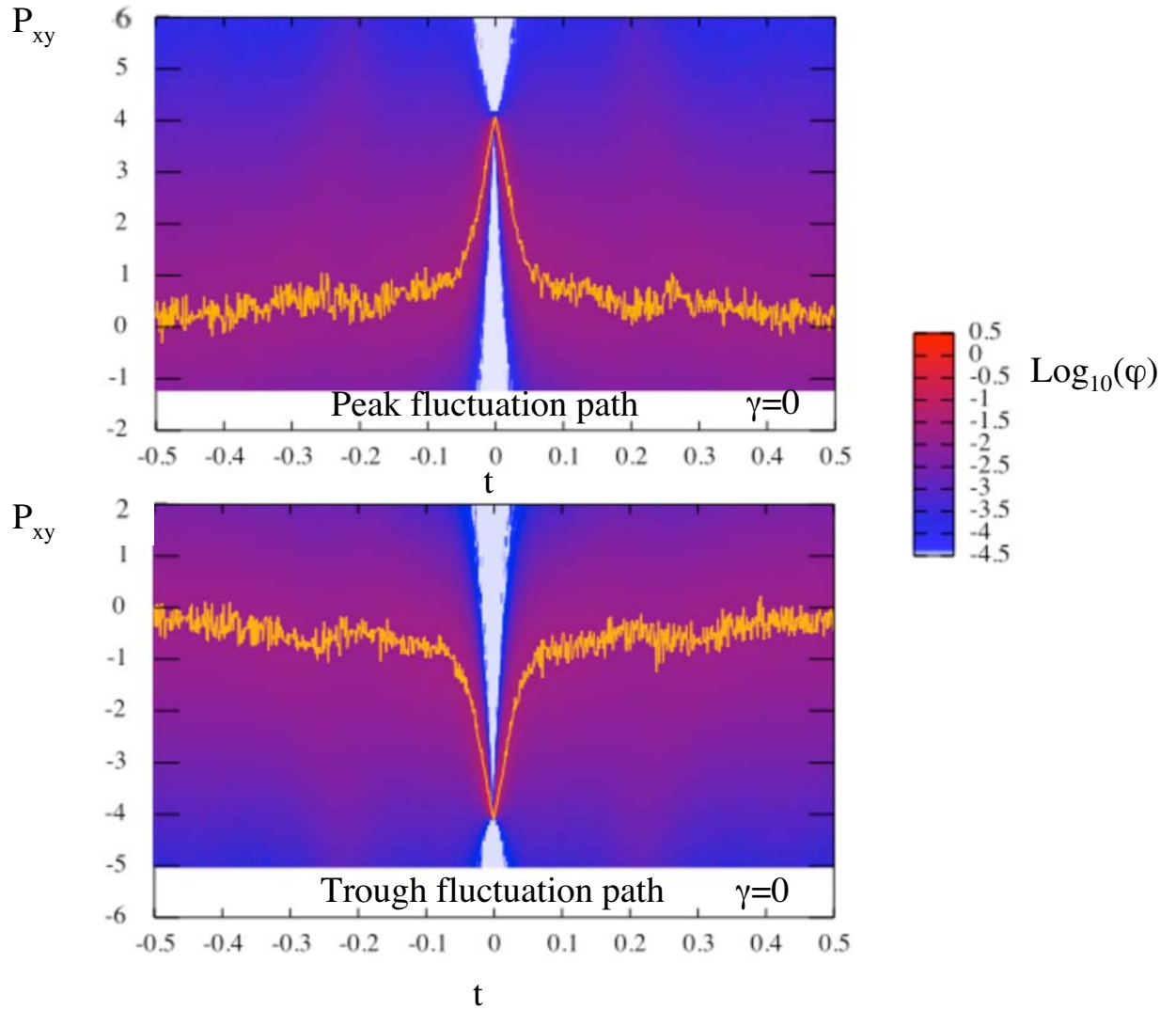


Figure 3-5 Histograms of shear stress (P_{xy}) peak and trough fluctuation paths at equilibrium ($\gamma = 0$) with a “bird’s eye” view parallel to the frequency axis, using the second definition of fluctuation path. The colours in the legend refer to the values of $\log_{10}(\varphi)$. The gold line is a line through the ridge of the histograms.

We can see this better in Figure 3-7, which shows the trough fluctuation paths of shear stress for $T_{hr} = \mu - 2.5\sigma$, with “bird’s eye” view (parallel to the frequency axis) of the frequency histogram for various γ ($\gamma=0, 1, 2, 3, 4$).

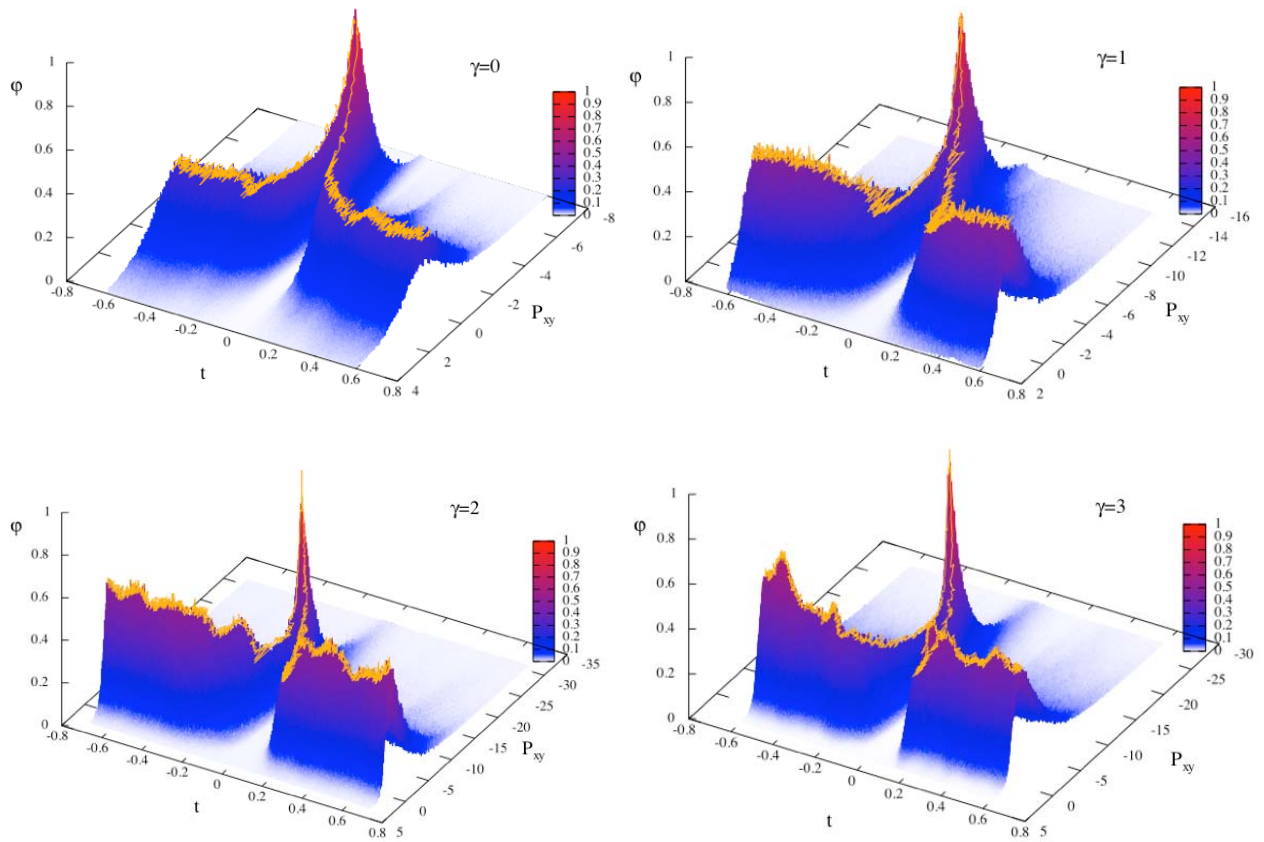


Figure 3-6 Histogram of shear stress (P_{xy}) trough fluctuation paths for various strain rates ($\gamma=0, 1, 2, 3$) using the first definition of fluctuation path. The colours in the legend refer to the values of ϕ . The gold line is a line through the ridge of the histograms.

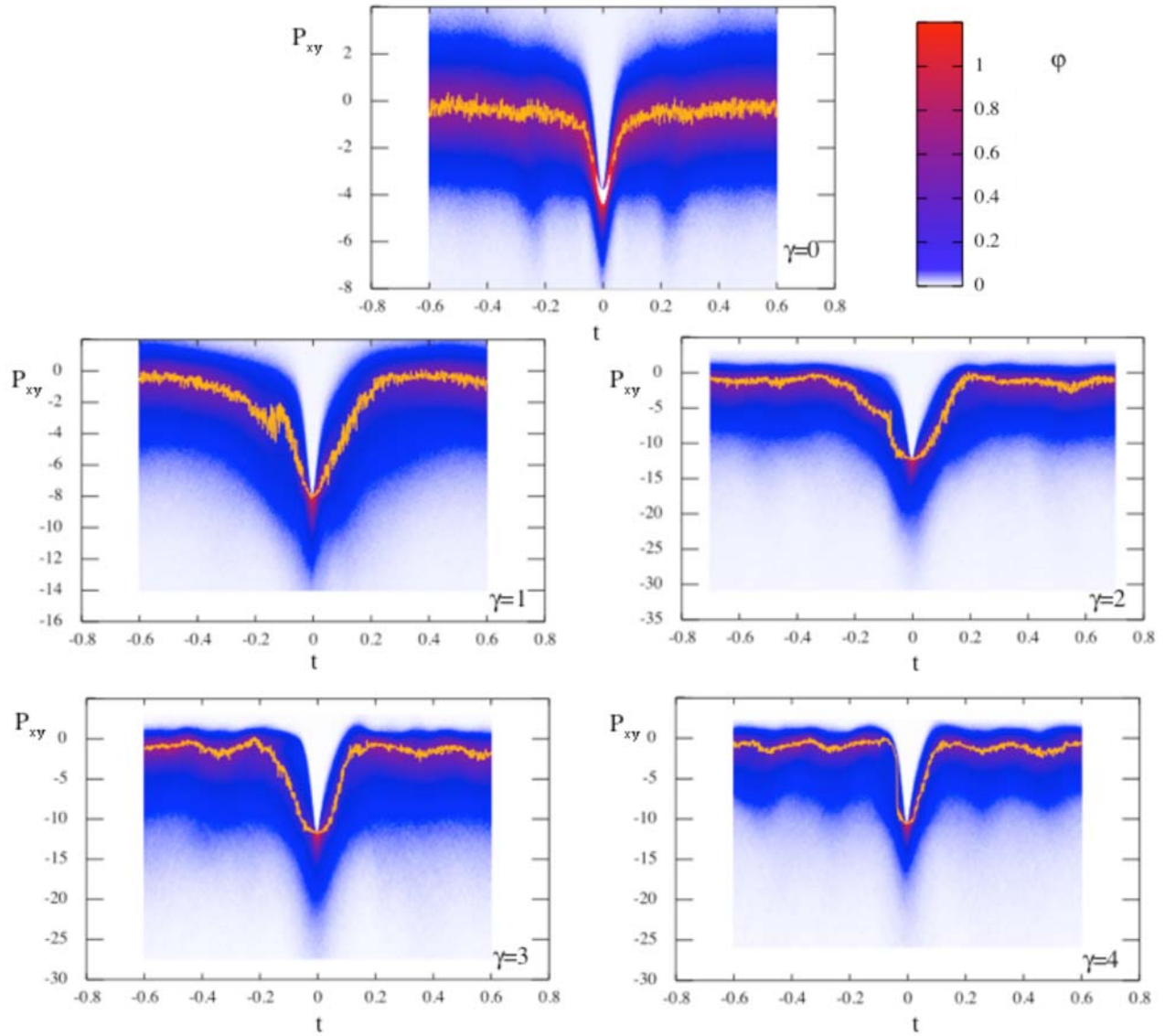


Figure 3-7 Histograms of shear stress (P_{xy}) trough fluctuation paths: synoptic plot for $\gamma = 0, 1, 2, 3, 4$ with “bird’s eye” view parallel to the frequency axis, using the first definition of fluctuation path. The colours in the legend refer to the values of ϕ . The gold line is a line through the ridge of the histograms.

Figure 3-8 presents the equivalent (γ ranging from 0 to 4 and $T_{hr} = \mu - 2.5\sigma$) histograms of trough fluctuation paths of shear stress obtained adopting the second definition. We note that, as distinct from the analysis with first definition of fluctuation path, the histograms plot the logarithm of the frequency φ . We are brought to this choice by the definition of fluctuation path employed. According to the second definition, the mid point of the fluctuation path is always equal to the threshold value T_{hr} . Therefore the maximum φ is very high, as all data will lie in one bin for $t=0$. Such a high density would obscure the values in the other points of the property-time grid.

Analogous to the first definition, the equilibrium fluctuation path appears to be perfectly symmetric, while the profiles become asymmetric out of equilibrium, as we are able to see from Figure 3-8.

Figure 3-9 shows, for $\gamma = 0, 1, 2, 3, 4$, the second definition trough fluctuation paths of shear stress, with “bird’s eye” view parallel to the frequency axis.

As is easy to see, temporal asymmetry emerges out of equilibrium regardless of the details in the definition of fluctuation paths.

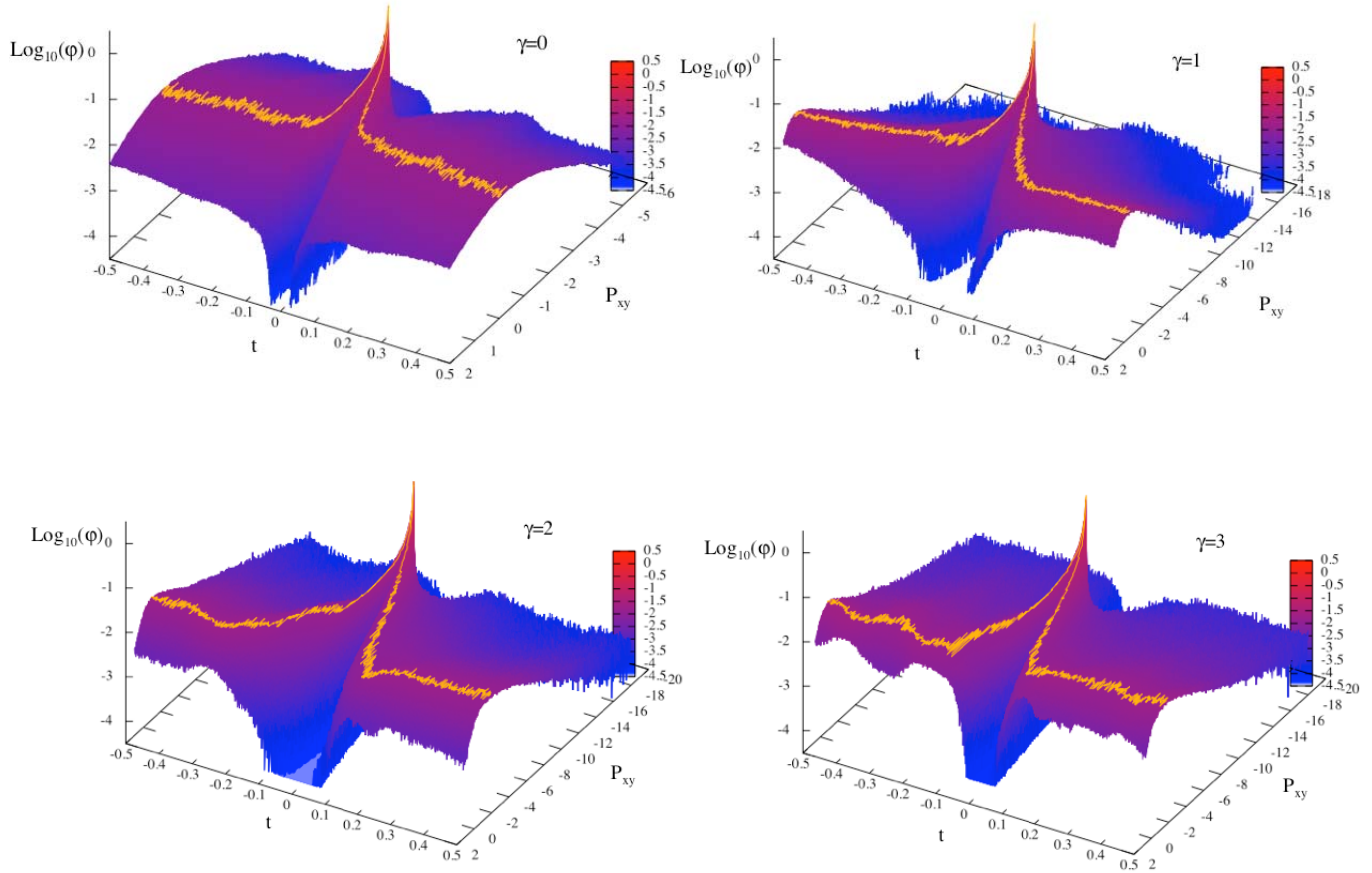


Figure 3-8 Histogram of shear stress (P_{xy}) trough fluctuation paths for various strain rates ($\gamma=0, 1, 2, 3$) using the second definition of fluctuation path. The colours in the legend refer to the values of ϕ . The gold line is a line through the ridge of the histograms.

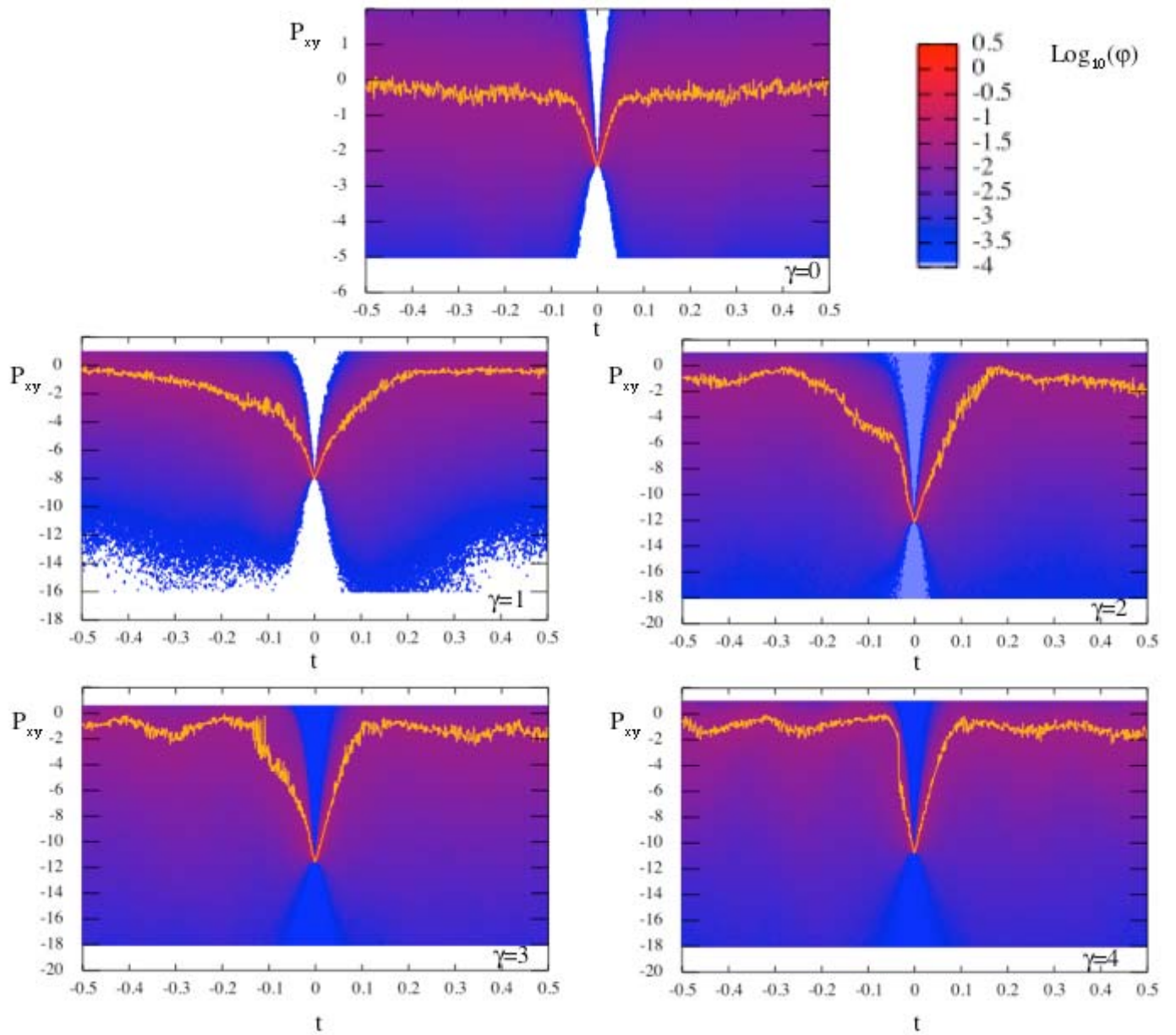


Figure 3-9 Histograms of shear stress (P_{xy}) trough fluctuation paths for $\gamma = 0, 1, 2, 3, 4$ with “bird’s eye” view parallel to the frequency axis, using the second definition of fluctuation path. The colours in the legend refer to the values of ϕ . The gold line is a line through the ridge of the histograms.

Temporal asymmetry appears to be a general feature of this nonequilibrium system. It is not only confined to odd properties, such as the shear stress P_{xy} . In Figure 3-10 we present the numerical results for the first definition fluctuation path of the internal energy E for various fields $\gamma = 0, 1, 2, 3, 4$, with thresholds T_{hr} set 2.5 times the standard deviation above the average. Internal energy is an even property under time reversal symmetry. As for shear stress, it is apparent that asymmetry seems to develop out of equilibrium even for the internal energy. Such behaviour is confirmed by our qualitative analysis on other even properties, such as the potential energy and the pressure, as shown in Figure 3-11 and in Figure 3-12. Similar results were also obtained for these properties using the second definition of fluctuation path. These graphical results suggested that asymmetry exists, at least at high fields. In the next section we will confirm this with a more careful, quantitative analysis.

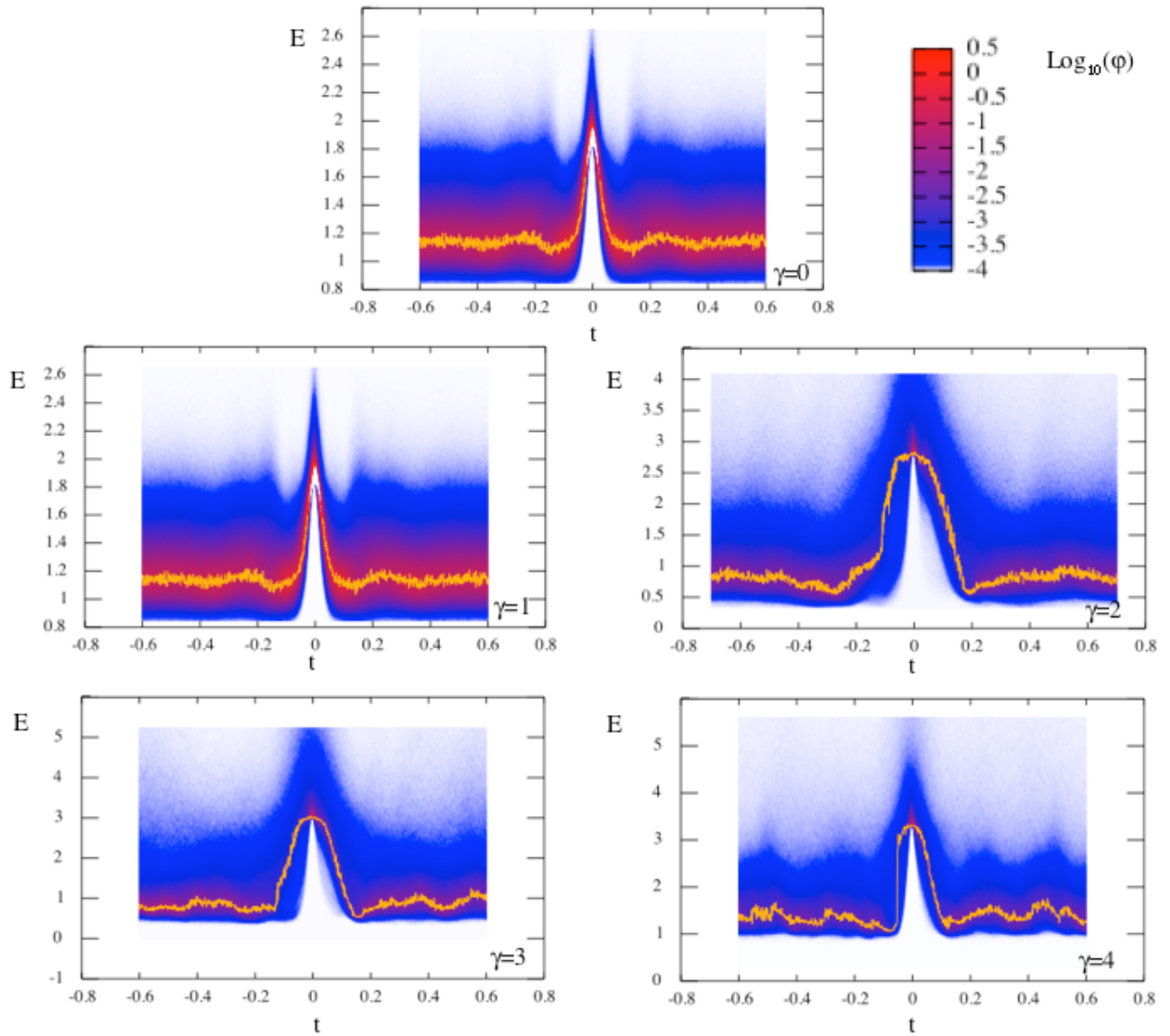


Figure 3-10 Histograms of internal energy E peak fluctuation paths: synoptic plot for $\gamma = 0, 1, 2, 3, 4$ with a “bird’s eye” view parallel to the frequency axis, using the first definition of fluctuation path. The colours in the legend refer to the values of φ . The gold line is a line through the ridge of the histograms.

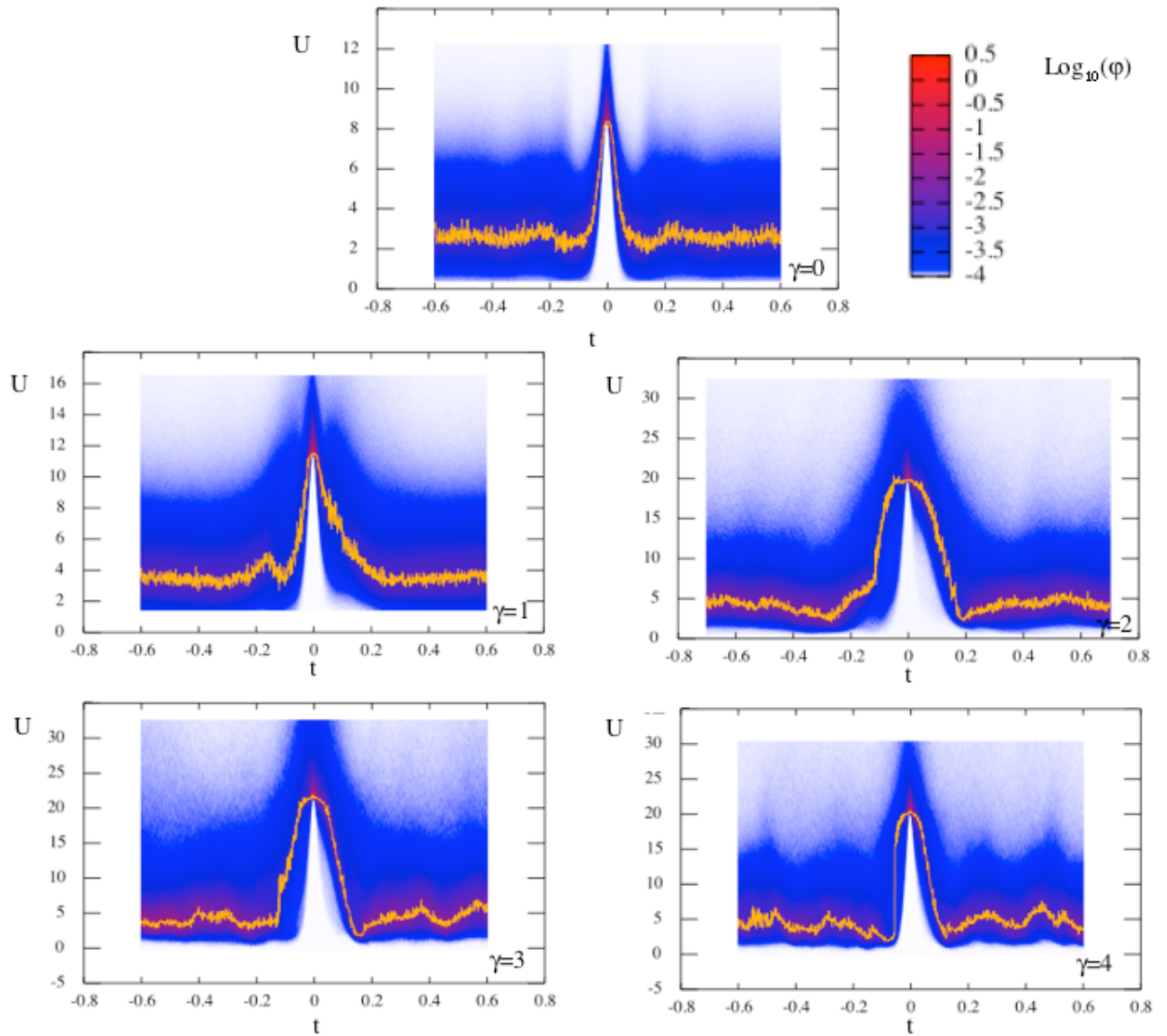


Figure 3-11 Histograms of potential energy U first definition peak fluctuation paths: synoptic plot for $\gamma = 0, 1, 2, 3, 4$ with a “bird’s eye” view parallel to the frequency axis. The colours in the legend refer to the values of ϕ . The gold line is a line through the ridge of the histograms.

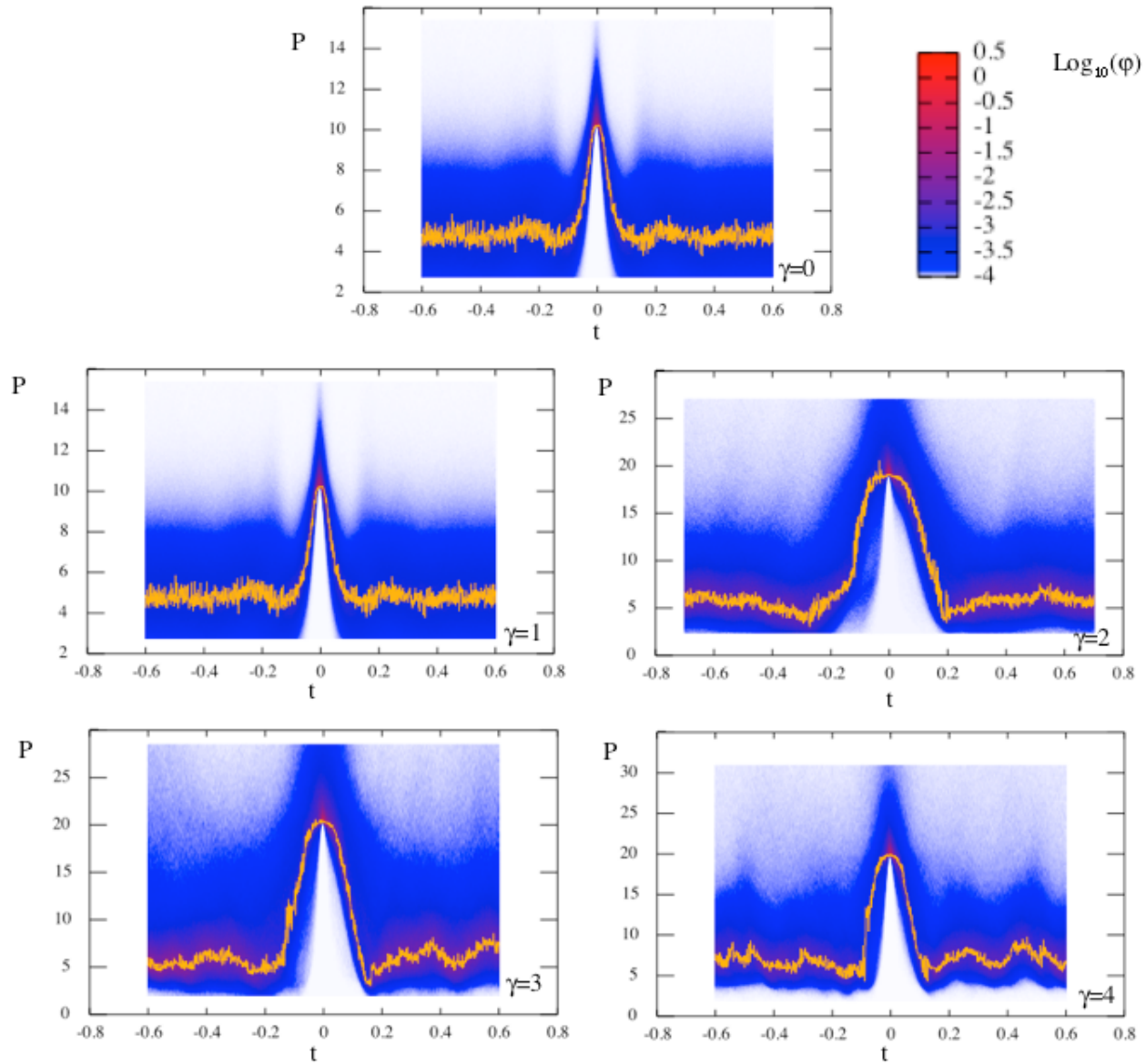


Figure 3-12 Histograms of first definition pressure p peak fluctuation paths: synoptic plot for $\gamma = 0, 1, 2, 3, 4$ with “bird’s eye” view parallel to the frequency axis. The colours in the legend refer to the values of φ . The gold line is a line through the ridge of the histograms.

3.2 Quantitative observation of asymmetry

In this section we present results for the full range of $\gamma = 0.05, 0.1, 0.2, 0.5, 1$ for the linear regime, and $\gamma = 2, 3, 4$ out of the linear regime, and we give a quantitative analysis of the temporal asymmetry.

We chose to focus our attention on two properties: the shear stress P_{xy} that is odd under time reversal symmetry, and the pressure P , that is even. The first step was to extract “typical” fluctuation paths from the numerical results using average and most probable paths. In the limit for large numbers of particles the two will coincide, as the only observable path is the most probable. This is not the case for our microscopic sample. We prefer to examine average paths because they are less demanding in terms of computational resources.

As an example, Figure 3-13 shows the average and the most probable fluctuation path obtained from the first definition, with threshold set two and a half times above the mean; the most probable fluctuations are the projections of the crest of the histograms of Figure 3-6 on the P_{xy} time plane.

Figure 3-14 shows the corresponding measure of asymmetry α_t (of both the average and most likely trough fluctuation paths), and it is apparent how asymmetry emerges only out of equilibrium.

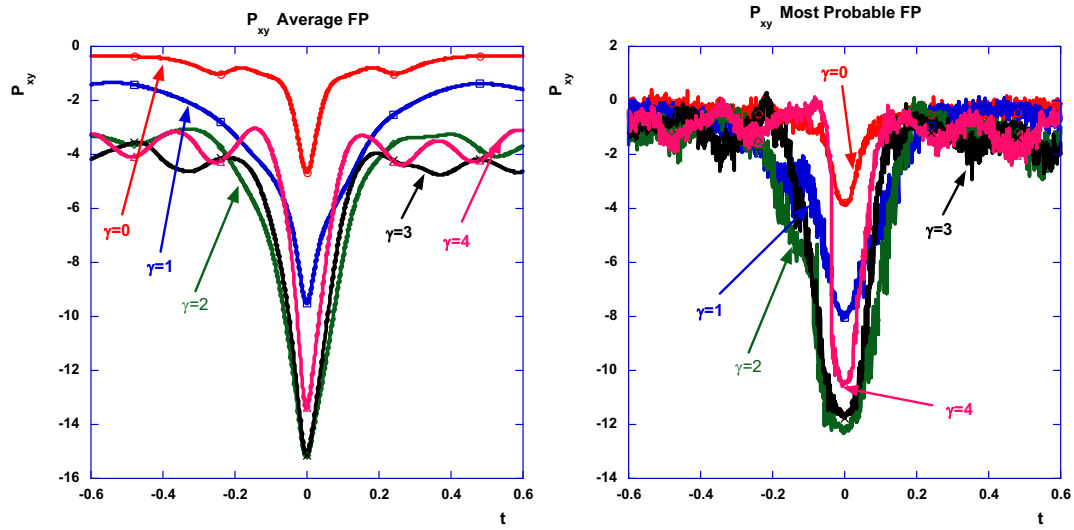


Figure 3-13 Average and most probable (the crest of the previous histograms) fluctuation paths of shear stress for various fields (first definition).

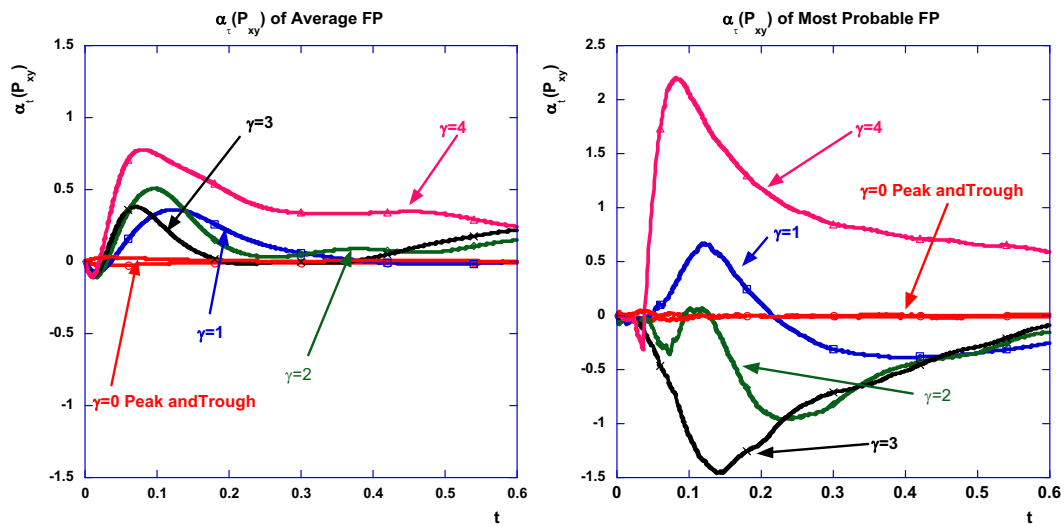


Figure 3-14 Measure of asymmetry of average and most probable fluctuation paths of shear stress for various fields (first definition).

However, we decided to abandon the first definition in favour of the second definition of fluctuation path adopted in reference [82], since it is physically reasonable and it is much more computationally efficient definition. The memory allocation required to take into account fluctuation paths that are wide and above the threshold, is too great

to take all results into account. We therefore proceed adopting the second definition of fluctuation path throughout this section.

Thresholds are set equal to $\mu - 1.5\sigma$ and $\mu - 2.5\sigma$ for P_{xy} (since we are monitoring its trough fluctuation paths) and to $\mu + 1.5\sigma$ and $\mu + 2.5\sigma$ for pressure (since we are monitoring its peak fluctuation paths). These fluctuation paths are collected for a time interval of duration 1. The most probable fluctuation paths are obtained from two-dimensional histograms of the values of P_{xy} and pressure, constructed collecting such values on rectangular grids with cells of width equal to the time step (in the direction of time) and of height 2×10^{-2} (in the direction of the observable).

Figure 3-15 shows the average (Figure 3-15 A) and most likely (Figure 3-15 B) trough fluctuation path of P_{xy} for various fields, with threshold set to $\mu - 2.5\sigma$.

Figure 3-16 shows the values of the measure of asymmetry α_i of the fluctuation paths; Figure 3-16 A shows α_i of the mean fluctuation path while Figure 3-16 B the corresponding for the most probable one. The average and most likely fluctuation paths and α_i 's are obtained as averages of ten runs. These values are plotted with error bars that are so small that the average α_i 's practically coincide with α_i 's of the corresponding average fluctuation paths. Importantly, for $\gamma = 0$, the α_i (of average and most likely fluctuation path of P_{xy}) is zero to within numerical error at all times.

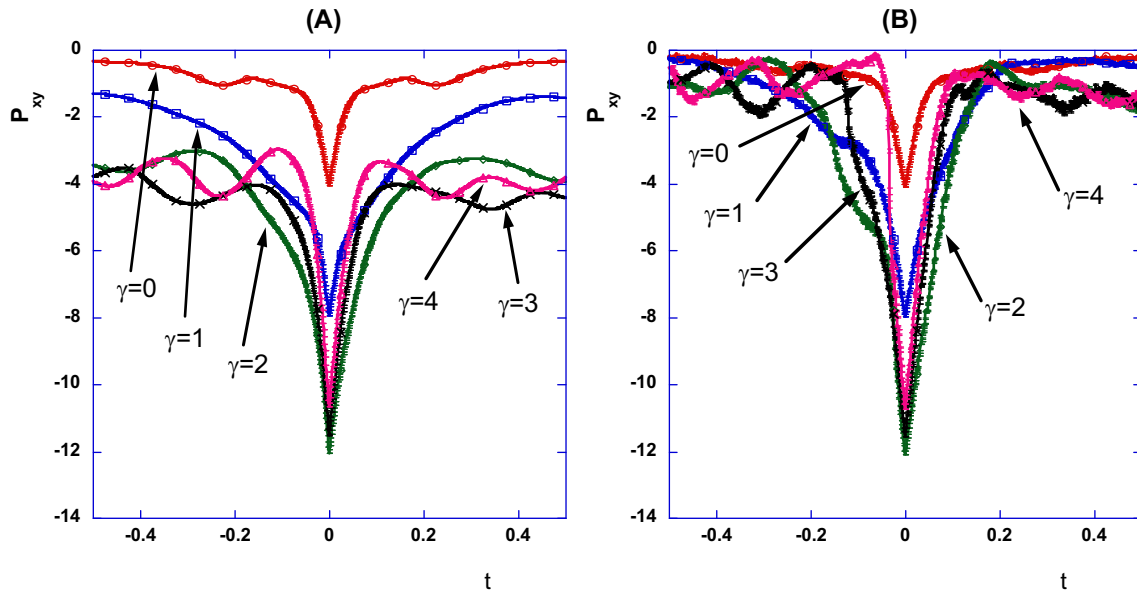


Figure 3-15 Average (A) and most probable (B) fluctuation path of shear stress P_{xy} with $T_{hr} = \mu - 2.5\sigma$. These are averages of 10 runs with error bars given by the standard error in the mean (which are often so small that they are not distinguishable in the plot).

Furthermore, at all other γ 's, asymmetry is evident: we can see that the α_t initially increases departing from 0; it reaches a maximum $\alpha_{\bar{t}}$ and starts decreasing. This behaviour is explained as follows. From the definition of $\alpha_{\bar{t}}$, it is obvious that this quantity vanishes at $t = 0$. For the fluctuation paths of P_{xy} with $\gamma \neq 0$ we observe a growth in $\alpha_{\bar{t}}$, as a consequence of the asymmetry of the fluctuation path around its central point, indicating that the approach to the peak is steeper than the departure from it. At a certain time $t > 0$, α_t starts to decrease, which is related to the decay of the correlations at the peak maximum and well into its wings.

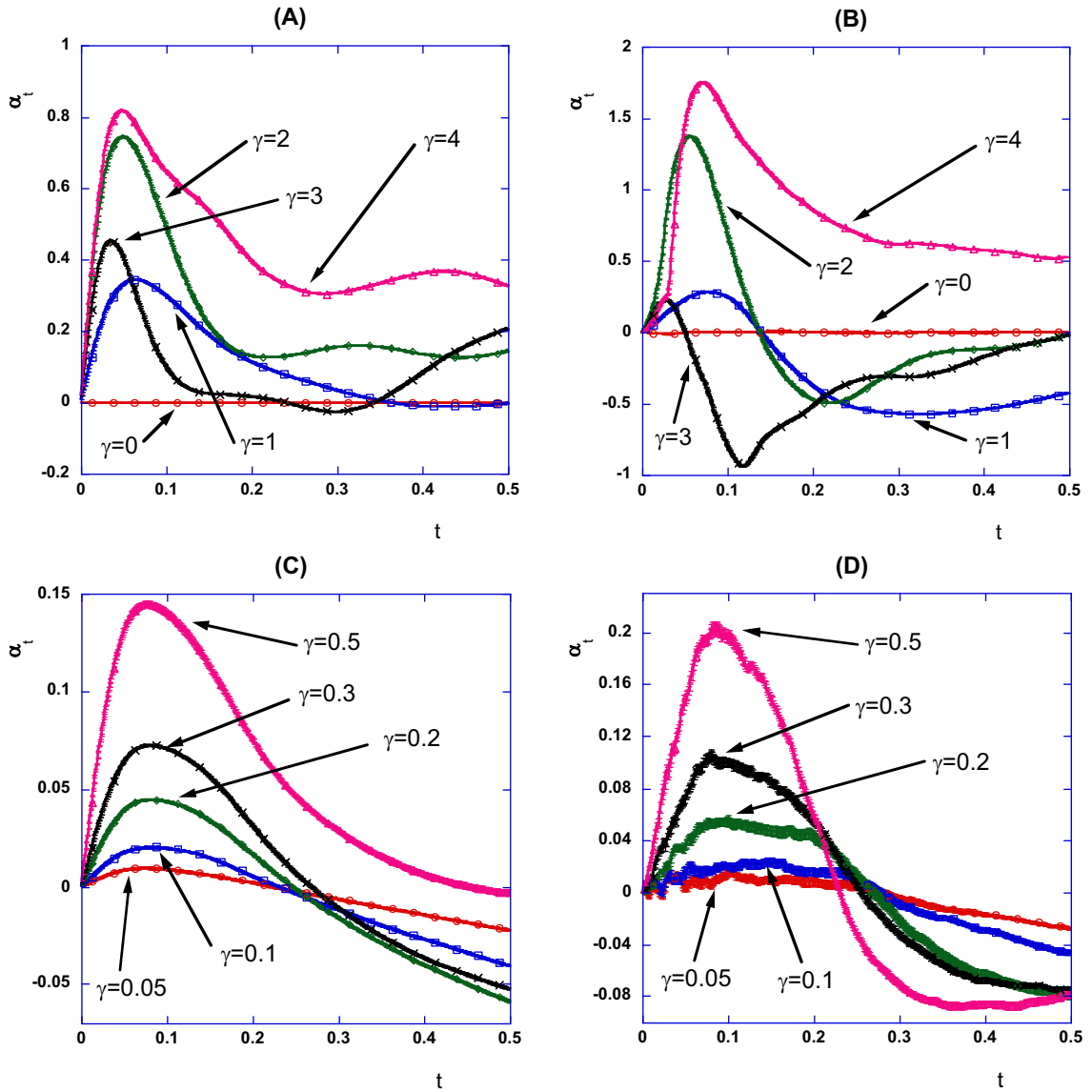


Figure 3-16 α_t of average (A and C) and most probable (B and D) FP of shear stress P_{xy} with $T_{hr} = \mu - 2.5\sigma$. These are averages of 10 runs with error bars given by the standard error in the mean (which are often so small that they are not distinguishable in the plot).

As shown in Figure 3-17, due to the high values of the selected thresholds, $t_r - t_d$ is small, so that the time interval between the approaching and departing paths can be considered to be equal to 2τ . Numerical results show that the maximum α_i of the

average fluctuation paths occurs at a time when the autocorrelations have decayed to

approximately $C\left(\left(P_{xy} - \langle P_{xy} \rangle\right), 2\tilde{t}\right) \approx \frac{1}{3}C\left(\left(P_{xy} - \langle P_{xy} \rangle\right), 0\right)$, where the

autocorrelation is defined as:

$$C\left(\left(P_{xy} - \langle P_{xy} \rangle\right), t\right) = \left\langle \left(P_{xy}(s^t \Gamma) - \langle P_{xy} \rangle\right) \left(P_{xy}(\Gamma) - \langle P_{xy} \rangle\right) \right\rangle \quad (3.1.1)$$

In these relations the ensemble average is over all Γ (not just peaks).

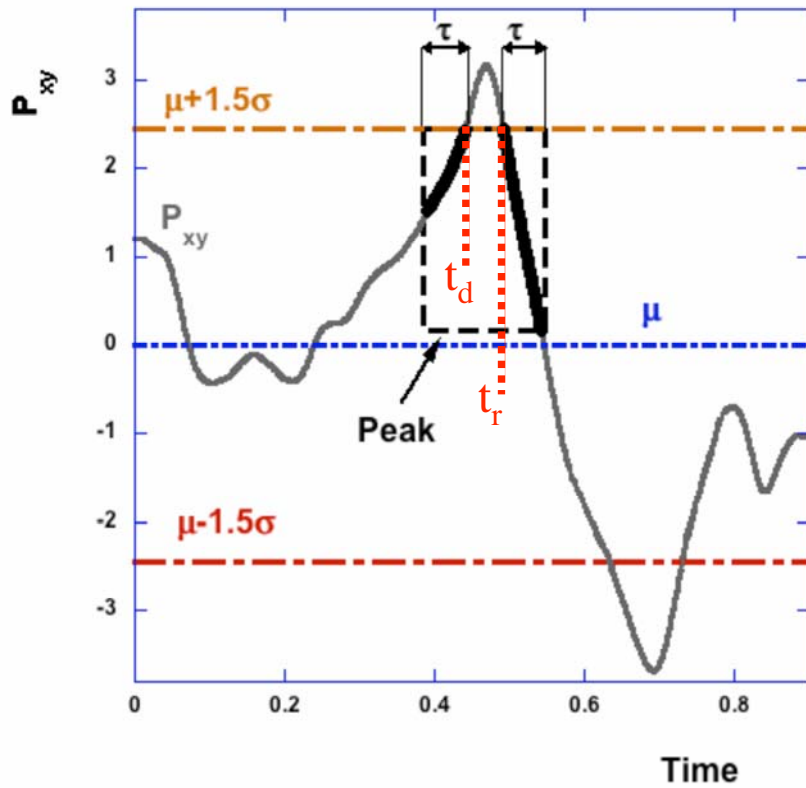


Figure 3-17 Construction of the second definition peak fluctuation path with reference to t_d and t_r .

Figure 3-18 displays the values of $C\left(P_{xy}, t\right)$ for t from 0 to 0.5. In a chaotic system, like ours, correlations decay with time (cf. Figure 3-18) so that the value of the observable A_t for large t 's, are uncorrelated from A_0 , and the “tails” of the fluctuation

path return to $\langle A \rangle$. This results in the value of $\lim_{z \rightarrow \infty} \frac{1}{z} \int_0^z (A_{-t} - A_{+t}) dt$ being zero, and

α_t decaying as $1/t$ at long t .

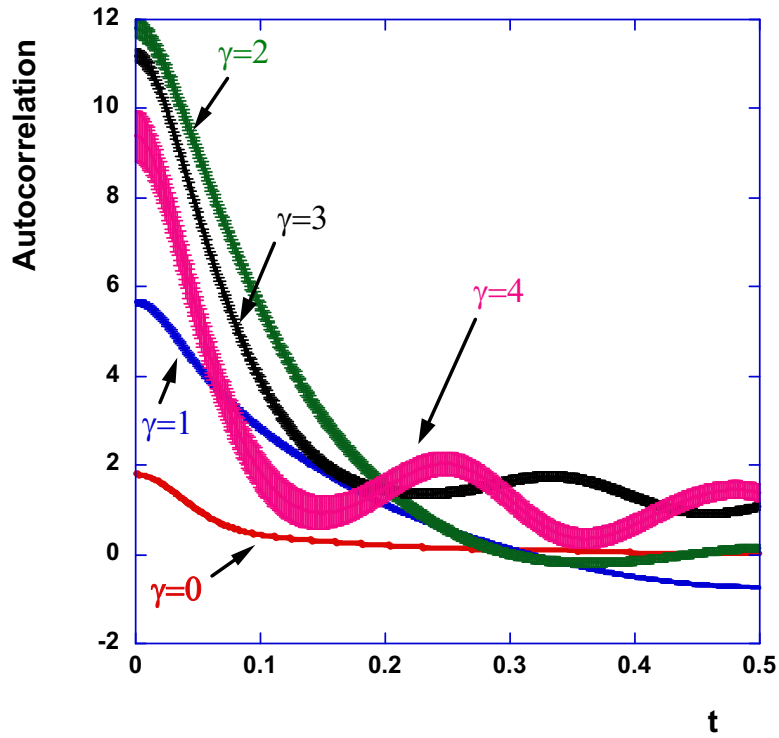


Figure 3-18 Autocorrelation function for the shear stress P_{xy} . These are averages of 10 runs with error bars given by the standard error in the mean (which are often so small that they are not distinguishable in the plot).

Figure 3-19 shows the corresponding $\langle \delta_t \rangle$ with $T_{hr} = \mu - 2.5\sigma$, in the linear regime.

Particularly interesting is the dependence of $\langle \delta_t \rangle$ on the field γ . We select an

arbitrary time $t = 0.05$ close to the peaks of the $\langle \delta_t \rangle$'s. Figure 3-20 shows $\langle \delta_t \rangle$ for

P_{xy} , at $t = 0.05$ as a function of γ , with $T_{hr} = \mu - 2.5\sigma$. δ_t grows with the field in the linear regime. By fixing T_{hr} at $\mu - 2.5\sigma$, there are two contributions to the growth of $\langle \delta_t \rangle$. Firstly there is a direct contribution which we would expect to be linear for the odd property P_{xy} , if the value of the threshold was fixed (see Chapter 5 for further discussion); then there is a growth due to an increase in the threshold, since μ increases linearly with γ .

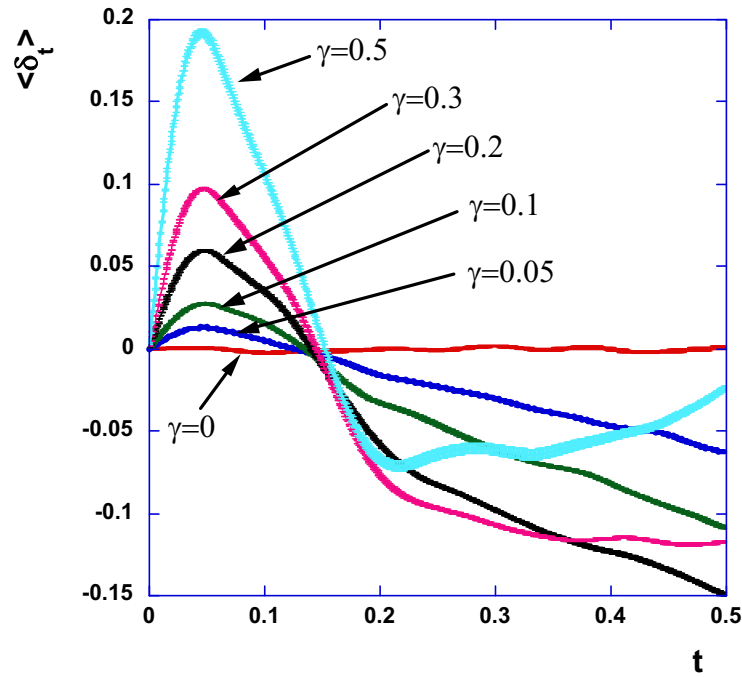


Figure 3-19 $\langle \delta_t \rangle$ of average fluctuation path of shear stress P_{xy} with $T_{hr} = \mu - 2.5\sigma$ in linear regime. These are averages of 10 runs with error bars given by the standard error in the mean (which are often so small that they are not distinguishable in the plot).

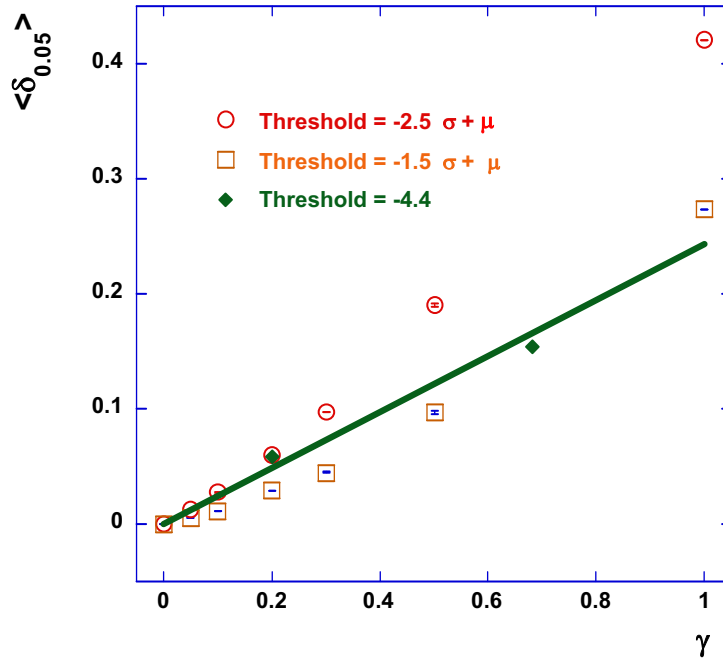


Figure 3-20 $\langle \delta_t \rangle$, with $t=0.05$ of average fluctuation path of shear stress P_{xy} with $T_{hr} = -2.5\sigma + \mu$ (red circles) and $T_{hr} = -1.5\sigma + \mu$ (orange squares) vs the shear flow γ , in the linear regime. The values of $\langle \delta_t \rangle$ for a threshold equal to -4.4 are shown as green diamonds.

In order to separate the dependence of $\langle \delta_t \rangle$ on T_{hr} and directly on γ , we should obtain data with fixed T_{hr} . By interpolation of a graph of T_{hr} vs γ for data obtained for $T_{hr} = \mu - 2.5\sigma$ and $T_{hr} = \mu - 1.5\sigma$, we found values of γ that, despite different μ and σ , give equal values of threshold T_{hr} . The values of $\langle \delta_t \rangle$ at those points, for a threshold equal to -4.4 , are shown as green diamonds. It is consistent with linear growth. It would be worthwhile in future work to obtain a more complete set of results using constant thresholds.

A set of simulations collecting fluctuation paths for a broader time interval was carried out so to see if the average P_{xy} fluctuation path would eventually reach the

average value $\langle P_{xy} \rangle$. From its definition and the decay of the correlations, we expect α_t to decay as $1/t$ for long t . The thresholds are the same as before but the fluctuation paths are collected for a time interval of 25. We focus on the average fluctuation path only, due to its smoother profile, and the results are shown as the dashed line in Figure 3-21. For efficiency data is not saved at each time step: the fluctuation paths are built from the averages, over 5 time steps, of the thermodynamic properties under interest. Once the properties have relaxed towards their steady state values, one finds small periodic oscillations of period $\pi = 1/\gamma$. In our case the amplitude of such oscillations on the left and on the right sides of the fluctuation path differ slightly; further to this, these oscillations do not appear to be exactly in phase. These results are due to the fact that t_d is not equal to t_r and $t_d - t_r$ is different for each peak or trough (even though, with high thresholds $t_d - t_r$ should tend to 0, refer to Figure 3-17). The period of these oscillations is the same as the one induced on the dynamics by the sliding brick boundary conditions $1/\gamma$, indicating that the oscillations are due to the periodicity of the algorithm. The results indicate that the maximum of the fluctuation path occurs at preferred alignments of the cells, in a small system, and this results in periodic oscillations in the fluctuation path. We need to show that the periodicity has a minimal influence on the degree of asymmetry observed at times close to the threshold crossing. Since these oscillations are completely periodic, it is easy to subtract this effect. In order to do so, we take the first oscillation from time $z = -t$ to time $z = -t + 1/\gamma$ of $X_t - \langle X \rangle$ and we extend it as a periodic function of period $1/\gamma$ up to $z = 0$. We repeat the same construction taking the last oscillation

from time $z = +t - 1/\gamma$ up to $z = t$ and we extend it backwards in time (starting from $z = t$) as a periodic function of same period down to $z = 0$ (This implies that most of the time the oscillations constructed from joining the two parts of a fluctuation path, result in a discontinuity at $t = 0$). Figure 3-21 A displays (for $\gamma = 1$ with threshold set to $\mu - 2.5\sigma$ and $2t = 25$) an example of the result of the above construction: the original fluctuation path and its profile when subtracted from the oscillation. Figure 3-21 B shows the corresponding α_i 's: it can be seen that qualitatively they do not differ at times close to zero, although the α_i of the fluctuation path without the oscillations now decays smoothly to 0 as $1/t$ for long t . Figure 3-22 and Figure 3-23 show that this holds for all the high γ 's, where the sliding brick condition continues to have significant effects, indicating that the computed asymmetries are a property of the system and not just an effect of the adopted algorithm. The α_i in Figure 3-23 now decay to zero as $1/t$ at long t , as expected.

Similar results have been obtained for P_{xy} with a threshold set to $\mu - 1.5\sigma$.

Fluctuation paths of shear stress P_{xy} with threshold set one and a half time below the mean ($T_{hr} = \mu - 1.5\sigma$) give results for the temporal symmetry that are analogous to those obtained with thresholds set at $\mu - 2.5\sigma$.

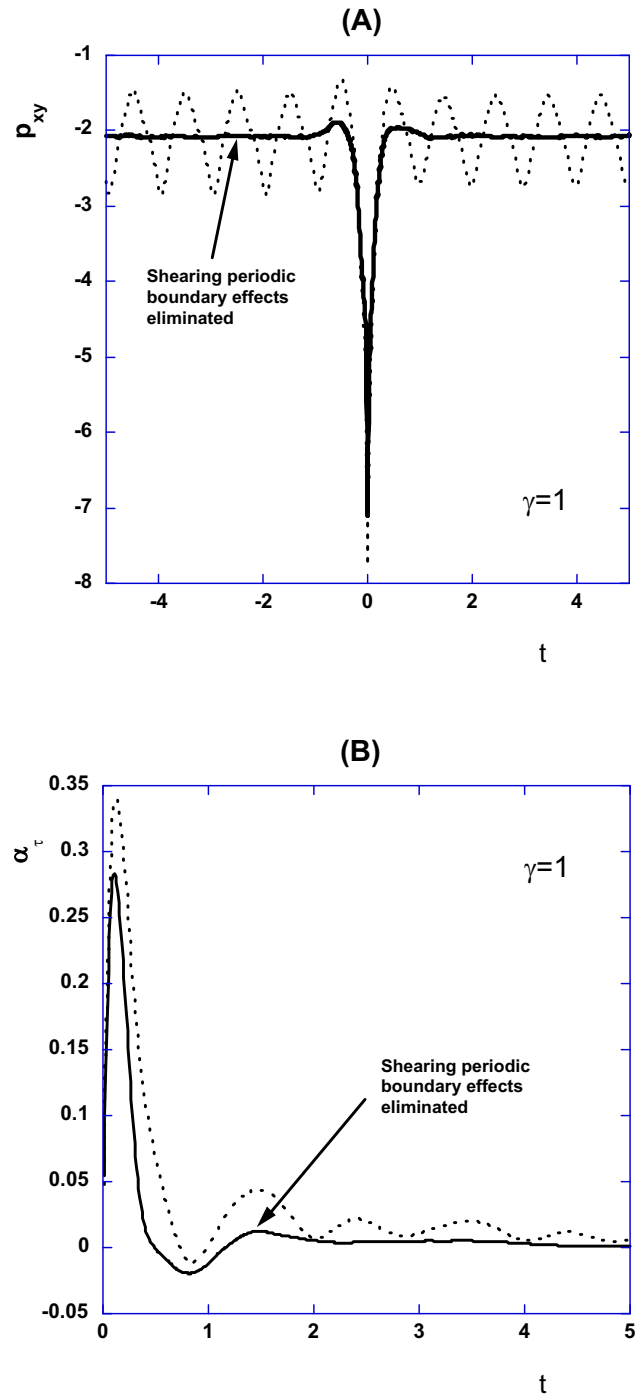


Figure 3-21 Average fluctuation path of P_{xy} together with its profile with the periodic oscillations due to the shearing boundaries removed for $\gamma = 1$ (A) and their α_t 's (B).

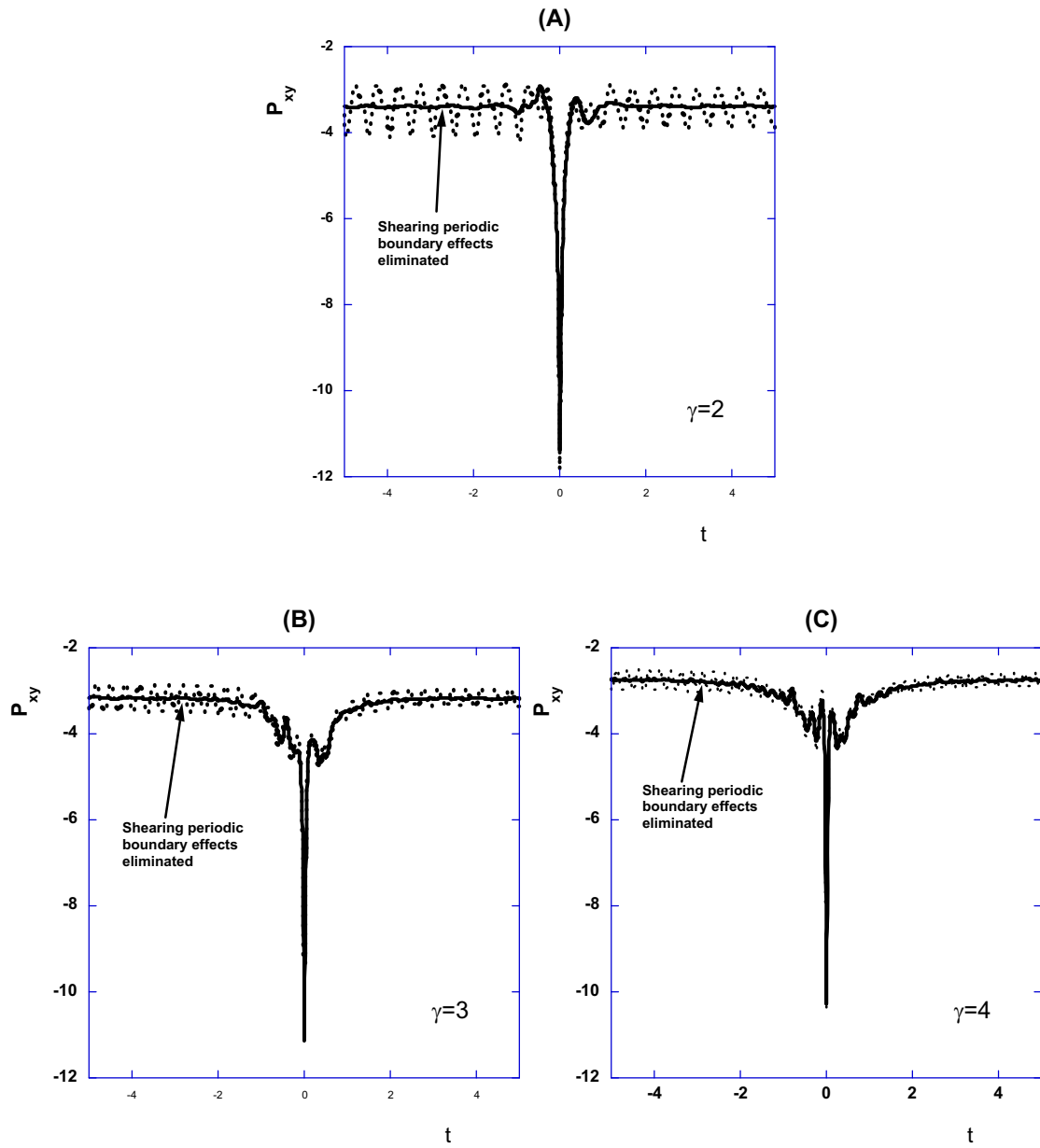


Figure 3-22 Average fluctuation path of P_{xy} together with its profile with the periodic oscillations due to the shearing boundaries removed for $\gamma = 2$ (A), $\gamma = 3$ (B) and $\gamma = 4$ (C).

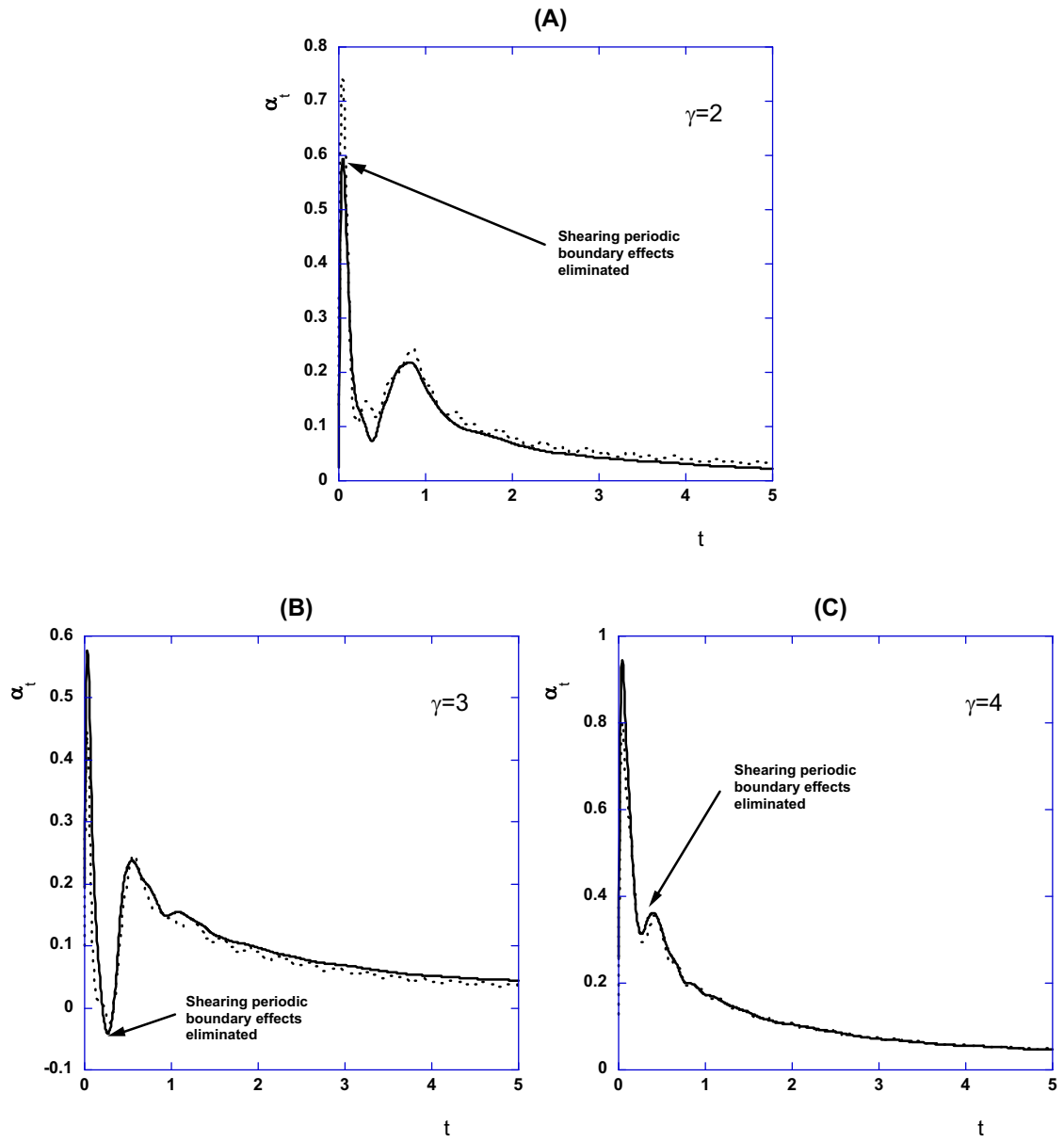


Figure 3-23 α_t of average fluctuation path of P_{xy} together with its profile with the periodic oscillations due to the shearing boundaries removed, for various high fields.

In Figure 3-24, the trough fluctuation paths of P_{xy} corresponding to a threshold set to $\mu - 1.5\sigma$ are shown. Figure 3-24A is the mean fluctuation path, while Figure 3-24B is the most probable one.

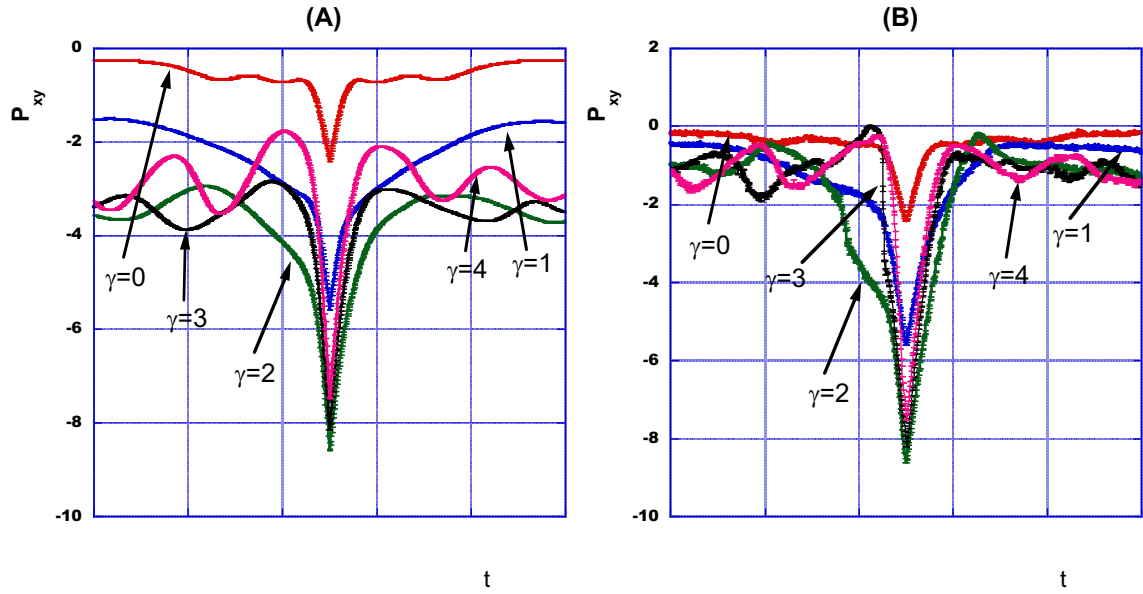


Figure 3-24 Average (A) and most probable (B) fluctuation path of shear stress P_{xy} with $T_{hr} = \mu - 1.5\sigma$. These are averages of 10 runs with error bars given by the standard error in the mean (which are often so small that they are not distinguishable in the plot).

Temporal asymmetry also emerges for ordinary fluctuation paths, as the threshold that the property has to exceed in order to be regarded was only $\mu - 1.5\sigma$. The phenomenon does not only seem to be confined to exceptional fluctuations (the fluctuations treated by stochastic theories).

Such asymmetry of fluctuation paths of P_{xy} with $T_{hr} = \mu - 1.5\sigma$ is measured by the

α_t 's displayed in Figure 3-25. Figure 3-25 A shows the α_t 's of the average

fluctuation paths, while Figure 3-25 B that of the most likely ones.

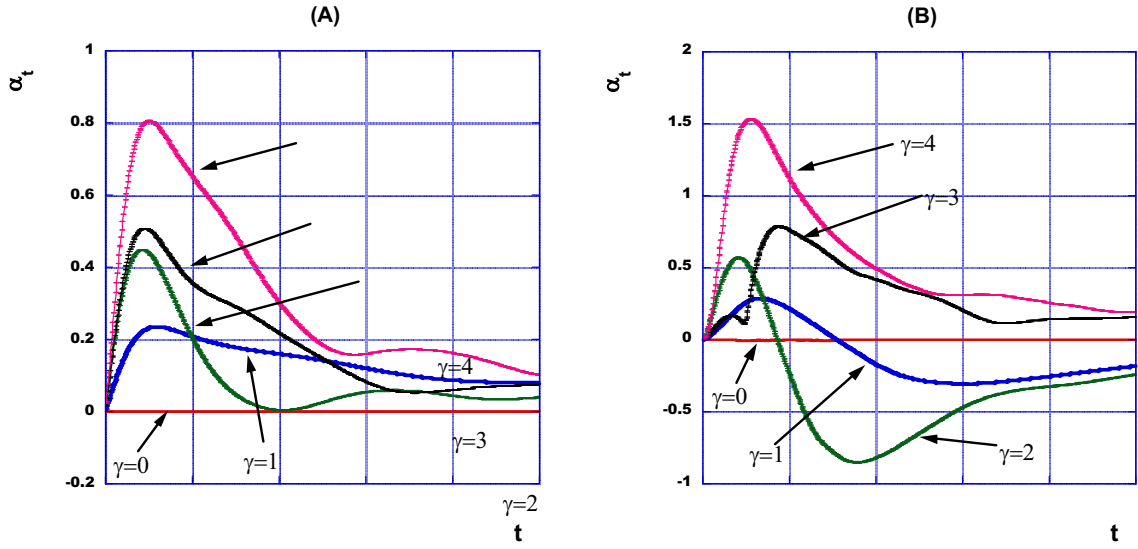


Figure 3-25 α_t of Average (A) and most probable (B) fluctuation path of shear stress P_{xy} with $T_{hr} = \mu - 1.5\sigma$. These are averages of 10 runs with error bars given by the standard error in the mean (which are often so small that they are not distinguishable in the plot).

Figure 3-20 also shows $\langle \delta_t \rangle$ at $t = 0.05$ of average fluctuation path of shear stress P_{xy} , with $T_{hr} = 1.5\sigma - \mu$, as a function of γ . As for the higher fluctuation paths (with $T_{hr} = 2.5\sigma - \mu$), in the linear regime the $\langle \delta_t \rangle$ at $t = 0.05$ increases with the field.

Analogueous results to those obtained for P_{xy} have been obtained for the pressure.

In Figure 3-26 we show the average peaks for pressure with $T_{hr} = \mu + 2.5\sigma$ and

Figure 3-27 shows the corresponding α_t 's.

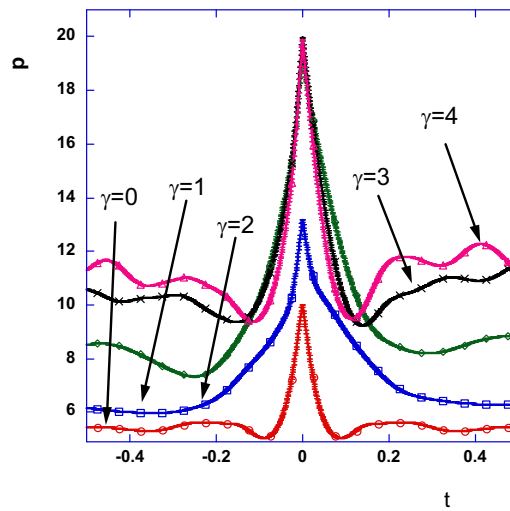


Figure 3-26 Average fluctuation path of pressure p , with $T_{hr} = \mu + 2.5\sigma$. These are averages of 10 runs with error bars given by the standard error in the mean (which are often so small that they are not distinguishable in the plot).

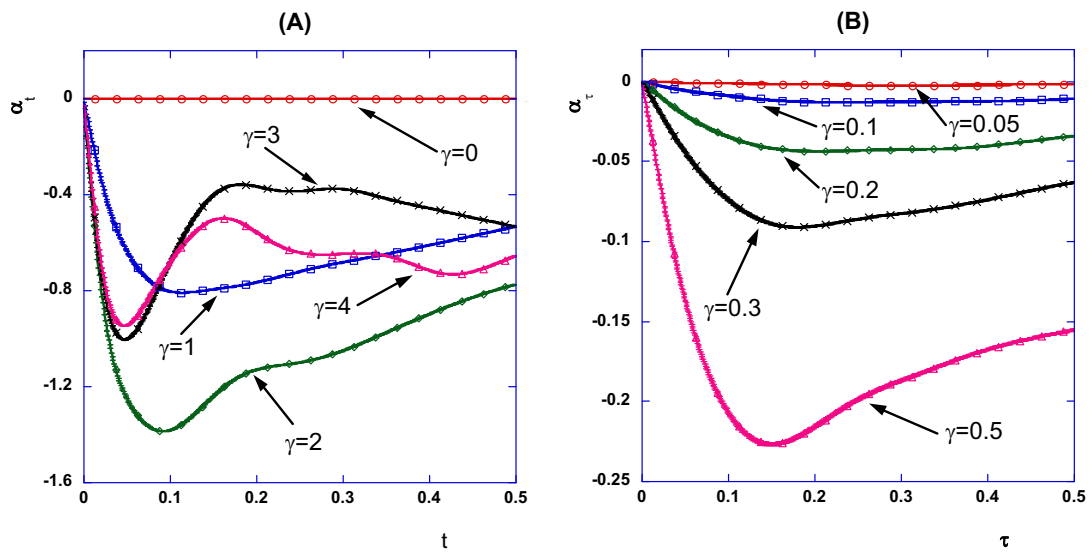


Figure 3-27 α_t of Average fluctuation path of pressure p with $T_{hr} = \mu + 2.5\sigma$.

These are averages of 10 runs with error bars given by the standard error in the mean. A shows the equilibrium and high field values; B shows samples of linear regime.

Their behaviour is very similar to that of P_{xy} (except for the sign of the different quantities), confirming asymmetry in this even property. The fact α_t is negative shows that, similarly to the peak fluctuation paths of P_{xy} , the approach to the peak is steeper than the relaxation from it for the average fluctuations of pressure and shear stress in Couette flow. Asymmetry out of equilibrium develops even for the most probable value of pressure. Figure 3-28 shows the maximum frequency value peaks for pressure with $T_{hr} = \mu + 2.5\sigma$ and Figure 3-29 shows the corresponding α_t 's.

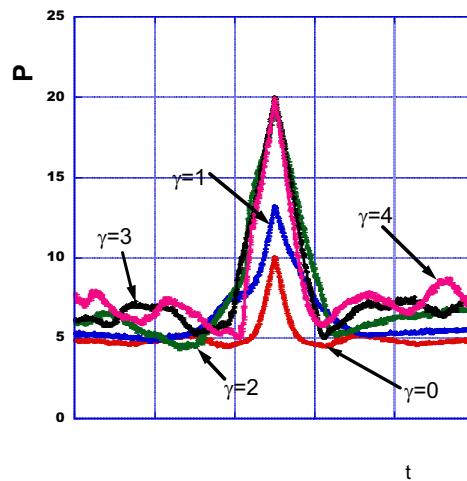


Figure 3-28 Maximum frequency value peak fluctuation path of pressure p , with $T_{hr} = \mu + 2.5\sigma$. These are averages of 10 runs with error bars given by the standard error in the mean (which are often so small that they are not distinguishable in the plot).

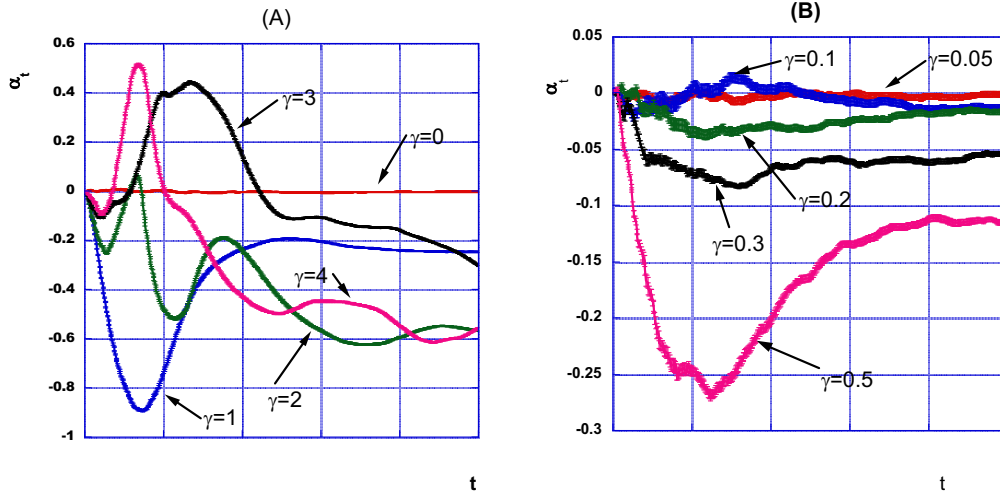


Figure 3-29 α_t of most probable fluctuation path of pressure P ($T_{hr} = \mu + 2.5\sigma$) .

These are averages of 10 runs with error bars given by the standard error in the mean (which are often so small that they are not distinguishable in the plot). **A** shows high values of γ , **B** the linear regime.

Figure 3-30 plots $\langle \delta_t \rangle$ at $t = 0.05$ of the average pressure P with $T_{hr} = \mu + 2.5\sigma$ and $T_{hr} = \mu + 1.5\sigma$ in function of the square of γ^2 . The maximum measure of asymmetry exhibits a quadratic dependence with γ within the linear regime. In this case the quadratic dependence of the mean on γ^2 as well as a quadratic dependence of $\langle \delta_t \rangle$ when T_{hr} is fixed is evident, as expected from theory (see Chapter 5 for further discussion). We note that this almost quadratic behaviour means that temporal asymmetries in even properties are generally difficult to observe in the linear regime.

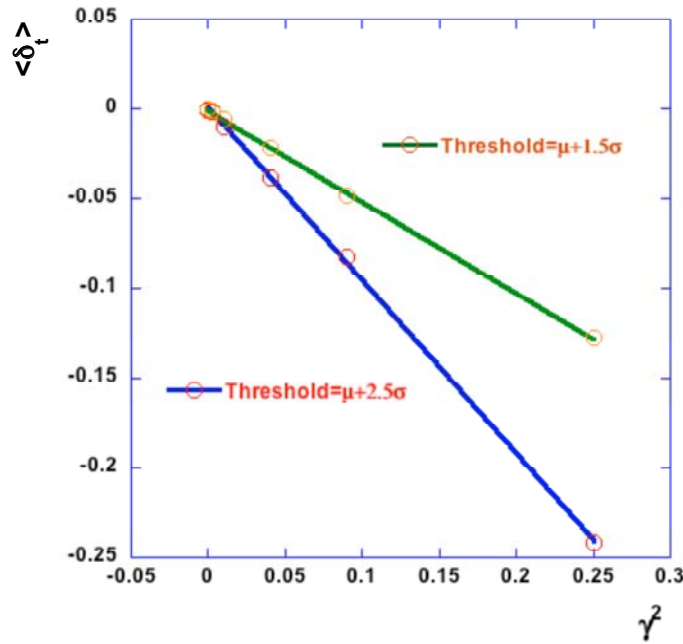


Figure 3-30 δ_t , with $t=0.05$ of average fluctuation path of pressure P with $T_{hr} = 2.5\sigma - \mu$ (red circles) and $T_{hr} = 1.5\sigma - \mu$ (red circles) vs the shear flow γ , in the linear regime. The lines are linear fits through the data showing a γ^2 dependence of δ_t .

3.3 Conclusions.

The departure from zero of the value of the measures of asymmetry, α_t and $\langle \delta_t \rangle$, if the system is away from equilibrium, is a numerical demonstration of asymmetry that occurs in fluctuation paths. This provides evidence for the first time that such behaviour, expected in stochastic nonequilibrium systems, can be found in the most common molecular dynamics representations of shearing fluids. The stochastic description of a physical system is of course a less detailed description than the deterministic microscopic one, which is obtained by coarse graining the reversible

deterministic dynamics, but which is not reversible anymore. In principle the irreversibility of the stochastic treatment could have been the cause of the emergence of temporal asymmetry. Our results show this is not the case. Furthermore, stochastic descriptions are not always appropriate.

We observe that asymmetry increases linearly with γ for P_{xy} at fixed threshold, and increases quadratically with γ for pressure in the linear regime. This will be explained in Chapter 5. The dependence is shown to be function of the parity. It means that, for even properties, temporal asymmetry will generally be difficult to observe in the linear regime.

Another important consideration that can be made from the simulations, is that temporal asymmetry is not only confined to exceptional fluctuations, but also in fluctuations that exceed the mean of 1.5 times the standard deviation. Stochastic theories were instead concerned with exceptional fluctuations and made no prediction on average fluctuations.

It is of conceptual interest to observe that such a subtle arrow of time can be found in perfectly reversible dynamics. Indeed the temporal asymmetry of fluctuation paths in our reversible dynamics is one manifestation of the emergence of macroscopic irreversibility starting from microscopic reversible evolution. Examination of the results shows that the statistical error in our data is small and not qualitatively affected by the computational method. Several open questions remain, which will be investigated in future chapters of the thesis. The first and most important is whether the phenomenon is relegated to shear flow, which has non-autonomous dynamics. We will therefore consider a system described by autonomous dynamics in Chapter 4.

Chapter Four: INITIAL NUMERICAL EXPERIMENTS: COLOUR DIFFUSION

4.1 Basic setup of the numerical experimental environment.

The present work was motivated by that of Gamba and Rondoni [81], who considered the asymmetry in fluctuations for the nonequilibrium Lorentz gas undergoing colour diffusion. This microscopic system, which is deterministic and time reversible, provided results that seem to be in contradiction with the mesoscopic theory, since asymmetry in the fluctuation paths was not observed. The simplified nature of the simulated system - composed of hard scatterers and of non-interacting particles- might justify the unexpected result. Such a result, however, made it important to verify the results using different nonequilibrium conditions: in particular it appeared worthwhile to analyse a similar system to the nonequilibrium state of the Lorentz gas in the experiments of Gamba and Rondoni; that is to subject the Lennard Jones fluid to a colour force field. Furthermore, as SLLOD is non-autonomous, it is important to study a system with autonomous dynamics such as colour diffusion, to see if the emergence of temporal asymmetry is really a general feature of deterministic and reversible systems. For colour diffusion, we focus our attention on the fluctuations of the colour flux J_x and of pressure P . The choice of colour flux J_x is obvious, as it is the flux coupled to the force that drives the system out of equilibrium -the colour field F_C . Since J_x is odd under time reversal symmetry, we also chose to study an even property, the pressure P , for consistency with the previous experiments. Referring to Section 2.3 in Chapter 2, for this series of experiments we constrain the kinetic

temperature defined as $\frac{(3N-4)}{2}k_B T = \frac{1}{2} \sum_{i=1}^N \frac{\mathbf{p}_i^{Pecul} \cdot \mathbf{p}_i^{Pecul}}{m_i}$ and the equations of motion are given by (2.3.11), (2.3.12) and (2.3.13).

Analogously to the experiments on shear flow, the first step in our colour diffusion experiments has been to examine where the linear regime extends to, so that we know if we are observing fluctuation paths within or outside of the domain of linear transport theory. As for the previous chapter, we adopt the second definition of fluctuation path (refer to Section 2.4.2 of Chapter 2): i.e. we observe the fluctuations as they approach and leave the threshold from a value closer to the mean.

Two-dimensional colour diffusion molecular dynamics simulations have been carried on a primitive cell containing 8 particles with reduced density equal to 0.8, kinetic temperature fixed at 1 and time step of 10^{-3} . At equilibrium (colour field $F_C=0$) and for colour field $F_C=1, 2, 3$ and 5, ten sets of simulations of 5×10^5 time steps each have been carried out.

Average values from these runs of colour diffusion J_x have then been plotted with respect to F_C , together with error bars, in Figure 4-1 A.

The test run simulations showed that the linear regime extends to colour fields equal to somewhere between 2 and 3, as it is shown in Figure 4-1B. Therefore subsequent simulations are run at equilibrium ($F_C = 0$), in the linear regime ($F_C = 1, 2$), at an intermediate field $F_C = 3$, and well out of the linear regime ($F_C = 5$). As for the Couette flow numerical experiments, at equilibrium ($F_C = 0$) the simulations have the

aim of verifying the suitability of our framework to the task of detecting temporal asymmetry.

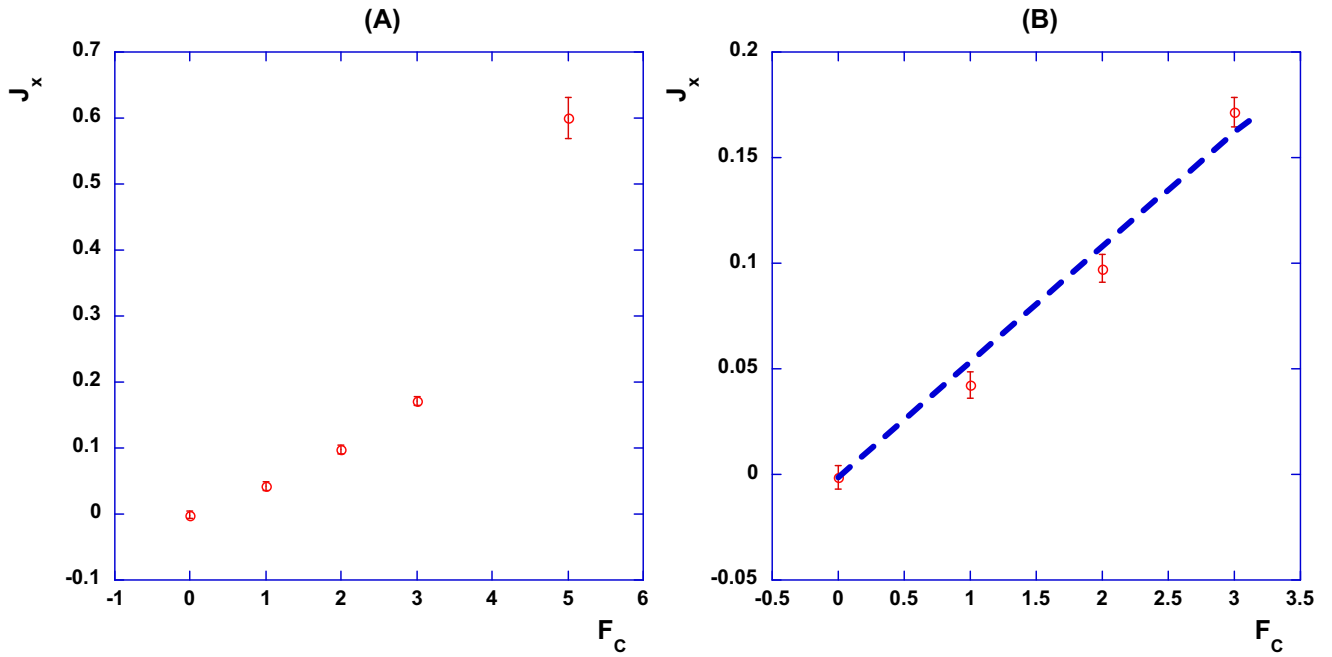


Figure 4-1 A) Average values of colour flux J_x vs colour field F_c . B) A closer view of the linear regime. The values of J_x are obtained from 10 sets of simulations of $5 \cdot 10^5$ time steps each. Error bars equal to the standard deviation out of the ten runs are plotted. The dashed line is a least squares fit through the data for $F_c = 0, 1, 2, 3$. It has a regression coefficient of 0.99289

Table 4-1 presents the means and standard deviations of the properties colour flux J_x and pressure P obtained from the sets of ten runs for colour field F_C equal to 0,1,2,3,5. Our interest is towards fluctuations that largely deviate from the mean, as in the case of shear flow; we therefore select the threshold value to be two and a half times the standard deviation from the mean.

Table 4-1 Mean μ and standard deviation σ of colour flux J_x and pressure P from 10 runs of 5×10^5 time steps for different colour fields F_C .

F_C	$\mu(J_x)$	$\sigma(J_x)$	$\mu(P)$	$\sigma(P)$
0	-0.00105459	0.00552164	6.1699647	0.02736428
1	0.04260152	0.00623772	6.1966469	0.03584121
2	0.09745269	0.00645693	6.281324	3.96E-02
3	0.17160809	7.01E-03	6.4427215	0.03424273
5	0.59998261	0.0310727	7.204467	0.04479972

To decide on whether to set the threshold above or below the mean, we refer to the distributions of the properties for each field. Figure 4-2 shows plots of sample values of colour flux J_x obtained from steady state simulations with colour field F_C set to 0, 1, 2, 3 and 5. The lines in blue represent thresholds set 2.5 times above and below the mean. The bias in the distribution is not strong, except for very high values of field F_C as 5: this means that it is possible to observe significant numbers of fluctuation paths above and below the mean.

For pressure instead, which is a positive function, large deviations (several standard deviations from the mean) are observed on one side of the mean only: the distributions of values are skewed towards the higher positive values. This bias in the distribution meant it would be pointless to set the threshold below the mean for

pressure, as we would not be able to observe any fluctuation at all.

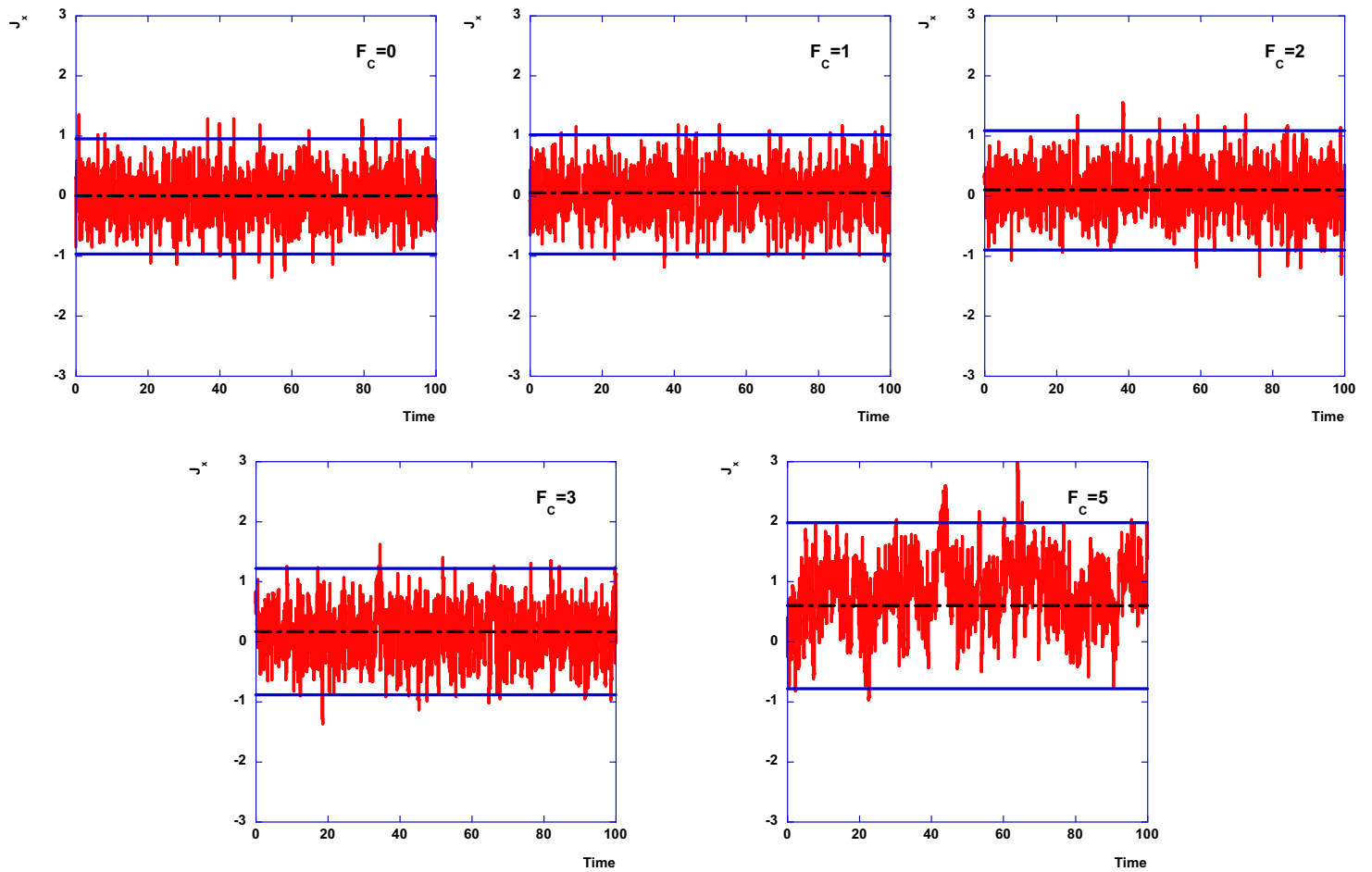


Figure 4-2 Sample values of colour flux J_x with colour field $F_c=0, 1, 2, 3, 5$.

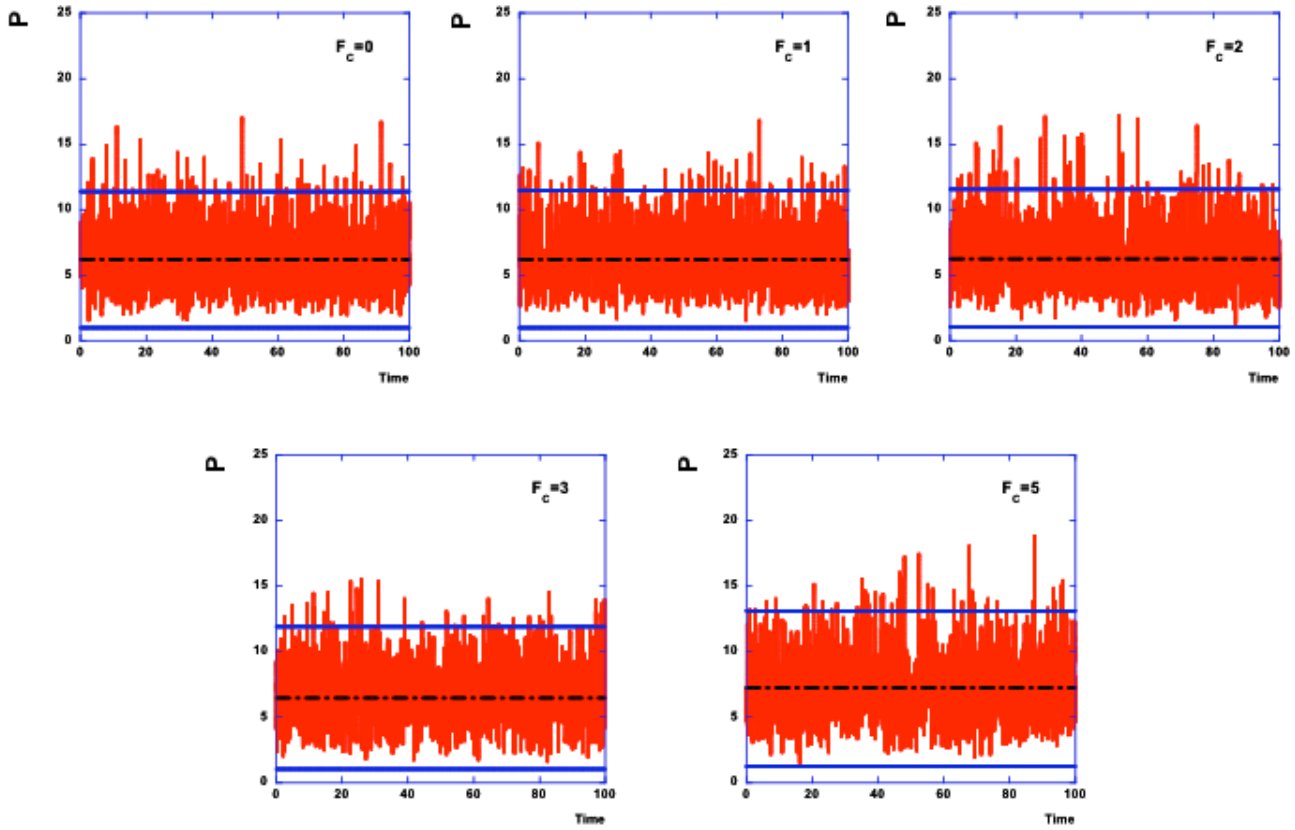


Figure 4-3 Sample values of pressure P with colour field $F_c=0, 1, 2, 3, 5$.

4.2 Numerical results

On the basis of the data of Table 4-1, sets of 10 - 20 simulations of 3×10^8 time steps have been carried out for each value of the colour field. During each run the peak and trough fluctuation path are collected for J_x and only peak fluctuation paths are collected for pressure, with thresholds set to $\mu \pm 2.5\sigma$ for J_x and to $\mu + 2.5\sigma$ for pressure. Fluctuation paths are collected for a time interval of duration 2 (instead of 1, as done for Couette flow) so that they have time to relax to the steady state.

Our analysis will focus on the average and on the most probable fluctuation path, obtained from two-dimensional histograms of the values of J_x and pressure,

constructed collecting such values on rectangular grids with cells of width equal to the time step (in the direction of time) and of height 2×10^{-2} (in the direction of the observable).

4.2.1 Fluctuation paths of colour flux

Figure 4-4 displays the equilibrium ($F_C=0$) histograms of colour flux J_x fluctuation paths with a “bird’s eye” view parallel to the frequency axis; φ is the measure of frequency, defined as the number of occurrences divided by the number of observations of the most frequent value of J_x . The histograms plot the logarithm of the frequency φ . As for the experiments for shear flow, we are brought to the choice of a logarithmic plot by the definition of fluctuation path employed, since the second definition fluctuation path presents an extremely high density of the threshold value in the fluctuation time midpoint: such a high density would obscure the values in the other points of the property-time grid if not on a logarithmic plot.

The peak and trough fluctuation paths ($T_{hr} = \mu \pm 2.5\sigma$) are compared and, as expected, they are the mirror image of each other about the plane $J_x = \mu(J_x) = 0$.

This confirms qualitatively for colour diffusion that the model exhibits symmetric values of peak and trough fluctuation paths at equilibrium; and this it is a necessary requirement for our system to exhibit the expected physical behavior.

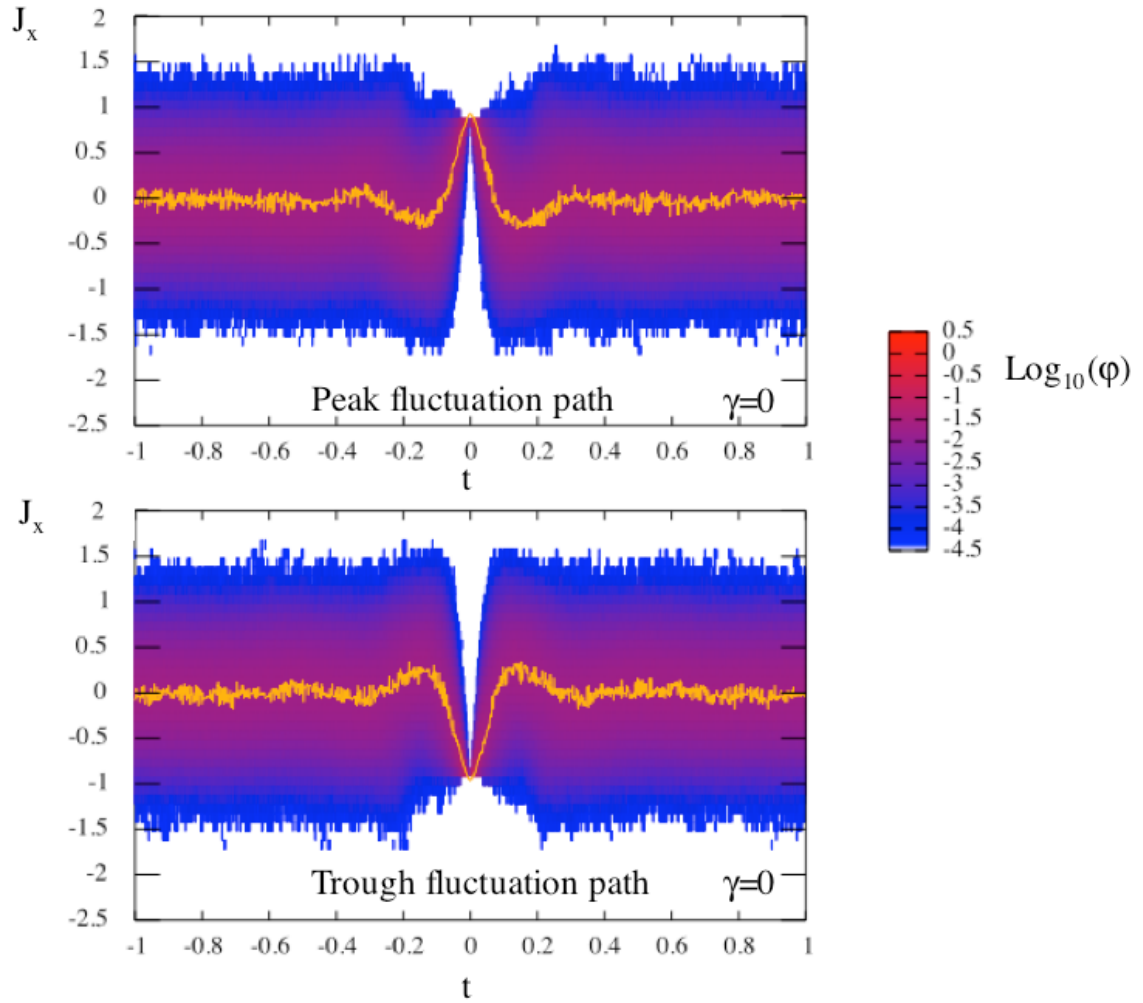


Figure 4-4 Histograms of colour flux (J_x) peak and trough fluctuation paths at equilibrium $F_C=0$ with threshold T_{hr} set to 2.5 times the standard deviation below and above the mean with a “bird’s eye” view parallel to the frequency axis. The colours in the legend refer to the values of $\log_{10}(\phi)$. The gold line is a line through the ridge of the histograms.

Figure 4-5 shows the histograms of the peak fluctuation paths of colour flux for fields F_C ranging from 0 to 3 with $T_{hr} = \mu + 2.5\sigma$: the symmetry of the profiles becomes irregular out of equilibrium, while the equilibrium fluctuation path appears to be symmetric.

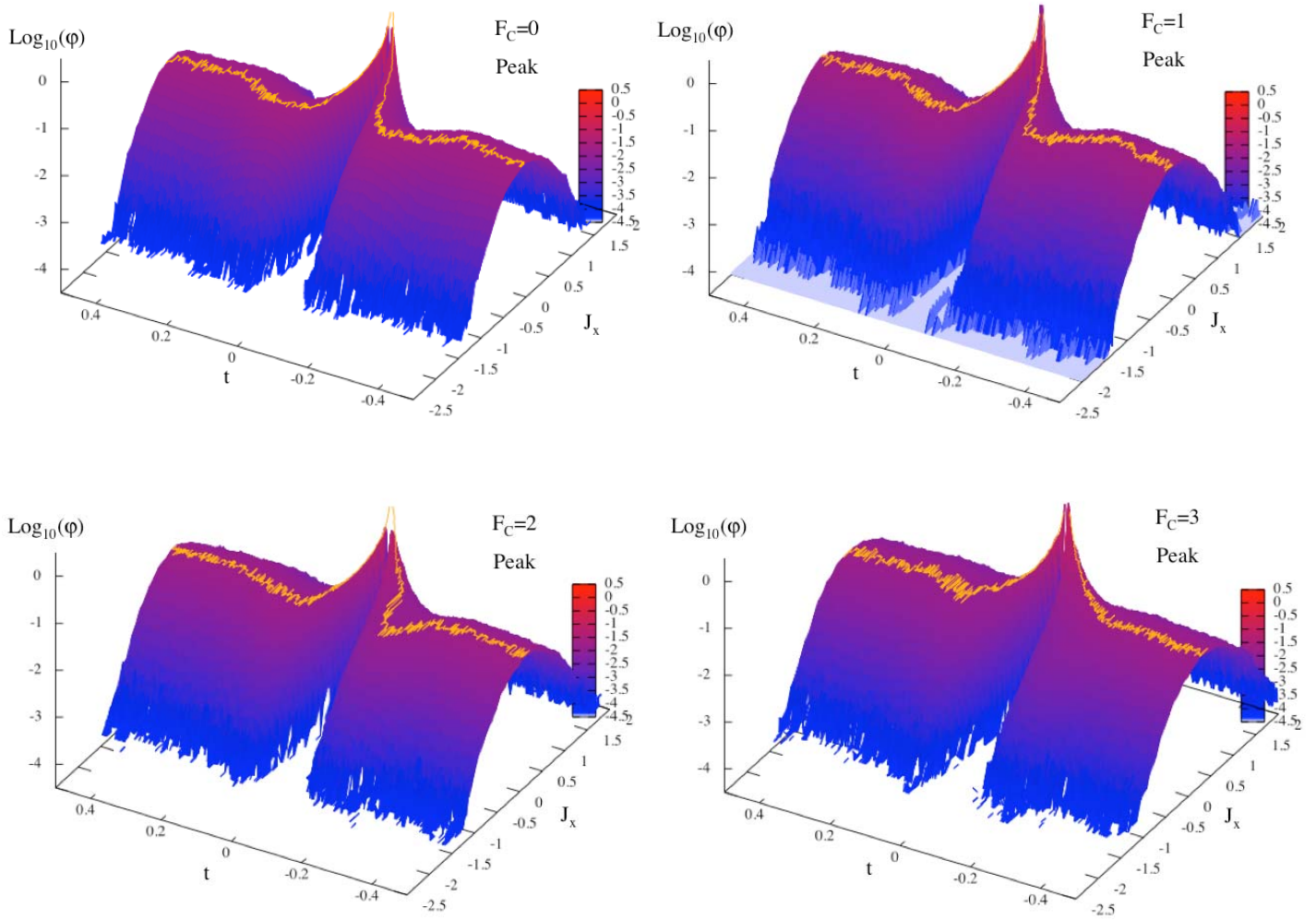


Figure 4-5 Histogram of colour flux (J_x) peak fluctuation paths for $F_C=0, 1, 2, 3$ with threshold $T_{hr} = \mu + 2.5\sigma$. The colours in the legend refer to the values of $\log_{10}(\varphi)$. The gold line is a line through the ridge of the histograms.

In Figure 4-6 we present the synoptic plots for peak fluctuation paths of colour flux J_x with “bird eye” view parallel to the frequency axis, for $F_C = 0, 1, 2, 3, 5$.

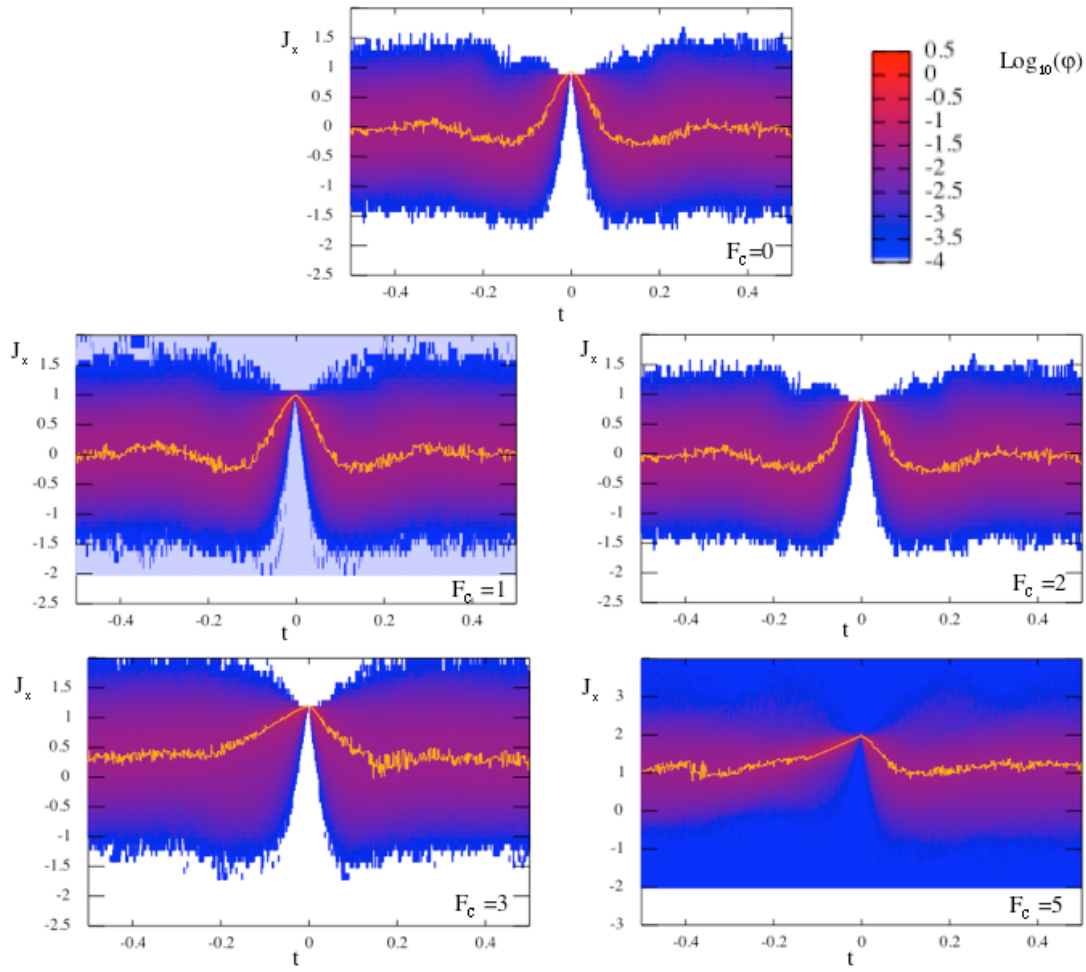


Figure 4-6 Histograms of colour flux (J_x) peak fluctuation paths with $F_c = 0, 1, 2, 3, 5$, threshold $T_{hr} = \mu + 2.5\sigma$, with a “bird’s eye” view parallel to the frequency axis. The colours in the legend refer to the values of $\log_{10}(\varphi)$.

The gold line is a line through the ridge of the histograms.

Figure 4-7 shows the most probable peak fluctuation path of J_x for various fields, with threshold set to $\mu + 2.5\sigma$, while Figure 4-8 is the corresponding average one.

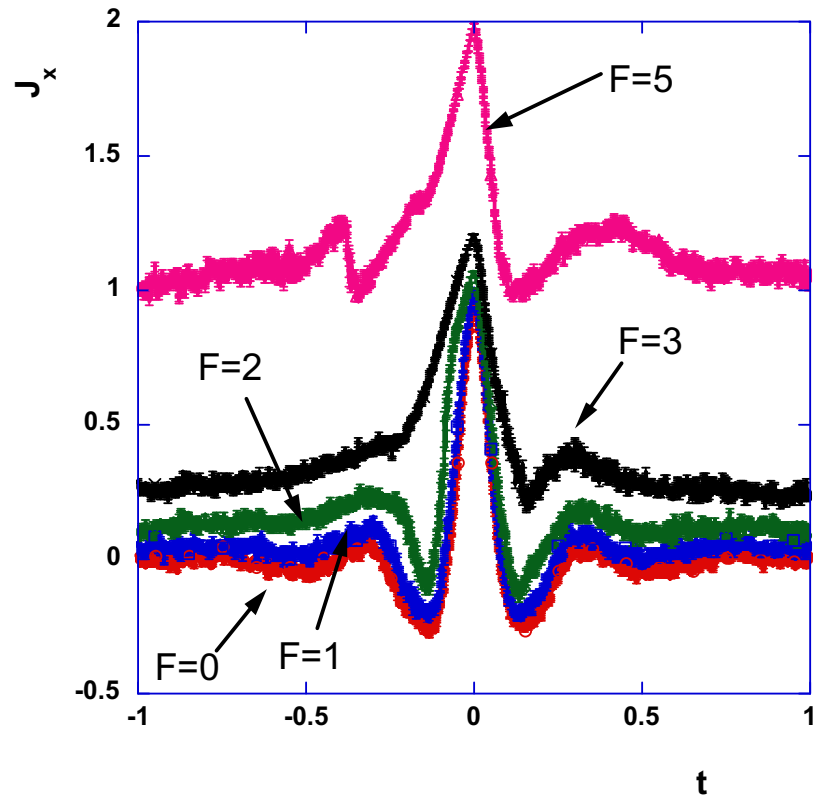


Figure 4-7 Most probable fluctuation path of colour flux J_x with $T_{hr} = \mu + 2.5\sigma$. These are averages of 10 runs with error bars given by the standard error in the mean.

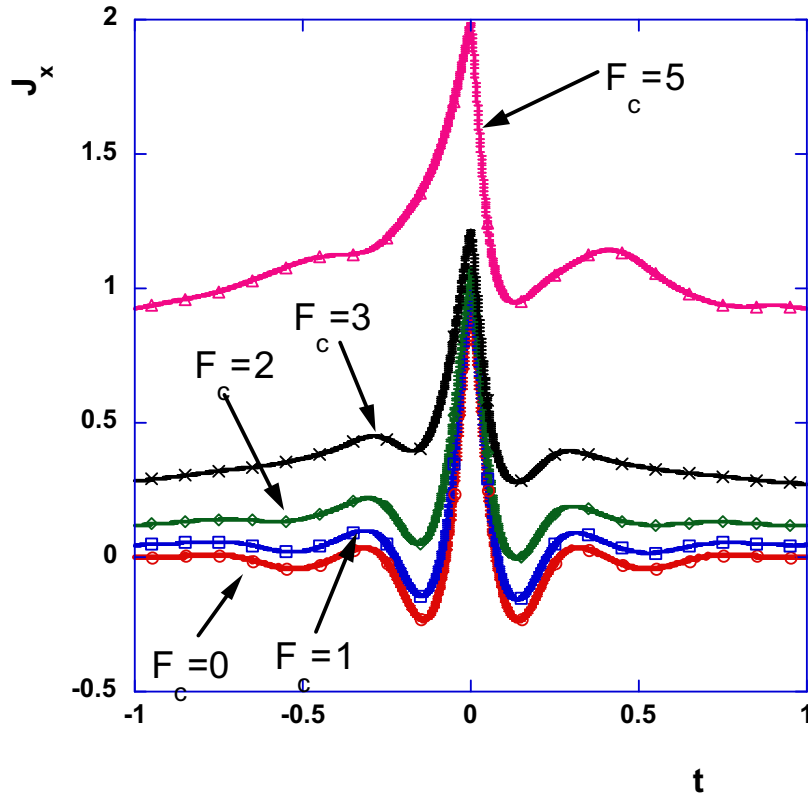


Figure 4-8 Average fluctuation path of colour flux J_x with $T_{hr} = \mu + 2.5\sigma$. These are averages of 10 runs with error bars given by the standard error in the mean (which are often so small that they are not distinguishable in the plot).

Average and most probable fluctuation paths exhibit roughly the same behaviour, with the average displaying a more regular field dependence than the most probable one.

Figure 4-9 shows the values of $\langle \delta_i \rangle$ of the average fluctuation path.

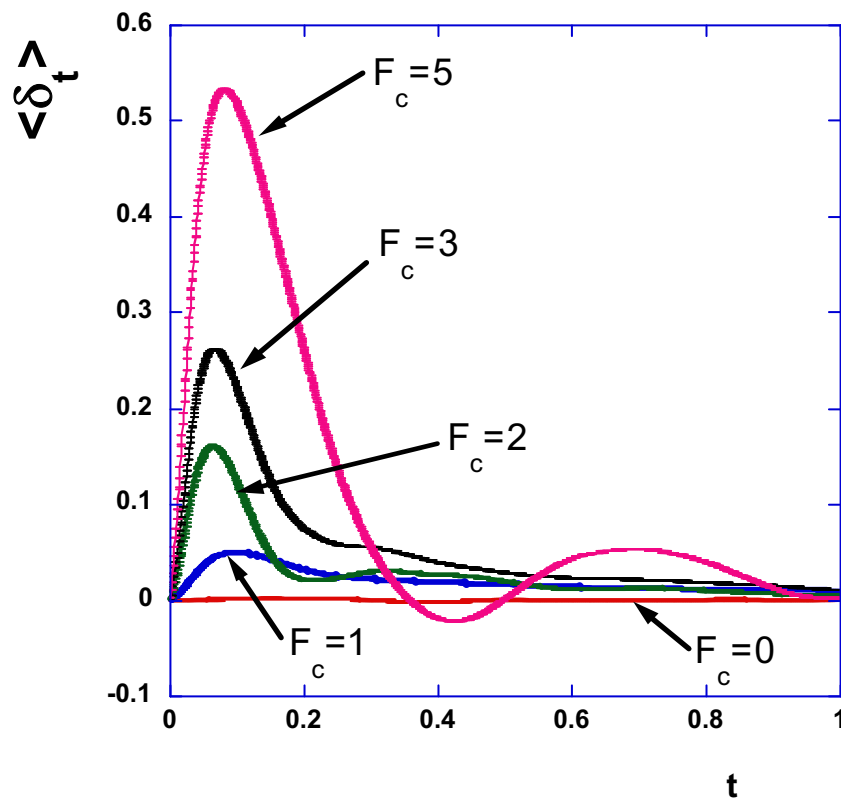


Figure 4-9 $\langle \delta_t \rangle$ of average fluctuation path of J_x with $T_{hr} = \mu + 2.5\sigma$. These are averages of 10 runs with error bars given by the standard error in the mean (which are often so small that they are not distinguishable in the plot).

Figure 4-10 shows the values of α_t of the most probable fluctuation paths and Figure 4-11 that of the average one. Again, the two are qualitatively similar. Importantly, even for colour diffusion, the $\langle \delta_t \rangle$ and α_t of the average and most likely fluctuation path of the flux J_x is zero to within numerical error at all times at equilibrium.

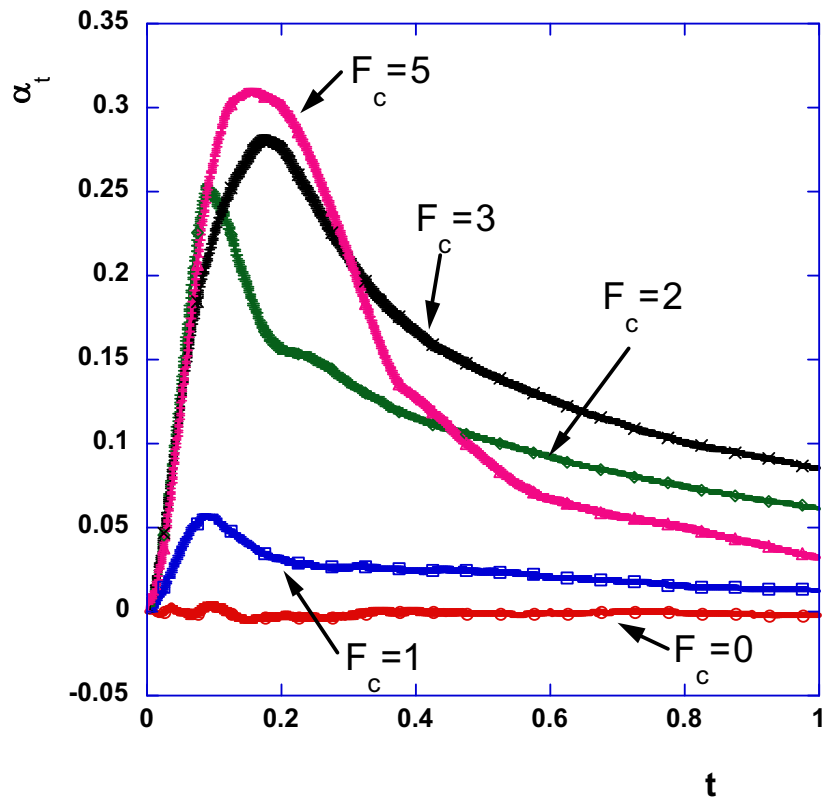


Figure 4-10 α_t of most probable fluctuation path of J_x with $T_{hr} = \mu + 2.5\sigma$.

These are averages of 10 runs with error bars given by the standard error in the mean.

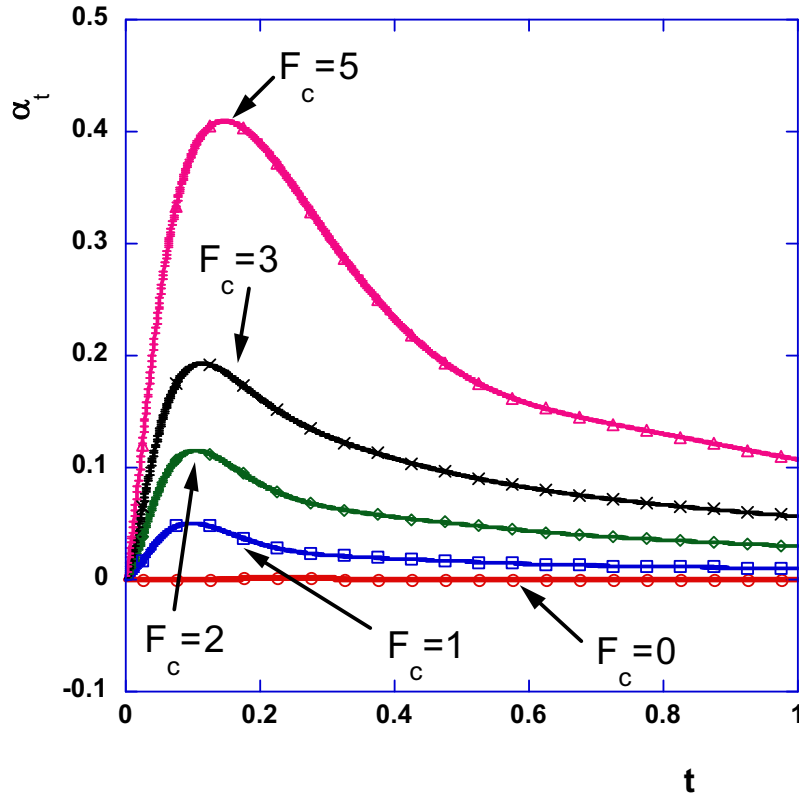


Figure 4-11 α_t of average fluctuation path of J_x with $T_{hr} = \mu + 2.5\sigma$. These are averages of 10 runs with error bars given by the standard error in the mean (which are often so small that they are not distinguishable in the plot).

Out of equilibrium asymmetry is evident: we can see that the $\langle \delta_i \rangle$ and α_t initially increase departing from 0; they reach a maximum and start decreasing. This behaviour can be explained in the same way as for shear flow. $\langle \delta_i \rangle$ and α_t are zero by definition at $t=0$; then they grow in correspondence to the asymmetry of the fluctuation path around its central point: this means that the approach to the peak is steeper than the departure from it. At a certain time they start to decrease, because the

correlations with the value at the peak have gone, and the fluctuation paths have relaxed to their asymptotic values.

Figure 4-12 presents the values of the autocorrelation of the colour flux

$C(J_x, t) = \langle J_x(\Gamma) J_x(S'\Gamma) \rangle$ for time t from 0 to 0.5. In a chaotic system correlations decay with time (cf. Figure 4-12) so that the value of a generic observable A_t for large t 's, are uncorrelated from the value at the threshold, and the “tails” of the FP are bound to return to $\langle A \rangle$. This implies that δ_t will become zero when correlations have decayed and its time average α_t must decay to zero as $1/t$ after this time.

As we did for shear stress, we select an arbitrary time $t = 0.05$ close to the peaks of the δ_t 's. Figure 4-13 shows δ_t , at $t = 0.05$, of the average fluctuation path of J_x , with $T_{hr} = 2.5\sigma + \mu$, as a function of the colour field in the linear regime. As for Couette flow, δ_t grows with the field.

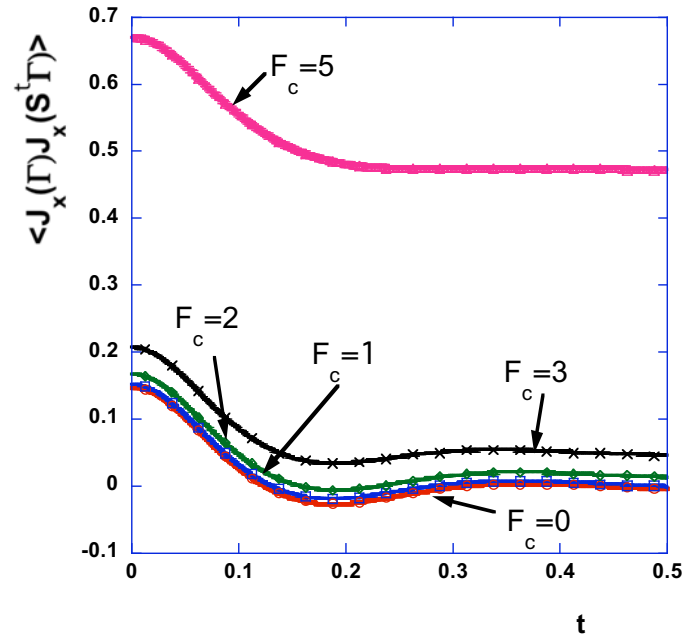


Figure 4-12 Autocorrelation function $C(J_x, t) = \langle J_x(\Gamma) J_x(S^t \Gamma) \rangle$ for colour flux J_x . These are averages of 10 runs with error bars given by the standard error in the mean (which are often so small that they are not distinguishable in the plot).

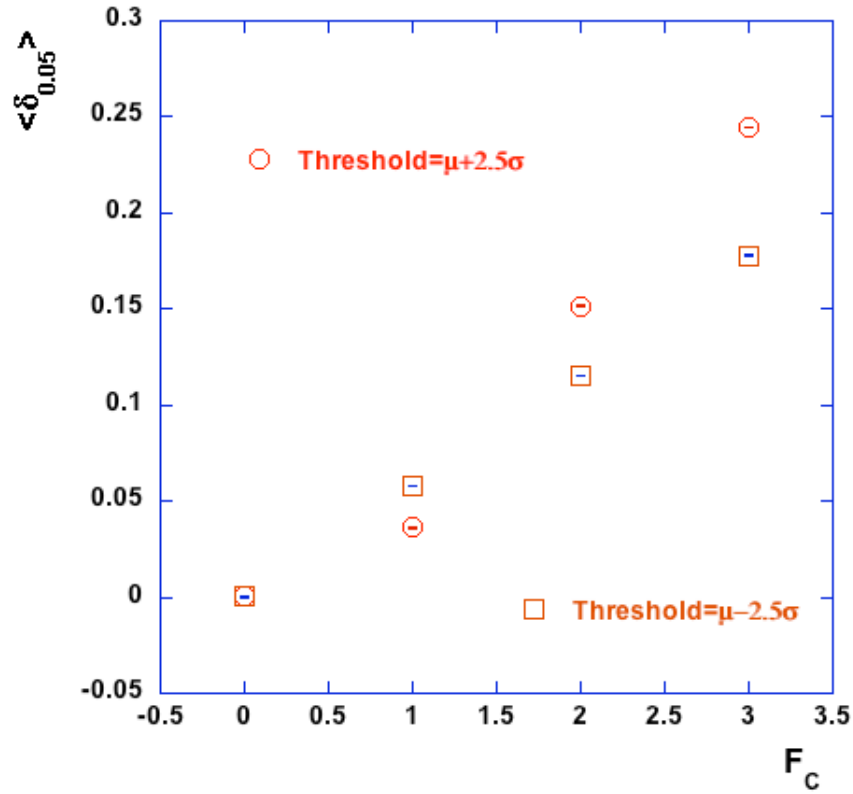


Figure 4-13 δ_t , with $t=0.05$ of average fluctuation path colour flux J_x with $T_{hr} = 2.5\sigma + \mu$ (red circles) and $T_{hr} = -2.5\sigma + \mu$ (orange squares) as a function of the colour field F_C , in the linear regime.

Trough fluctuation paths of J_x with threshold set to $\mu - 2.5\sigma$ have also been collected and histograms of the trough fluctuation paths of colour flux with $T_{hr} = \mu - 2.5\sigma$, are displayed with a “bird’s eye” view parallel to the frequency axis in Figure 4-14.

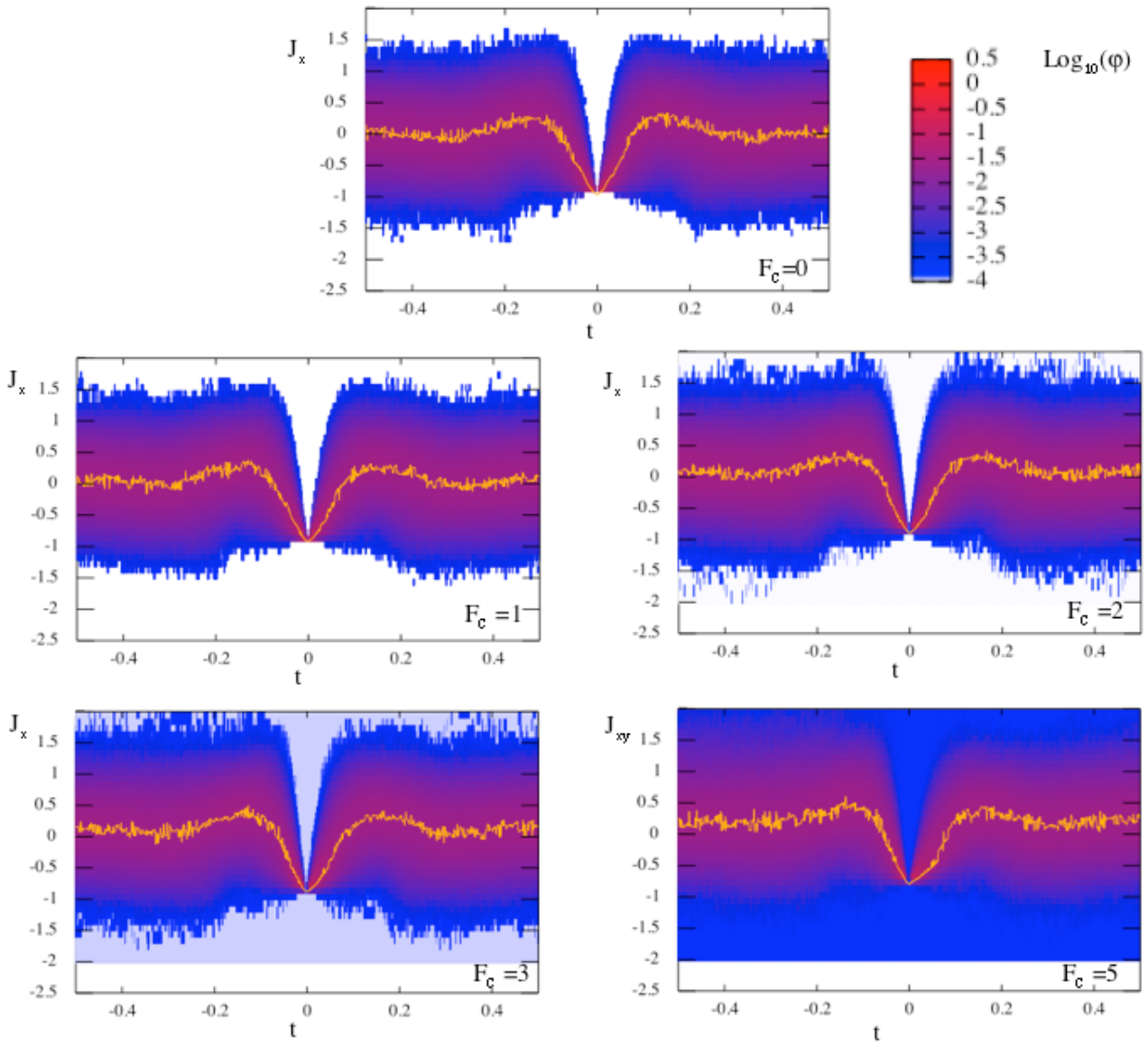


Figure 4-14 Histograms of colour flux (J_x) trough fluctuation paths for $F_c = 0, 1, 2, 3, 5$ with threshold $T_{hr} = \mu - 2.5\sigma$, with a “bird’s eye” view parallel to the frequency axis. The colours in the legend refer to the values of $\log_{10}(\phi)$. The gold line is a line through the ridge of the histograms.

It is evident from Figure 4-14 how, even for trough fluctuation paths, asymmetry develops out of equilibrium.

Figure 4-15 shows the trough fluctuation path of J_x with threshold set to $\mu - 2.5\sigma$ for various fields. Figure 4-15A is the mean fluctuation path, while Figure 4-15B is the most probable one.

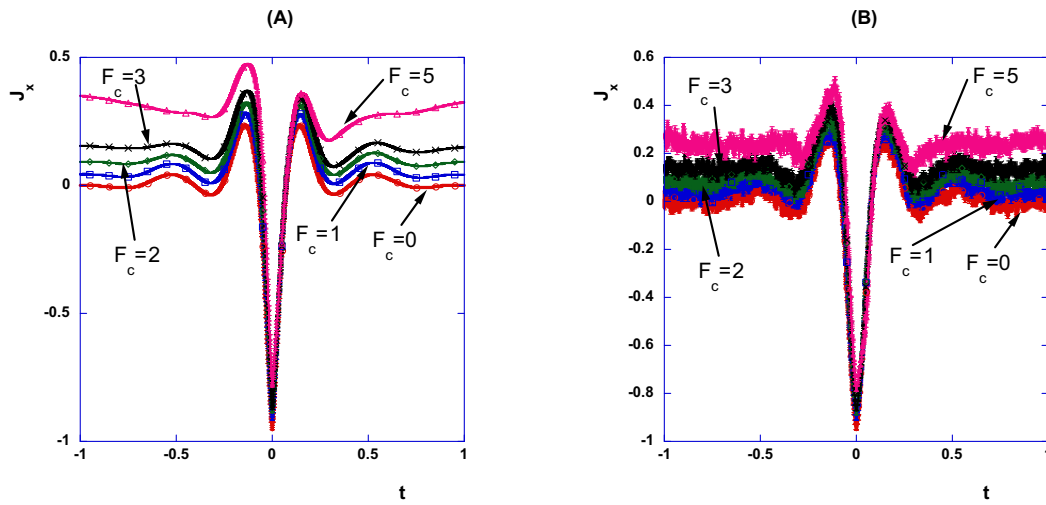


Figure 4-15 Average (A) and most probable (B) trough fluctuation path of colour flux J_x , with $T_{hr} = \mu - 2.5\sigma$. These are averages of 10 runs with error bars given by the standard error in the mean.

Such asymmetry of trough fluctuation paths of J_x is measured by the α_i 's displayed in Figure 4-16. Figure 4-16A shows the α_i 's of the average fluctuation paths, while Figure 4-16B that of the most likely ones.

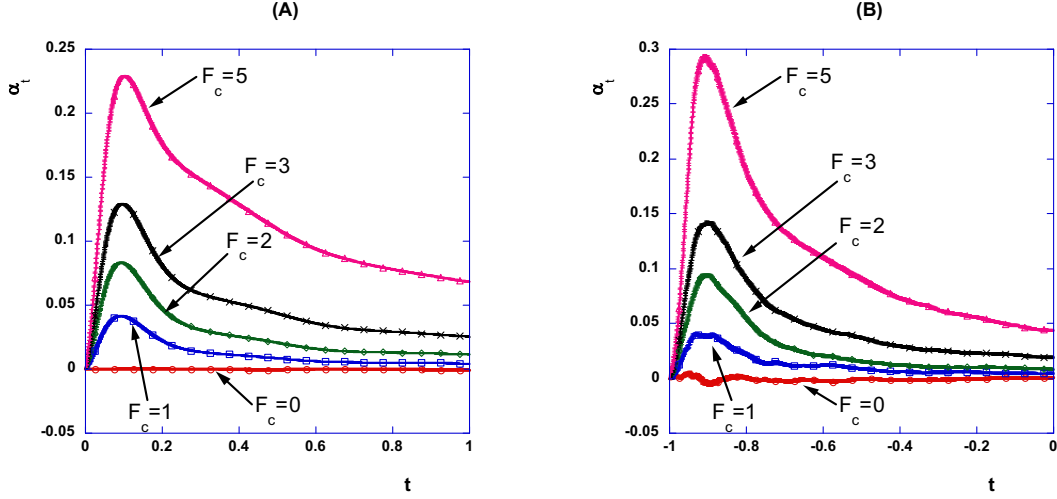


Figure 4-16 α_t of Average (A) and most probable (B) fluctuation path of colour field J_x with $T_{hr} = \mu - 2.5\sigma$. These are averages of 10 runs with error bars given by the standard error in the mean (which are often so small that they are not distinguishable in the plot).

As we can see, temporal asymmetry also emerges for trough fluctuation paths.

Yet the positive value of α_t for a negative fluctuation path (with negative threshold) indicates that—in opposition to what occurs for peak fluctuation paths—the deviation is less steep than the relaxation towards the mean. Asymmetry is also larger in the peaks.

Figure 4-13 shows $\langle \delta_t \rangle$ at $t = 0.05$ of the average trough fluctuation path of colour field J_x , with $T_{hr} = \mu - 2.5\sigma$, in function of F_c . As for the peak fluctuation paths (with $T_{hr} = \mu + 2.5\sigma$), in the linear regime the $\langle \delta_t \rangle$ at $t = 0.05$ increases with the field as discussed in Chapter 3.

4.2.2 Pressure fluctuation paths.

Analogue results to those obtained for J_x have been obtained for the pressure.

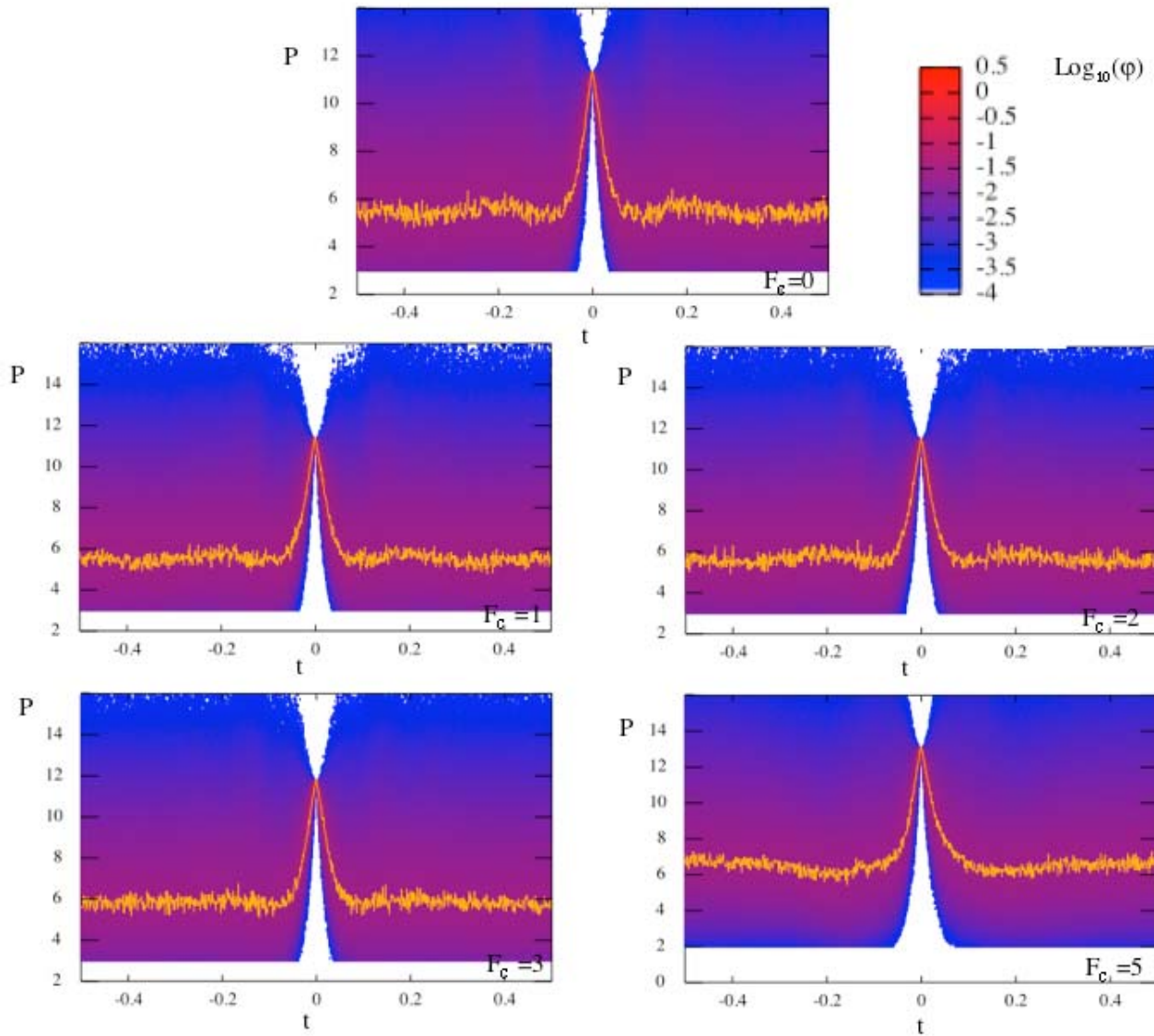


Figure 4-17 Histograms of pressure P peak fluctuation paths for $\gamma=0, 1, 2, 3, 4$ with a “bird eye” view parallel to the frequency axis. The colours in the legend refer to the values of $\log_{10}(\varphi)$. The gold line is a line through the ridge of the histograms.

We display the histograms of pressure trough fluctuation paths for F_c ranging from 0 to 5 in Figure 4-17, with a “bird’s eye” view parallel to the frequency axis.

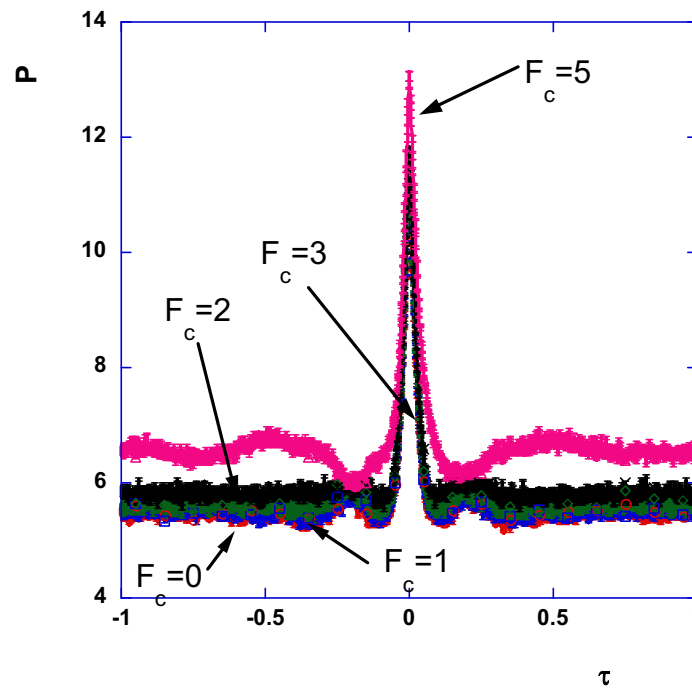


Figure 4-18 Maximum frequency value peak fluctuation path of pressure P , with $T_{hr} = \mu + 2.5\sigma$. These are averages of 10 runs with error bars given by the standard error in the mean.

In this case, asymmetry is more difficult to see. Figure 4-18 shows the maximum frequency value peaks for P with $T_{hr} = \mu + 2.5\sigma$ - and Figure 4-19 shows the corresponding α_i 's.

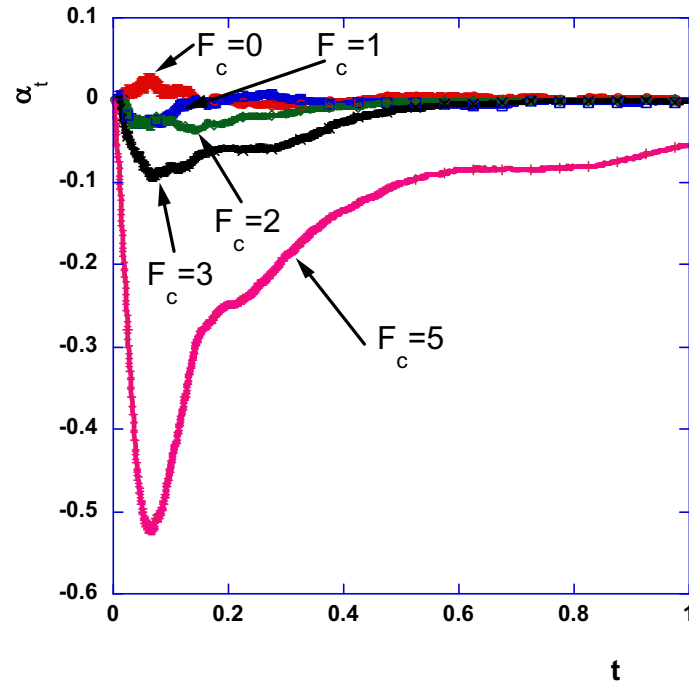


Figure 4-19 α_t of Most probable fluctuation path of pressure P with $T_{hr} = \mu + 2.5\sigma$ as averages of 10 runs with error bars. These are averages of 10 runs with error bars given by the standard error in the mean (which are often so small that they are not distinguishable in the plot).

Asymmetry out of equilibrium also develops for the average value of pressure, as we can see from In Figure 4-20, which shows the average peaks for pressure with $T_{hr} = \mu + 2.5\sigma$, and from Figure 4-21, that shows the corresponding α_t 's.

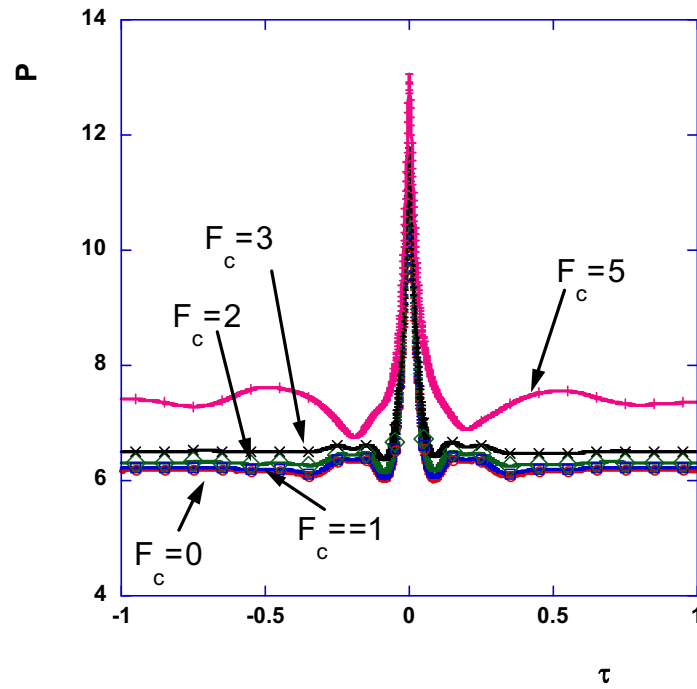


Figure 4-20 Average fluctuation path of pressure P , with $T_{hr} = \mu + 2.5\sigma$. These are averages of 10 runs with error bars given by the standard error in the mean (which are often so small that they are not distinguishable in the plot).

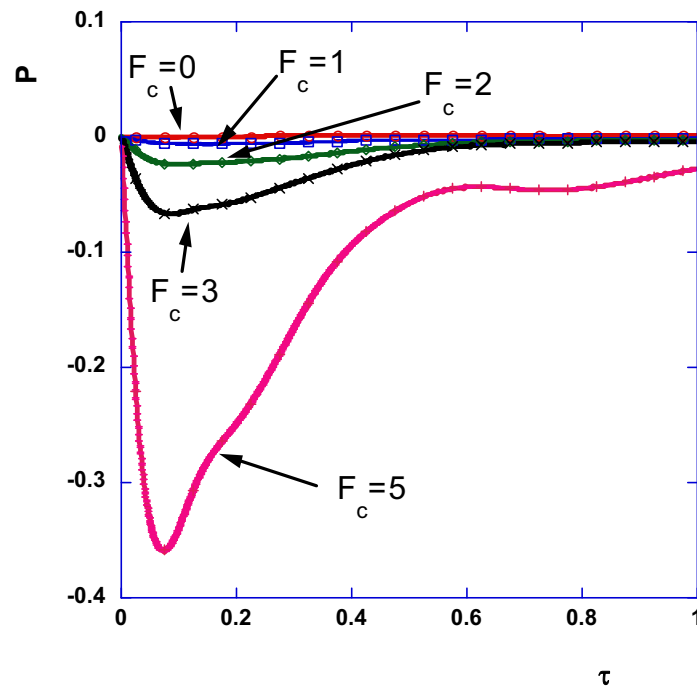


Figure 4-21 α_t of average fluctuation path of pressure P with $T_{hr} = \mu + 2.5\sigma$

These are averages of 10 runs with error bars given by the standard error in the mean (which are often so small that they are not distinguishable in the plot).

Although the asymmetry was more difficult to see on the histograms, it is clearly evident in these measures and it shows a similar behaviour to that seen in J_x (except in sign). The fact α_t is negative shows that the approach to the peak is steeper than the relaxation from it for pressure in colour diffusion.

Once more it is interesting to study the dependence from the field F_C of the asymmetry coefficient $\langle \delta_t \rangle$ at $t = 0.05$ (an arbitrary time close to the maximum) for the average peak fluctuation path of pressure, with $T_{hr} = \mu + 2.5\sigma$. In the linear regime, as we can see for Figure 4-22, the δ_t at $t = 0.05$ shows an almost quadratic dependence in function of the field, as seen for pressure in Chapter 3.

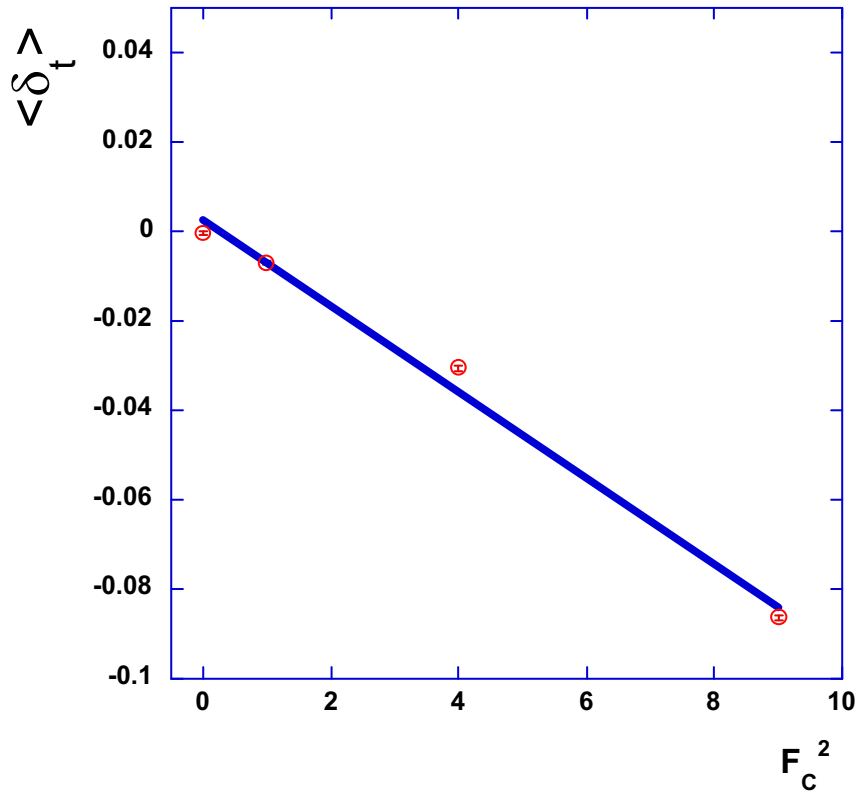


Figure 4-22 $\langle \delta_t \rangle$, with $t=0.05$ of average fluctuation path of pressure P with $T_{hr} = 2.5\sigma + \mu$ as a function of the square of the colour field F_C in the linear regime. The line is a linear fit through the data showing linear dependence of $\langle \delta_t \rangle$ on F_C^2 .

4.3 Conclusions

The simulations performed on a Weeks-Chandler-Andersen fluid undergoing colour field have shown that temporal asymmetry in fluctuation paths is not confined to the experimental framework of Couette flow. In principle, the non-autonomous equations of motion, coupled to the periodic boundary effects, could have induced spurious asymmetric effects in the system.

Temporally asymmetric fluctuations occur in the Weeks-Chandler-Andersen fluid under colour field, differently from what was observed for the Lorentz gas [81], although we should note that in low fields the asymmetry is small. The temporal symmetry observed in the Lorentz gas might be an effect of this simplified model.

The observation of temporal asymmetry in the shear flow and colour diffusion simulations of this thesis is consistent with the work of Giberti et al [82], on quite a different system. They considered fluctuation paths of the local heat flux in the nonequilibrium Fermi-Pasta-Ulam-beta model, a one dimensional model in which heat flow occurs due to a temperature gradient. As in our work, the equations of motion used in [82] are deterministic and reversible, and the system is driven to a nonequilibrium steady state. In [82] the fluctuation paths are defined in a similar manner to our 1st and 2nd definition, but the end of the paths occur when the heat flux is equal to its mean value. The average asymmetry coefficient that is measured is equal to our α_t divided by the difference between the threshold and the mean value. Giberti et al. [82] observe asymmetry, and also find that it is only weakly dependent on the parameters used in the simulation, including the number of oscillators.

Once temporal asymmetry is ascertained to be a general feature of deterministic and reversible microscopic systems, it is necessary to give a theoretical justification to its presence. This is the topic of the next chapter.

Chapter Five: FLUCTUATION PATHS, CORRELATION FUNCTIONS AND NONLINEAR RESPONSE THEORY.

In Chapter 3 and Chapter 4, we verified, for two reversible and deterministic nonequilibrium simulated systems, that deterministic and reversible systems exhibit temporal asymmetries in their fluctuation paths. We therefore confirmed that the asymmetry, postulated by [50,51,69] is not an artifact of stochastic models representation. In those chapters we limited ourselves to an observation of this behaviour, but we gave no justification of it.

In this chapter we justify the presence of asymmetry in fluctuation paths expressing them as cross correlation functions. Once Fluctuation Paths are expressed as cross correlation functions, the presence of asymmetries in fluctuations can be explained in terms of correlation function properties and using a Transient Time Correlation formalism.

To test our predictions we required a non-autonomous system to be considered. However the system studied in Chapter 4 was found to be unsuitable, due to some subtle formal requirements, in the study of small systems using the nonlinear response theory. These are discussed in the appendix to this chapter.

5.1 Building of the fluctuation paths as cross correlation functions of symmetric properties.

Referring to Chapter 2, Section 2.4.3, the third definition of fluctuation path is amenable to representation as a cross correlation function: we now proceed in

showing how.

Let $X(\Gamma)$ be the phase variable (of phase point Γ) whose asymmetry is being investigated; let s^z be the propagator that represents the evolution in time z of our thermodynamic system. The fluctuation path of $X(\Gamma)$ can be expressed as the cross correlation of the following functions $A(\Gamma)$ and $B(\Gamma)$:

$$A(\Gamma) = X(\Gamma) \quad (5.1.1)$$

$$B(\Gamma) = \begin{cases} 0 & \text{if } |X(\Gamma)| < T_{hr} \quad \text{or} \quad \text{sign}(\Delta X(\Gamma, \Delta t)) \neq \text{sign}(\Delta X(\Gamma, -\Delta t)) \\ \text{sign}(X(\Gamma)) & \text{if } |X(\Gamma)| > T_{hr} \quad \text{and} \quad \text{sign}(\Delta X(\Gamma, \Delta t)) = \text{sign}(\Delta X(\Gamma, -\Delta t)) \end{cases} \quad (5.1.2)$$

where: $\Delta X(\Gamma, t) = X(S^t \Gamma) - X(\Gamma)$ and Δt is a fixed time interval. $B(\Gamma)$ serves the purpose of selecting only values about stationary points above the threshold and turns troughs into peaks. An equivalent way of writing this is:

$$B(\Gamma) = \text{sign}(X(\Gamma)) \Theta(|X(\Gamma)| - T_{hr}) [\text{sign}(\Delta X(\Gamma, \Delta t)) + \text{sign}(\Delta X(\Gamma, -\Delta t))] / 2 \quad (5.1.3)$$

where $\Theta(r)$ is the Heaviside step function ($\Theta(r) = 1$ if $r > 0$, and $\Theta(r) = 0$ otherwise).

In the limit $\Delta t \rightarrow 0$, $B(\Gamma)$ is therefore simply equal to +1 for stationary points above the threshold T_{hr} ; it is equal to -1 for stationary points below the threshold T_{hr} ; and it is equal to 0 otherwise.

We can therefore write Y_t as:

$$Y_t = X(S^t \Gamma) B(\Gamma) \quad (5.1.4)$$

with $t \in [-\tau, +\tau]$, and this describes a fluctuation path if $B(\Gamma) \neq 0$.

If we take the (conditional) ensemble average over all Γ for which $B(\Gamma) \neq 0$, we obtain an average fluctuation path:

$$\begin{aligned} \langle Y_t \rangle_c &= \frac{\langle A(S^t \Gamma) B(\Gamma) \rangle}{\langle |B(\Gamma)| \rangle} = \langle A(S^t \Gamma) B(\Gamma) \rangle_c = \\ &= \langle X(S^t \Gamma) B(\Gamma) \rangle_c = \langle |X(S^t \Gamma)| \rangle_c \end{aligned} \quad (5.1.5)$$

where $\langle \dots \rangle_c$ denotes a conditional average (ie an average over fluctuation paths, whereas $\langle \dots \rangle$ represents an average over all Γ). Remembering the coefficient of asymmetry δ_t in Chapter 2 $\delta_t = Y_t - Y_{-t}$, we can write:

$$\langle \delta_t \rangle_c = \langle X(S^{-t} \Gamma) B(\Gamma) \rangle_c - \langle X(S^{+t} \Gamma) B(\Gamma) \rangle_c \quad (5.1.6)$$

We can easily observe that the correlation function $\langle Y_t \rangle$ is an even function if $X(\Gamma)$ is even or odd under time reversal mapping. In either cases $X(i\Gamma) = p_X X(\Gamma)$, where $p_X = \pm 1$ is defined as the parity of $X(\Gamma)$; then -of course- $A(i\Gamma) = p_X A(\Gamma)$, since $A(\Gamma) = X(\Gamma); \Theta(|X(\Gamma)| - T_{hr})$ and $|sign(\Delta X(\Gamma, \Delta t)) + sign(\Delta X(\Gamma, -\Delta t))|$ do not change with time reversal symmetry; on the other hand $sign(X(\Gamma))$ has the same parity of $X(\Gamma)$, and, therefore the parity of $A(S^t \Gamma) B(\Gamma)$ is

$$p_{AB} = p_A p_B = p_X p_X = (\pm 1)(\pm 1) = 1.$$

Due to the ergodic hypothesis, $\langle Y_t \rangle$ can be evaluated as a steady state time average:

$$\lim_{t \rightarrow +\infty} \frac{1}{t} \int_{z=0}^t A(S^{z+\tau}\Gamma) B(S^z\Gamma) dz \quad (5.1.7)$$

This means that we can evaluate it from a steady state simulation, following the time evolution of the values of X for a long enough interval.

We note that in the definition of Y_t , the value of $X(t_{STAT} - t)$ is multiplied by the sign of $X(t_{STAT})$ to ensure that fluctuation paths are always positive at the peak. This destroys the smoothness of Y_t as a function of F_c at $F_c = 0$ if the field changes the sign of $\langle X \rangle$ and therefore in analyzing the behaviour of the fluctuation paths as a function of F_c we consider the paths defined without this change in sign (i.e. $\text{sign}(X(t_{STAT})Y_t)$). We note that there is no explicit dependence of A or B on the field, however the nonequilibrium distribution function will change, and therefore the ensemble average may change.

We observe that if $\langle A \rangle_{F_c} = p_A^{F_c} \langle A \rangle_{-F_c}$, where $\langle \dots \rangle_{F_c}$ denotes the mean with respect to the nonequilibrium steady state driven by external field F_c and $p_A^{F_c}$ the parity with respect to the field, then $\langle \text{sign}(X(t_{STAT})Y_t) \rangle_{F_c} = p_A^{F_c} \langle \text{sign}(X(t_{STAT})Y_t) \rangle_{-F_c}$.

5.2 Properties of Correlation Functions.

With the average fluctuation path expressed as a correlation function, we can use properties of correlation functions to infer some properties of fluctuation paths. It is therefore important to study the properties and the asymmetry of various correlation

functions. Table 5-1 lists a number of properties of a generic correlation function

$$C(z, t) = \langle A(z+t)B(z) \rangle, \text{ where by } A(t) \text{ we mean } A(S^t).$$

Table 5-1 Properties of correlation functions $C(z, t) = \langle A(z+t)B(z) \rangle$, where $\langle \dots \rangle_{eq}$ is the average at equilibrium.

Ensemble/ Dynamics	Condition	$C(z, t)$	$C(z, t) - C(z, -t)$	$\lim_{t \rightarrow \infty} C(z, t)$	$\lim_{t \rightarrow \infty} (C(z, t) - C(z, -t))$
equilibrium	none	$\langle A(z)B(z+t) \rangle_{eq}$	0	0	0
equilibrium	$P_{AB} = -1$	0 when $t=0$	0	$\langle A \rangle_{eq} \langle B \rangle_{eq}$	0
steady state	$A=B$	$\langle A(z)A(z+t) \rangle$	0	$\langle A \rangle^2$	0
steady state	$A = \dot{B} \text{ or } B = \dot{A}$	$\langle A(z)B(z+t) \rangle_{eq}$	0	0	0
steady state	$P_C^{Fc} = 1$ linear regime		0	$\langle A \rangle \langle B \rangle$	0
steady state	none				0
transient response equilibrium at $t=0$	$P_A = -1$			0	0
transient response equilibrium at $t=0$	$P_{AB} = -1$	0 when $t=0$			0

These were obtained from observation in some cases, and by considering the symmetry of the functions on time-reversal and change of the sign of the field in others. We have assumed that correlations decay in all the systems considered. At equilibrium and in steady states, the value of $C(z, t)$ is independent of z , but not usually of t . Furthermore, at equilibrium the time-reversal invariance of the distribution function can be used to show that $C(z, 0) = 0$ if $p_{AB} = -1$ and

$$d(C(z, t))/dt \Big|_{z, t=0} = \dot{C}(z, t) \Big|_{z, t=0} = 0 \text{ if } p_{AB} = +1.$$

Using the information in Table 5-1, firstly we note that the identification of asymmetry through examination of $\langle A(z-t)B(z) \rangle - \langle A(z+t)B(z) \rangle$ should be carried out with caution, as, in the steady state, selection of some combinations of A and B will give a value of 0 for this difference. Another important deduction is that the selection of A and B given in equations (5.1.1) and (5.1.3) will result in $\langle \delta_t \rangle$ that becomes 0 in the linear regime if $p_X^{F_c} = 1$. In contrast, if $p_X^{F_c} = -1$, the asymmetry might be linear in F_c . We will see below that our results are consistent with a F_c^2 dependence of $\langle \delta_t \rangle$ on F_c for the pressure and with a F_c dependence for the color current, in accord with these results (and noted in the previous chapter –see Section 4.2). We also note that in the limit of long t , our measure of asymmetry will go to zero.

Another important observation can be made when considering steady states. We note that if there is any correlation between the functions A and B, then

$(C(z,0) - \langle A \rangle \langle B \rangle)$ will be non zero, while $(C(z,\infty) - \langle A \rangle \langle B \rangle) = 0$. If correlation between A and B exists and the correlation time is finite, in general $\dot{C}(z,t)\big|_{z,t=0} \neq 0$, although this will not be the case if $\dot{A}\big|_{z,t=0} = 0$ for all $B(z) \neq 0$ or if $A = B$, $\dot{A} = \dot{B}$, etc.

It is for example easy to prove this in the case of $A = B$. We can write:

$$\begin{aligned} \frac{d}{dt} \langle A(z) A(z+t) \rangle \bigg|_{t=0} &= \langle A(z) \dot{A}(z+t) \rangle \bigg|_{t=0} = \left\langle A(z) \frac{dA(z+t)}{d(z+t)} \right\rangle \\ &= \left\langle A(z) \frac{dA(z)}{dz} \right\rangle \end{aligned} \quad (5.1.8)$$

but in the steady state, $\frac{d}{dz} \langle A(z)^2 \rangle = \left\langle A(z) \frac{dA(z)}{dz} \right\rangle$ since phase averages must not vary with time.

Similarly, $\frac{d^2 C(z,t)}{dt^2} \bigg|_{z,t=0}, \frac{d^3 C(z,t)}{dt^3} \bigg|_{z,t=0} \dots$ will be non-zero in general. However, we

know that in the limit of large t, $C(z,t) = \langle A \rangle \langle B \rangle = C(z,-t)$. As demonstrated in

Figure 5-1, these features and any non-zero value of an odd time-derivative of $C(z,t)$

at $t = 0$ indicate that asymmetry must exist.

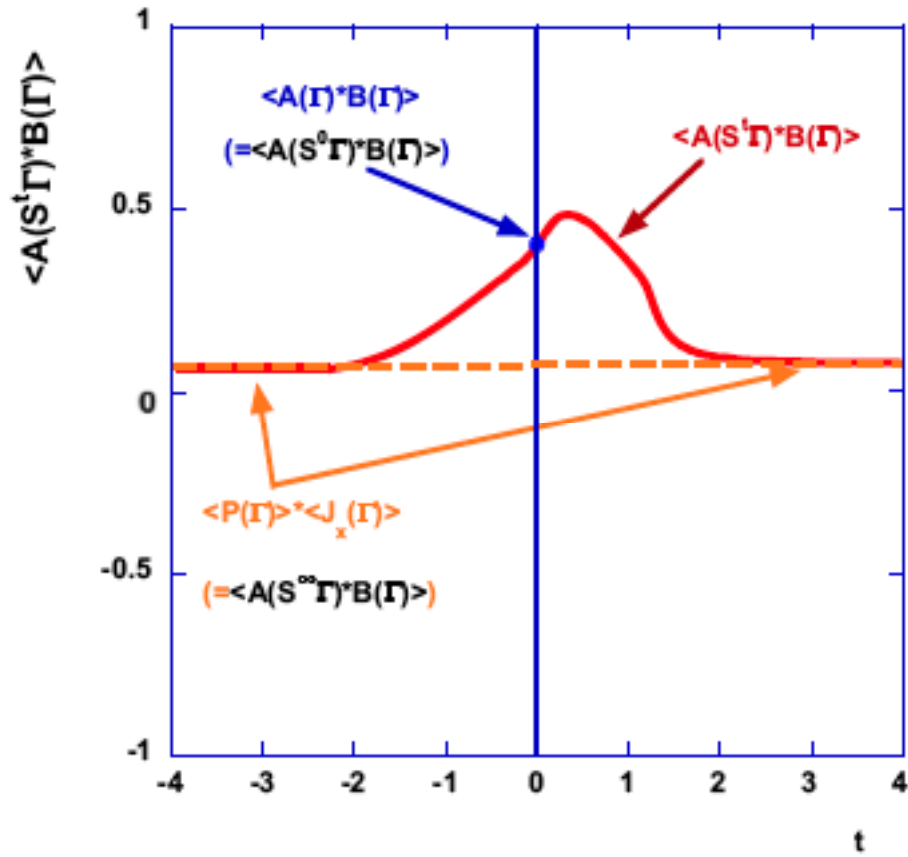


Figure 5-1 A schematic illustration of the existence of asymmetry in systems

where correlations decay and $\left. \frac{d^n C(z,t)}{dt^n} \right|_{z,t=0} \neq 0$, for any of $n = 1, 3, 5, \dots$

This is an important result as it means that it is not necessary to monitor the full

fluctuation path, it is sufficient to know $C(t,0)$, $\dot{C}(t,0)$, $\left. \frac{d^3 C(z,t)}{dt^3} \right|_{z,t=0}$ and

$\langle A \rangle \langle B \rangle$. This is computationally much more straightforward, and in most cases the

fact that $\dot{C}(z,t)|_{z,t=0}$ and $\left. \frac{d^3 C(z,t)}{dt^3} \right|_{z,t=0}$ are non-zero can be inferred from the facts

that A and B are correlated and the correlation time is finite. For example it would be expected that if A is the pressure (P) and B is the current (J_c) asymmetry would occur

as $\langle \dot{P}(z, t) J_C(z) \rangle \neq 0$ when $t = 0$. As mentioned above, if $\left. \frac{d^n C(z, t)}{dt^n} \right|_{z, t=0} = 0$ for all

$n = 1, 3, 5, \dots$, this is insufficient to rule out asymmetry as it might be due to the

definition of the fluctuation path, but if $\left. \frac{d^n C(z, t)}{dt^n} \right|_{z, t=0} \neq 0$, for any $n = 1, 3, 5, \dots$,

asymmetry is present.

For the correlation function developed to produce $\langle \delta_t \rangle$, (i.e. equations (5.1.1) and

(5.1.2)), it can be seen that $\left. \dot{A} \right|_{z, t=0} = 0$ for all $B(z) \neq 0$, since this is used as a selection

criteria in conditional average. Therefore $\left. \dot{C}(z, t) \right|_{z, t=0} = 0$ in this case, and the

argument based on the first derivative in the previous paragraph cannot be used to

predict asymmetry in the fluctuation paths. However, the third-derivative is not

subject to such a condition, and would be expected to be non-zero at $t = 0$. This

indicates that $\langle \delta_t \rangle \neq 0$ and asymmetry in the fluctuation paths exists.

5.3 Nonlinear response theory

Since we have expressed the asymmetry coefficient, $\langle \delta_t \rangle$, in terms of an ensemble

average of a phase function, we can also apply nonlinear response theory to its

analysis. The advantage of this approach, for the purposes of this work, is that it

allows a nonequilibrium, time-dependent phase function to be expressed in terms of

an ensemble average over equilibrium initial states. Using nonlinear response theory,

the transient time correlation function provides the time dependence of a phase

function in a nonequilibrium steady state far from equilibrium [101]. In the long time limit for a system that reaches a steady state, it can be considered as a generalization of the Green-Kubo relations [109] to states far from equilibrium as it provides an expression for the flux, from which the non-linear transport coefficients can be determined. It allows us to express the average value of a function $\langle A(S^z \Gamma) \rangle$ at time z after equilibrium in terms of its value at equilibrium $\langle A(\Gamma) \rangle_{eq}$ and an integral of a time correlation function, which in this case (see Appendix) is given by:

$$\langle A(S^z \Gamma) \rangle = \langle A(\Gamma) \rangle_{eq} - \beta V F_c \int_0^z \langle J(\Gamma) \Delta A(S^u \Gamma) \rangle_{eq} du \quad (5.1.9)$$

where $J(\Gamma)$ is the dissipative flux and $\Delta A(S^u \Gamma) = A(S^u \Gamma) - \langle A \rangle_{eq}$. The dynamics

S^u is generated using the nonequilibrium (thermostatted) equations of motion, but the ensemble averages use the equilibrium distribution. This can directly be extended to express the product of two functions $A(\Gamma)$ and $B(\Gamma)$ separated by a time interval t [88], and Equation (5.1.9) becomes:

$$\begin{aligned} \langle A(S^{z+t} \Gamma) B(S^z \Gamma) \rangle &= \\ &= \langle A(S^t \Gamma) B(\Gamma) \rangle_{eq} - \beta V F_c \int_0^z \langle J(\Gamma) \Delta A(S^{u+t} \Gamma) B(S^u \Gamma) \rangle_{eq} du \end{aligned} \quad (5.1.10)$$

Then [88]:

$$\begin{aligned} \langle A(S^{z-t} \Gamma) B(S^z \Gamma) \rangle - p_{AB} \langle A(S^{z+t} \Gamma) B(S^z \Gamma) \rangle &= \\ = p_{AB} \beta V F_c \int_{-z}^z \langle J(\Gamma) A(S^{u-t} \Gamma) B(S^u \Gamma) \rangle_{eq} du \end{aligned} \quad (5.1.11)$$

where for A,B given by equations (5.1.1) and (5.1.2), $p_{AB} = 1$, as discussed above.

This is a transient response expression. However, if the system reaches a steady state, it will become independent of z , and give the limiting steady state expression. This relation, for $t \in [-\tau, +\tau]$, assumes a particular significance if applied to the functions $A(\Gamma)$ and $B(\Gamma)$ of Equations (5.1.1) and (5.1.3), in that the left hand side of Equation (5.1.11) describes the measure of asymmetry $\langle \delta_t \rangle$. It is this steady state result that we are interested in:

$$\langle \delta_t \rangle = \lim_{z \rightarrow \infty} \frac{\langle A(S^{z-t}\Gamma) B(S^z\Gamma) \rangle - \langle A(S^{z+t}\Gamma) B(S^z\Gamma) \rangle}{\langle B(S^z\Gamma) \rangle} \quad (5.1.12)$$

We will verify this relationship in numerical simulations in the next Section.

Now that we have expressed the asymmetry coefficient in terms of equilibrium ensemble averages and the transient time correlation function, we consider its properties again. We note from above, that the expression (5.1.11) with $p_{AB} = 1$ applies to all phase variables A, irrespective of their parity under time reversal. First of all we observe that (5.1.11) shows that at equilibrium ($F_c = 0$), the asymmetry coefficient is zero. While this is not a new observation, given (5.1.11), it is perhaps the most trivial proof of this fact. Similar considerations to those in Section 5.2 show that the asymmetry varies as F_c to leading order when $p_A^{F_c} = -1$ and as F_c^2 when $p_A^{F_c} = 1$. In addition we trivially observe that if $p_{AB} = 1$, the left hand side of (5.1.11) is zero, but note that this is also evident from consideration of the right hand side of that equation. In that case, the argument of the time-integral is an odd function and the time integral is from $-z$ to z , which will produce a value of zero for all z . The

emergence of asymmetry can then be seen to come from the disturbance of integrand when $t \neq 0$ (i.e. a non-zero value of t results in a shift in the time at which values of A are determined compared to those at which the values of B are determined) will clearly, in general, result in the argument no longer being an odd function, and therefore the integral will no longer be zero. This will be true in general, but in the special case that z is large, by shifting the time origin and using the fact that correlations decay and $A = B$ or $\dot{A} = B$, etc, the integral can be reformulated giving the expected result of zero.

5.4 Numerical Results

The system investigated is the model of colour diffusion (See section 2.3). We use equations (5.1.13)-(5.1.14) where, since we thermostat $\frac{1}{2} \sum_{i=1}^N \frac{\mathbf{p}_i \cdot \mathbf{p}_i}{m_i}$, the isokinetic canonical distribution function with the usual value of β is not preserved employing the colour diffusion dynamics of Chapter 4. This is explained in more detail in the Appendix to this chapter (Section 5.6). Molecular dynamics simulations have been carried out in 2 Cartesian dimensions with a primitive cell containing 8 particles with kinetic temperature fixed at 1 and time step of 10^{-3} . We consider an equilibrium system as well as a range of nonequilibrium systems ($F_c = 0.5, 1, 1.5, 2, 3, 4$), extending from the linear regime to the nonlinear regime and examine the fluctuation paths of J_c . Sets of ten independent simulations of least 3×10^6 time steps were carried out for each value of color field, in order to determine the mean and the

standard deviations of J_c , so to set the thresholds. These means and standard deviations of J_c and pressure are reported in Table 5-2.

Table 5-2 Mean μ and standard deviation σ of color current J_c from 10 runs with corresponding standard errors (three times the standard deviation of the means out of the runs).

F_c	$\mu(J_c)$	$\sigma(J_c)$
0	0 ± 0.006	0.341 ± 0.005
0.5	0.021 ± 0.007	0.342 ± 0.004
1	0.043 ± 0.007	0.343 ± 0.005
1.5	0.069 ± 0.005	0.345 ± 0.003
2	0.101 ± 0.008	0.35 ± 0.003
3	0.196 ± 0.023	0.365 ± 0.006
4	0.341 ± 0.019	0.38 ± 0.007

From the data we can see that the linear regime extends to approximately $F_c = 1.5$. For large J_c , large fluctuations (several standard deviations from the mean) are biased above the mean in the nonequilibrium systems; the same does not happen for the values of J_c at equilibrium, since they are symmetrically distributed around their mean, which is zero. On the basis of these data, sets of 30 steady state simulations of 3.5×10^7 time steps were carried out for each strain rate. The average FP of J_c with a threshold equal to $\mu + 2.5\sigma$ was evaluated for $\tau = 1$ and are shown in Figure 5-2 A. Figure 5-2 B shows the values of $\langle \delta_t \rangle$ of the fluctuation paths. All values are plotted with error bars determined as the standard error of the mean. The average fluctuation paths are obtained as averages of these runs and so are the $\langle \delta_t \rangle$'s. These values are plotted with error bars.

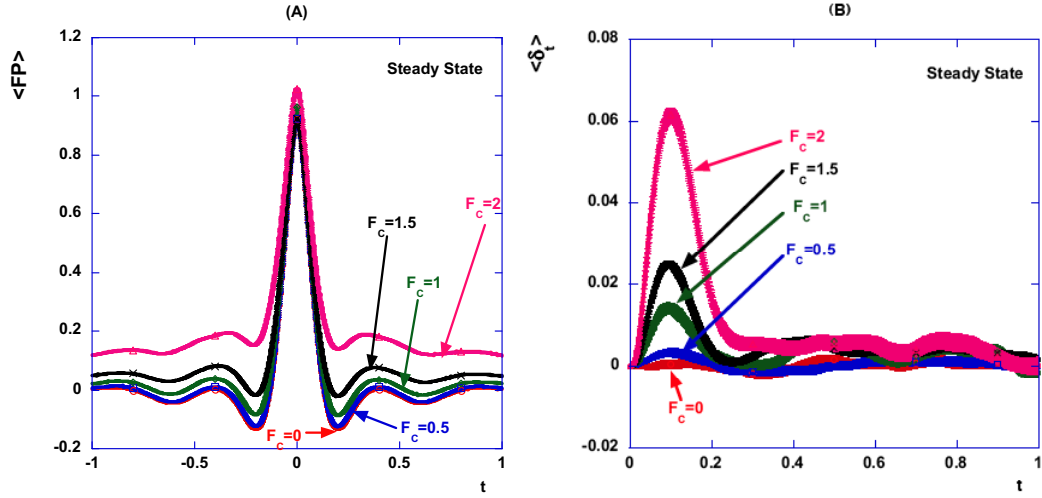


Figure 5-2 A: Average fluctuation path of the color current from 10 steady state runs with error bars (equal to the standard deviation of the means). B: $\langle \delta_t \rangle$ for the average fluctuation path of the color current from 10 runs with error bars (equal to the standard error of the mean).

Importantly, for $F_c = 0$, the value of $\langle \delta_t \rangle$ is zero to within numerical error at all times.

This is an independent check of the accuracy of our results. Furthermore, at all other

F_c , asymmetry is evident: we can see that the $\langle \delta_t \rangle$ initially increases departing from

0; it reaches a maximum $\langle \delta_t \rangle$ and starts decreasing. This behaviour was also

observed in our work in Chapter 3 and 5. From the definition of $\langle \delta_t \rangle$ it is obvious that

this quantity vanishes at $t = 0$; as t increases, $\langle \delta_t \rangle$ departs from zero indicating

asymmetry out of equilibrium, showing, in particular, that the approach to the peak of

the fluctuation path is less steep than the departure from it. At a certain time $\hat{t} > 0$,

$\langle \delta_t \rangle$ starts to decrease in connection to the decay of the correlations of the system, in

the same way as previously explained for a general odd function. All the previous

results confirm the observations we made for different definitions of fluctuation path

in Chapter 3 and 4, attesting once more the presence of asymmetry of fluctuations, even if defined in slightly different ways. The symmetries of various correlation functions were also considered. Sets of ten independent simulations of 5×10^5 time steps were carried out for ($F_c = 0.5, 1, 1.5, 2, 3, 4$) in order to compute examples of correlation functions $\langle B(S'\Gamma)A(\Gamma) \rangle$.

The presence of asymmetry in t is expected for a generic odd property, such as the correlation between the flux J_c and the pressure P , as discussed above. Figure 5-3 displays the cross correlation $\langle J_c(S'\Gamma)P(\Gamma) \rangle$ as a function of t for our system undergoing color diffusion with $F_c = 2$. The results are obtained as time averages from steady state runs and are the average values obtained from 10 runs of 10^8 time steps with error bars. We verify that for this function the time dependence of the correlation function fulfills the relevant properties of Table 5-1. At equilibrium,

$\langle J_c(\Gamma)P(\Gamma) \rangle = 0$ whereas it has a finite positive value when $F_c \neq 0$. We observe that for all fields, in the limits $t \rightarrow +\infty$ and $t \rightarrow -\infty$ the correlation functions are equal, and equal to $\langle J_c \rangle \langle P \rangle$, as expected for this chaotic dynamics where correlations decay.

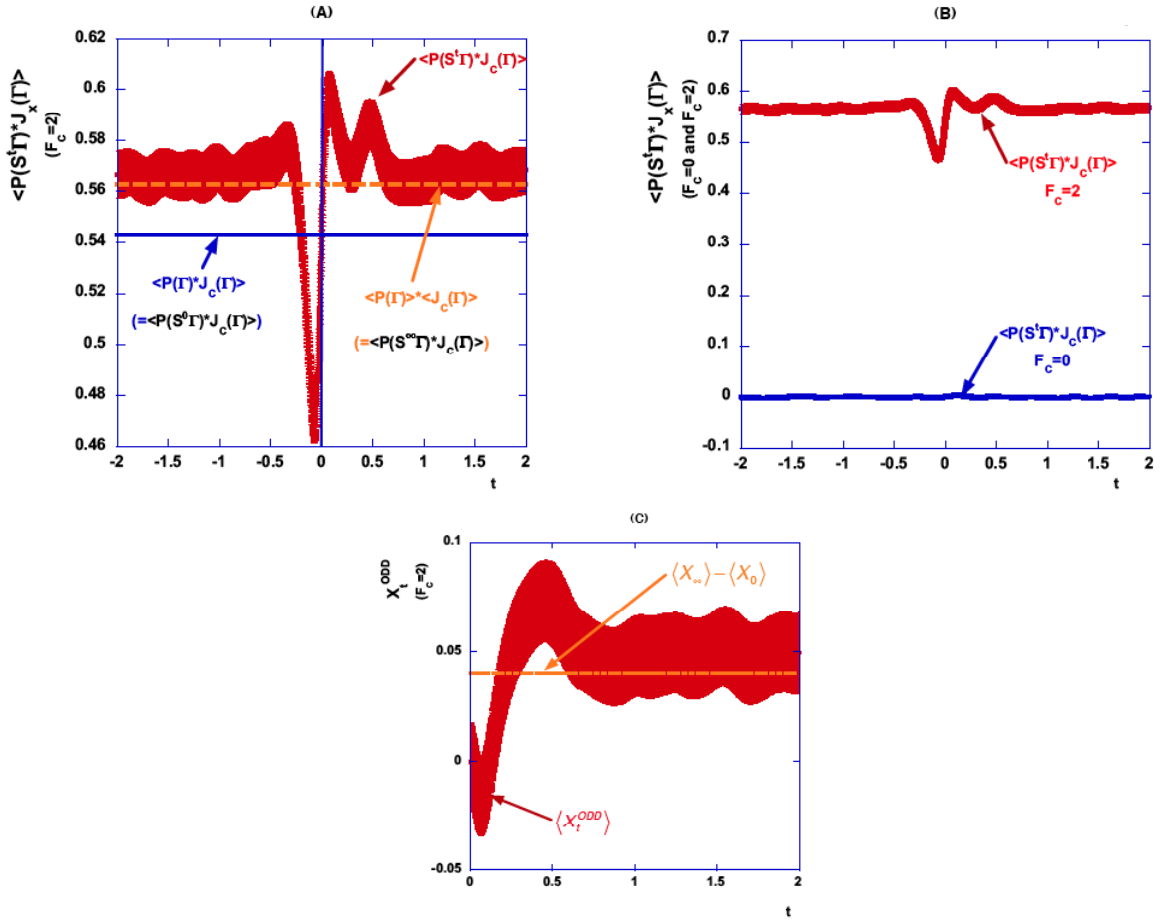


Figure 5-3 Cross correlation function of color current J_c and pressure P obtained from an average of 10 runs with error bars (equal to the standard error of the mean) with color field $F_c=2$. **B:** Comparison between the profile of the cross correlation with $F_c=2$ and with $F_c=0$, that is at equilibrium, where the profile is constantly equal to zero. **C:** Coefficient of asymmetry X_t^{ODD} , for $F_c=2$, that shows asymmetry out of equilibrium.

We also note that at $t = 0$ the slope is different from zero, and that the value at $t = 0$ is different from that at large values of $\pm t$. This is consistent with the analysis at the end of Section 5.2.

In the nonequilibrium system, at $t=0$ the correlation has a value $\langle J_c(\Gamma) P(\Gamma) \rangle$ and a slope different from zero; it then relax in both directions to equal values

$\langle J_c(S'\Gamma)P(\Gamma) \rangle \neq \langle J_c(\Gamma) \rangle \langle P(\Gamma) \rangle \neq 0$ for long $|t|$: therefore for intermediate $|t|$, our cross correlation $\langle J_c(S'\Gamma)P(\Gamma) \rangle$ must be different from $\langle J_c(S^{-t}\Gamma)P(\Gamma) \rangle$. For even functions, the presence of asymmetry can be measured by calculating

$$X_t(A, B) = C(z, t) - C(z, -t).$$

For odd functions, due to the characteristics of their profile described above, in particular for its non negative slope at $t = 0$, we consider the departure of the profile from an anti-symmetric one by evaluating $X_t^{ODD}(A, B)$, where

$$X_t^{ODD}(A, B) = 2C(z, 0) + C(z, t) + C(z, -t),$$

so that our coefficient starts from 0 for $t=0$. We can see from Figure 5-3 C how this coefficient indicates the presence of a departure from an anti-symmetric behaviour, which is, as discussed, the general case out of equilibrium. There are choices of particular functions, such as the correlation of a function with itself or with its derivative, for which it can be proven and shown by numerical results, that no asymmetry is present. Figure 5-4 shows the colour current autocorrelation $\langle J_c(S'\Gamma)J_c(\Gamma) \rangle$ with $F_c = 2$.

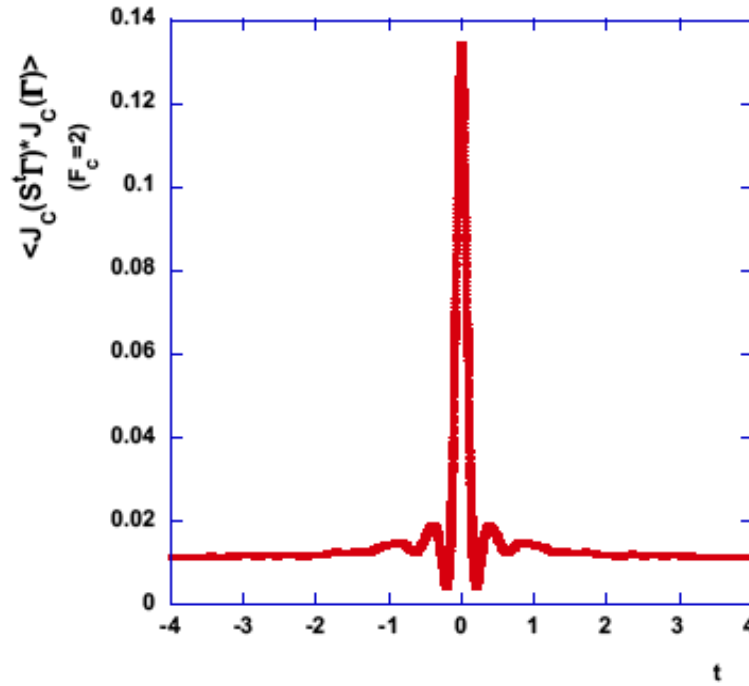


Figure 5-4 Autocorrelation function of color current J_c average of 10 runs with error bars (equal to the standard error of the mean) with color field F_c .

Its profile is perfectly symmetric, within numerical error, as we can see from Figure 5-5, that plots $X_t(A, B)$ for $A = B = J$ together with $X_t(A, B)$ for $A = \dot{J}$ and $B = J$, which are zero for every t . This behaviour is different from that of the cross correlation $\langle J_c(S^t\Gamma)P(\Gamma) \rangle$. The numerical results for $\langle \delta_i \rangle$ in Figure 5-5 and Figure 5-6 confirm this.

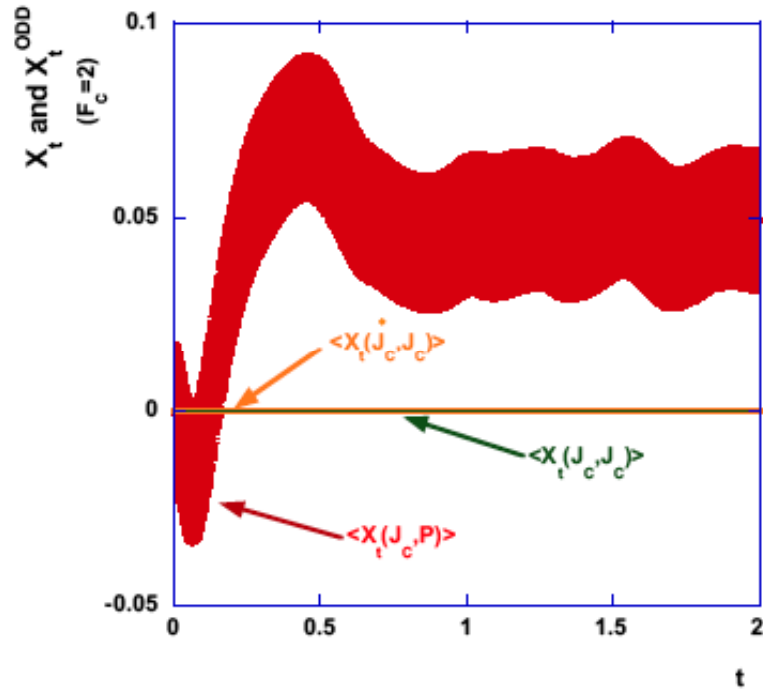


Figure 5-5 Values of $X(z, t)$, which measures the departure of the cross correlation function $C_{J_c, J_c}(z+t) = \langle J_c(z) J_c(z+t) \rangle$ from symmetric behaviour, and values of X_t^{ODD} which measures the departures from anti-symmetric behaviour of $C_{J_c, J_c}(z+t) = \langle J_c(z) \dot{J}_c(z+t) \rangle$ and $C_{J_c, P}(z+t) = \langle J_c(z) P(z+t) \rangle$. All data are computed as average of 10 runs with error bars (equal to the standard error of the mean) with color field $F_c = 2$.

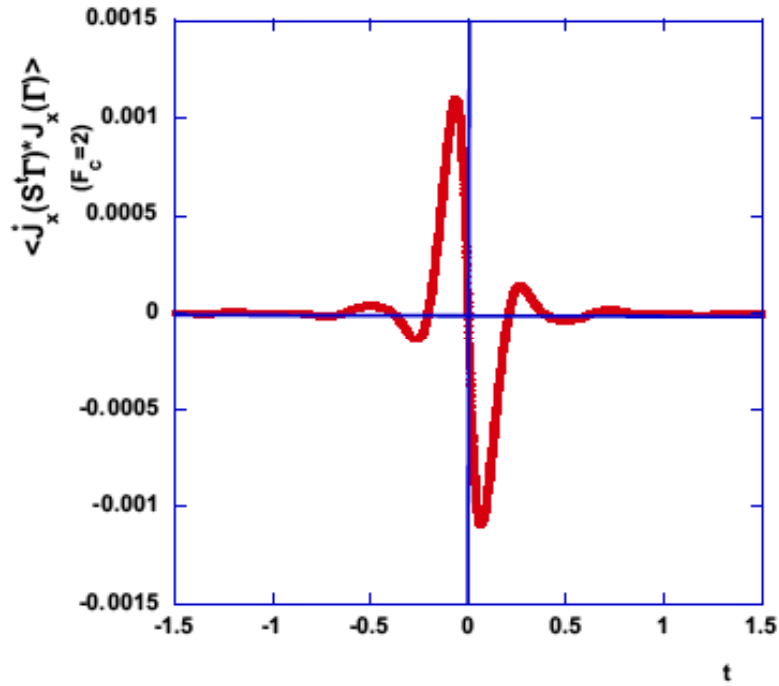


Figure 5-6 Correlation function of color current J_c with its derivative as average of 10 runs with error bars (equal to the standard error of the mean) with color field $F_c=2$.

We now provide numerical results confirming the transient time correlation function expression for the asymmetry (5.1.11), and thus confirming the relationship on which we based our main argument in Section 5.3 that asymmetry must exist in general for correlations functions, and for the fluctuation paths in particular. Referring to Equation (5.1.11), we see that if we make z sufficiently large that a steady state is reached, the right hand side of our equations give $\langle \delta_i \rangle$ through Equation (5.1.12). We therefore ran a set of 20 simulations consisting each of 10^6 transients starting from equilibrium values and going forward and backwards in time for a period $z + t$, with $t \in [-\tau, +\tau]$, $\tau = 1$ and with $z = 3$ so as to be far enough from the equilibrium starting point to consider our system well into the steady state. In practice it was not possible

to run the transients backwards in time more than a period of about of 1 due to numerical error. Therefore we ran them backwards for t (with $t=1$); and we then exploited the time reversal properties of the system in order to calculate the values assumed by our function from $-t$ to $-(t+z)=-4$ directly from the values obtained in the forward run.

We then evaluated the left hand side of equation (5.1.11). The numerical error in evaluation of the left hand side of Equation (5.1.11) from the transients is extremely high: in fact, the probability of finding a peak exactly at time z of the transient is very low (at high fields it is much lower than in the corresponding steady state because much of the trajectory is in a state close to the initial equilibrium state where large deviations are even more unlikely to be observed). An enormous number of cycles should be run in order to obtain data with reasonable statistics, and while the data we were able to obtain was in agreement with the results, the statistical error was so large that the values were not very meaningful: therefore these results are not shown.

Instead, the left hand side of the equation was evaluated from the steady state simulations. Figure 5-7 shows the right hand side of Equation (5.1.11), scaled to give $\langle \delta_t \rangle$ through Equation (5.1.12), and evaluated from the transient runs is equal to that evaluated as steady state average, to within numerical errors. This confirms the link between the presence of asymmetry with transient time correlation function theory, for the fluctuation paths of a deterministic and reversible system.

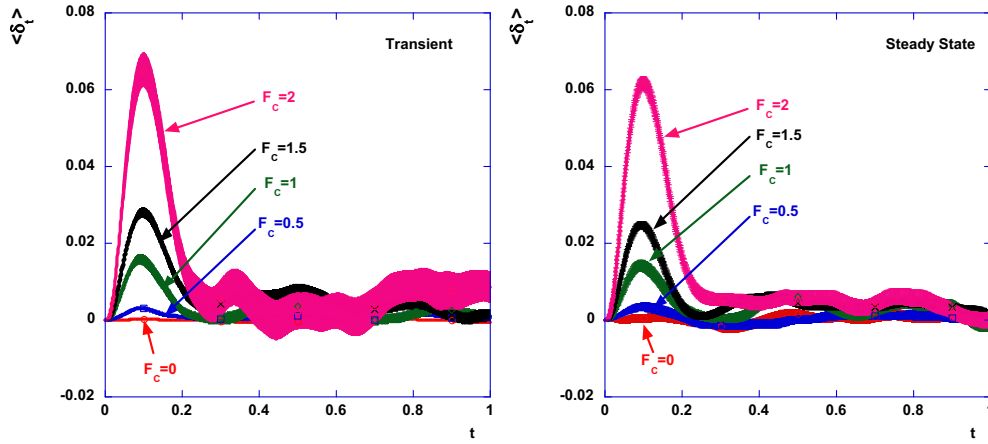


Figure 5-7 The values of $\langle \delta_i \rangle$ of the average fluctuation path of color current as averages of 10 transient runs with error bars (equal to the standard error of the mean), calculated using the right hand side of equation (5.1.11) with $z=3$, and compared to the value obtained using a steady state expression.

Finally we consider the dependence of $\langle \delta_i \rangle$ as a function of the field F_c . We select an arbitrary time $t = 0.1$ close to the peaks of the $\langle \delta_i \rangle$. Figure 5-8 shows $\langle \delta_i \rangle$ at $t = 0.1$, of the average fluctuation path of color flux J_c , with $T_{hr} = \mu + 2.5\sigma$, as a function of the color field F_c applied. We see that $\langle \delta_i \rangle$ grows with the field in the linear regime: once more there are two contributions to the growth of $\langle \delta_i \rangle$. Firstly there is a direct contribution which we would expect to be linear for the odd property J_c , if the value of the threshold was fixed; then there is a growth due to an increase in the threshold, since μ increases linearly with F_c .

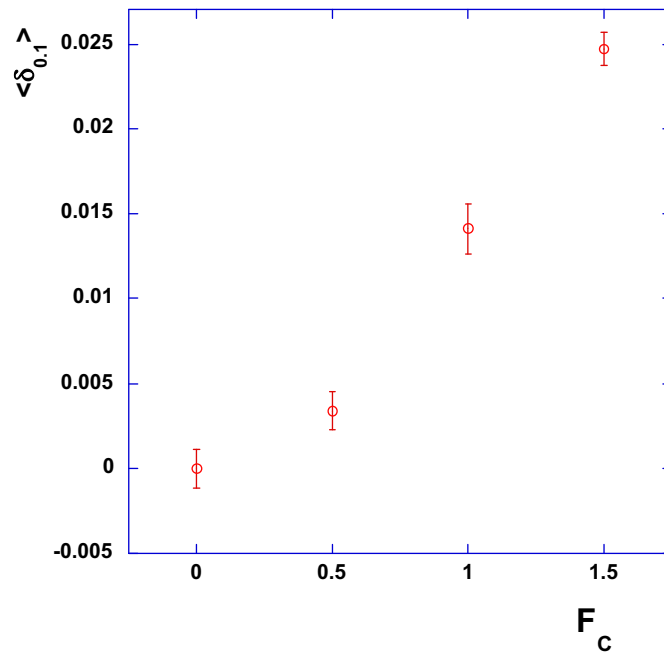


Figure 5-8 $\langle \delta_t \rangle$ as a function of the field F_c at arbitrary time $t = 0.1$ close to the peaks of the $\langle \delta_t \rangle$, with $T_{hr} = \mu + 2.5\sigma$. Error bars are equal to the standard error out of the 10 runs.

We also are interested in seeing if asymmetry persists in the large N limit, and have carried out preliminary calculations for various N with $T_{hr} = \mu + 2.5\sigma$. The results are shown in Figure 5-9. There is a decrease in the asymmetry with N , however the statistical errors (error bars shown are one standard error) are so large that it is not possible to determine the functional form of the N dependence.

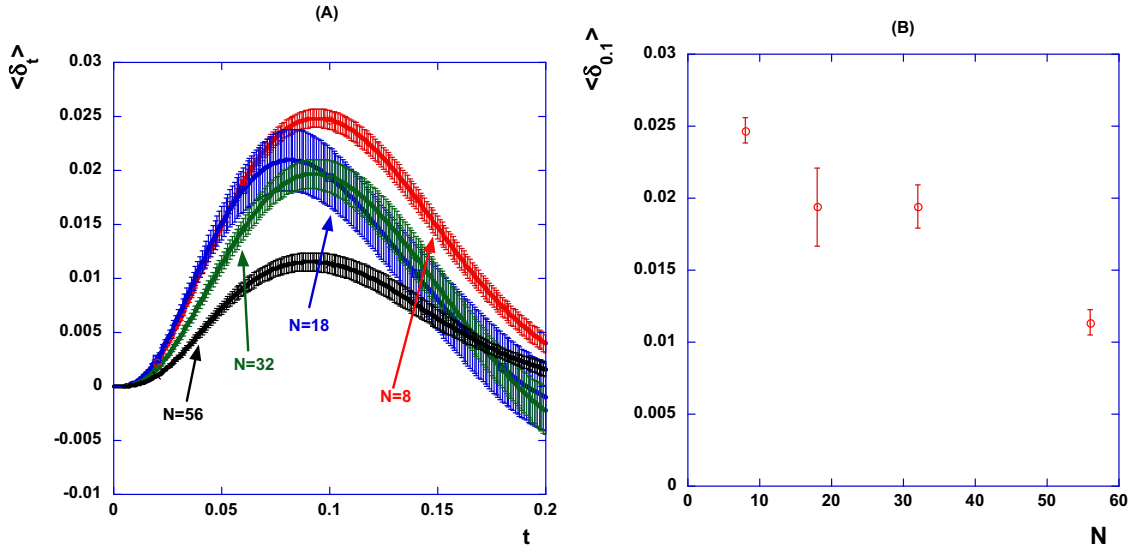


Figure 5-9 A: $\langle \delta_t \rangle$ of fluctuation path with $T_{hr} = \mu + 2.5\sigma$ for various N . **B:** $\langle \delta_t \rangle$ at arbitrary time $t=0.1$ close to the peaks of the $\langle \delta_t \rangle$'s. These are averages of 4 runs with error bars given by the standard error in the mean.

Observation of asymmetry in large systems occurs, and computer time limitations make this unfeasible at this time. Results by [82] suggest that in the Fermi-Pasta-Ulam model the asymmetry persists in the large N limit.

5.5 Conclusions

The presence of temporal asymmetries has been confirmed in various nonequilibrium molecular dynamics simulations and adopting various methods to detect them.

Fluctuation paths have been expressed as correlation function and via transient time correlation function theory: by this means for the first time for deterministic reversible systems we have been able to theoretically justify the asymmetries that have been observed previously. It has allowed us to show that temporal asymmetries are intrinsic properties of deterministic and reversible nonequilibrium systems.

We note that all time-series, even a saw-tooth oscillation which is clearly just as asymmetric near the mean as far from it, will become symmetric if the average of the difference in the mean is taken without a conditional average (as can be inferred from formula (5.1.12)). It is clear that it is our conditional average, which serves to take averages only over the defined fluctuations paths (peaks or troughs), that is causing the asymmetry. However, we also observe that smaller thresholds result in less asymmetry. This would not be the case for saw-tooth oscillations, and indicates that the fluctuation paths close to the mean are more symmetric. $T_{hr} = \mu + 1.5\sigma$.

5.6 Appendix

Some care is required in writing the time correlation function expression in equation (5.1.9) if results for small systems are to be obtained. In reference [101], it has been shown how to obtain the transient time correlation function expression for some particular cases. Consideration of equation (7.29) of that reference provides us with a route to a more general expression:

$$\left\langle B(S^z\Gamma) \right\rangle_{eq} = \left\langle B(\Gamma) \right\rangle_{eq} + \int_0^z \left\langle B(S^u\Gamma) \Omega(\Gamma) \right\rangle_{eq} du \quad (5.1.15)$$

where

$$\Omega(\Gamma) f(\Gamma) = -\frac{\partial}{\partial \mathbf{A}} \cdot (\dot{\Gamma} f(\Gamma)) = -f(\Gamma) \frac{\partial}{\partial \mathbf{A}} \cdot \dot{\Gamma} - \frac{df(\Gamma)}{dt} + \frac{\partial f(\Gamma)}{\partial t} \quad (5.1.16)$$

and Ω is the dissipation function that appears in the Evans-Searles fluctuation relation [6]. Although equilibrium ensemble averages are used in (5.1.15) the

dynamics represented by S are the nonequilibrium dynamics. The distribution function that is used in the ensemble average in equation (5.1.15) and in the definition of (5.1.15) is the distribution function preserved by the field free dynamics, so $\partial f / \partial t = 0$ when $F_c = 0$. Interestingly, the isokinetic canonical distribution function with $\beta = \frac{1}{k_B T}$ and using $K_0 = (dN - 1 - d)k_B T / 2$ is not preserved when the usual (see Chapter 6 of [101]) color diffusion equations are employed, and terms of all order in N are considered. A more problematic, but similar, situation has been observed when μ thermostats have been employed (for more details see reference [19]) In the case of color diffusion, the problem that occurs relates to the subtraction of the streaming velocity, \mathbf{u} . If the streaming velocity was known, then it would be a constant and the distribution function could be determined as usual, giving an isokinetic equilibrium distribution function:

$$f_{EQ}(\Gamma) = \frac{e^{-\beta H_0(\Gamma)} \delta(K(\Gamma) - K_0)}{\int_{\Gamma} e^{-\beta H_0(\Gamma)} \delta(K(\Gamma) - K_0) d\Gamma} \quad (5.1.17)$$

where K_0 is the required kinetic energy and the internal energy is given by:

$$H_0(\Gamma) = K(\Gamma) + \Phi(\mathbf{q}) = \sum_i \frac{(\mathbf{p}_i - \mathbf{u})^2}{2m_i} + \Phi(\mathbf{q}) \quad (5.1.18)$$

If \mathbf{u} is not known a priori, it can be estimated as $1/N \sum_1^N c_i \mathbf{p}_i$ which fluctuates at equilibrium, even though its average is zero. This leads to a change in the phase space contraction rate that is $O_N(1)$, and no longer preserves (5.1.17) even when H_0 is redefined to account for the altered streaming term. An equilibrium distribution can

be defined, but it requires that the proportionality constant between K_0 and $k_B T$ is different.

To circumvent this problem in this paper (which does not aim to model a physical problem) we simply set $\mathbf{u} = 0$, obtaining a distribution function (5.1.17) and

thermostatting $\sum_i \frac{1}{2m_i} \mathbf{p}_i^2 = K_0 = (dN - 1 - d)k_B T/2$. A better approach if a physical

system was to be studied would be use an iterative method to determine the streaming velocity. In this Appendix we show that for this system $\Omega = -\beta J F_c V$, and hence Equation (5.1.9) follows. The equations of motion used in this chapter are given by equations:

$$\dot{\mathbf{q}}_i = \frac{\mathbf{p}_i}{m_i} \quad (5.1.19)$$

$$\dot{\mathbf{p}}_i = \mathbf{F}_i + \mathbf{i} c_i F_e - \zeta (\mathbf{p}_i - \ell) \quad (5.1.20)$$

$$\zeta = \frac{\sum (\mathbf{p}_i - \ell) \cdot (F_i + c_i F_c \mathbf{i})}{\sum (\mathbf{p}_i - \ell) \cdot \mathbf{p}_i} \quad (5.1.21)$$

Where $\ell = 1/N \sum_1^N \mathbf{p}_i$ ensures that the total momentum stays fixed.

Firstly we show that the distribution function (5.1.17) is conserved by the equilibrium equations of motion. That is, we consider

$$\frac{\partial}{\partial t} f_{EQ}(\Gamma, t) = f_{EQ}(\Gamma, t) \Lambda(\Gamma) - \beta \dot{H}_0(\Gamma) f_{EQ}(\Gamma, t) \quad (5.1.22)$$

where the quantity $\Lambda(\Gamma) = -\frac{\partial}{\partial \Gamma} \bullet \dot{\Gamma}$ is the phase space compression rate of the

system. Using the equations of motion, we can write the phase space compression rate as:

$$\Lambda(\Gamma) = (dN - d - 1)\zeta \quad (5.1.23)$$

We also find:

$$\dot{H}_0 = -JF_C V - 2\zeta K_0 = -JF_C V - (dN - 1 - d)k_B T \zeta \quad (5.1.24)$$

Clearly (5.1.22) is zero at equilibrium ($F_C = 0$).

We can now evaluate Ω using (5.1.16), that is,

$$\Omega(\Gamma) = \Lambda(\Gamma) - \beta \dot{H}_0(\Gamma) = \beta J(\Gamma) F_C V \quad (5.1.25)$$

Hence we obtain the nonlinear response given by equation (5.1.9).

Chapter Six: CONCLUSIONS

The simulations performed in this work have shown that temporal asymmetry is present in microscopic deterministic and reversible systems. Its presence has been confirmed in various nonequilibrium molecular dynamics simulations and various methods have been adopted to detect it. Temporal asymmetry is observed for non-autonomous equations of motion, such as for Couette flow, and from autonomous dynamics, such as colour diffusion.

Temporally asymmetric fluctuation paths have been observed in the Weeks-Chandler-Andersen fluid, in contrast with the results for the Lorentz gas [81], and are consistent with the results of [82]. This is an important result, that shows that temporal asymmetry is not an artifact of a stochastic model, but is a ubiquitous feature of physically realistic systems, that are deterministic and reversible. The detection of asymmetry is insensitive to the definition of fluctuation path.

The second important result obtained in this work, has been to express fluctuation paths as correlation functions: by this means for the first time we have been able to theoretically justify the presence of temporal asymmetry. Exploiting the properties of correlation function and of transient time correlation function theory we have given a first theoretical justification of the emergence of temporal asymmetry and shown for the first time that temporal asymmetries are an intrinsic property of physically realistic deterministic and reversible nonequilibrium systems. Ultimately we give a new approach to the justification of the breaking of the principle of detailed balance out of equilibrium for deterministic and reversible dynamics. In particular we have shown and justified the presence of a phenomenon (temporal asymmetry) that

constitutes another remarkable manifestation of the emergence of asymmetric behaviour in deterministic reversible systems.

Such a result assumes even more importance in light of the recent discovery of the potential applications of the emergence of temporal asymmetry in exceptional fluctuations in the nonequilibrium current generation [87]. Here temporal asymmetry in fluctuations of the noise can lead to net transport, even in absence of any other kind of asymmetry, in superconducting electronic devices [87].

Further work will be directed towards the determination of the dependence of asymmetry as a function of the field and, even more importantly, towards the study of its manifestation as the number of particles increases toward the thermodynamic limit.

Finally a future development should be the experimental validation of the theory with real nanoscale systems, resorting, for example, to experiments on optical tweezers. A “drag experiment”, where a colloidal particle is dragged by the circular translation of a particle-filled optical trap, could provide a real nonequilibrium environment analogue to our simulated one, and some initial studies have been attempted by Wang, based on an extension of the technique adopted in [8]. Technical difficulties related to the capability of measuring temporal asymmetry in nanoscale experiments and the huge amount of data necessary to detect asymmetry with statistical relevance could provide obstacles to this experimental approach, at this time.

References

1. L. Boltzmann, *Annalen der Physik* **60**, 392 (1897).
2. J. L. Lebowitz, *Physica A* **194**, 1 (1993).
3. J. L. Lebowitz, *Physics Today* **46**, 32 (1993).
4. J. L. Lebowitz, in *Physical Origins of Time Asymmetry*, edited by J. Halliwell and W. H. Zurek (Cambridge University Press, Cambridge, 1994), pp. 131.
5. J. Bricmont, *Ann. N. Y. Acad. Sci.* **775**, 131–175 (1996).
6. D. J. Evans and D. J. Searles, *Adv. Phys.* **51**, 1529 (2002).
7. G. M. Wang, E. M. Sevick, E. Mittag, D. J. Searles, and D. J. Evans, *Phys. Rev. Lett.* **89**, 050601 (2002).
8. D. M. Carberry, J. C. Reid, G. M. Wang, E. M. Sevick, D. J. Searles, and D. J. Evans, *Phys. Rev. Lett.* **92**, 140601 (2004).
9. S. Chu, *Rev. Mod. Phys.* **70**, 685 (1998).
10. T. Strick, J. Allemand, V. Croquette, and D. Bensimon, *Physics Today* **54** (October), 46 (2001).
11. E. H. Trepagnier, C. Jarzynski, F. Ritort, G. E. Crooks, C. Bustamante, and J. Liphardt, *Proc. Natl. Acad. Sci.* **101**, 15038 (2004).
12. J. Liphardt, S. Dumont, S. B. Smith, I. Tinoco, and C. Bustamante, *Science* **296**, 1832 (2002).
13. G. Hummer and A. Szabo, *Proc. Natl. Acad. Sci.* **98**, 3658 (2001).
14. C. Bustamante, J. Liphardt, and F. Ritort, *Physics Today* **58**, 43 (2005).
15. G. P. Morriss and C. P. Dettmann, *Chaos* **8**, 321 (1998).

16. D. J. Evans, W. G. Hoover, B. H. Failor, B. Moran, and A. J. C. Ladd, Phys. Rev. A **28**, 1016 (1983).
17. D. J. Evans and B. L. Holian, J. Chem. Phys. **83**, 4069 (1985).
18. C. P. Dettmann and G. P. Morriss, Phys. Rev. E, 2495 (1996).
19. J. N. Bright, D. J. Evans, and D. J. Searles, J. Chem. Phys. **122**, 194106 (2005).
20. D. J. Evans and D. J. Searles, Phys. Rev. E **50**, 1645 (1994).
21. O. Jepps, D. J. Evans, and D. J. Searles, Physica D **187**, 326 (2004).
22. E. Mittag, D. J. Searles, and D. J. Evans, J. Chem. Phys. **116**, 6879 (2002).
23. S. R. Williams, D. J. Searles, and D. J. Evans, J. Chem. Phys. **124**, 194102/1 (2006).
24. C. Jarzynski, Phys. Rev. Lett. **78**, 2690 (1997).
25. G. E. Crooks, Phys. Rev. E **60**, 2721 (1999).
26. F. Ritort, Poincaré Seminar **2**, 195 (2003).
27. Y. Oono and M. Paniconi, Prog. Theor. Phys. Suppl. **130**, 29 (1998).
28. T. Hatano and S. Sasa, Phys. Rev. Lett. **86**, 3463 (2001).
29. L. Rondoni, in *Lecture Notes in Physics* (Springer, Berlin / Heidelberg, 2002), Vol. 597, pp. 35.
30. M. I. Dykman, V. N. Smelyanskiy, D. G. Luchinsky, R. Mannella, P. V. E. McClintock, and N. D. Stein, Int. J. Bifurcat. Chaos **8**, 747 (1998).
31. M. I. Dykman, D. G. Luchinsky, P. V. E. McClintock, and V. N. Smelyanskiy, Phys. Rev. Lett. **77**, 5229 (1996).
32. A. R. Bulsara and L. Gammaitoni, Physics Today **49**, 39 (1996).

- 33. M. I. Dykman, D. G. Luchinsky, R. Mannella, P. V. E. McClintock, N. D. Stein, and N. G. Stocks, Riv. Nuovo Cimento Soc. Ital. Fis. D **17**, 661 (1995).
- 34. F. Mosset, A. R. Bulsara, and M. F. Shlesinger, J. Stat. Phys. **70**, 512 (1993).
- 35. M. Magnasco, Phys. Rev. Lett. **71**, 1477 (1993).
- 36. M. Millonas and M. I. Dykman, Phys. Lett. A **185**, 65 (1994).
- 37. S. Leibler, Nature **370**, 412 (1994).
- 38. C. R. Doering, W. Horsthemke, and J. Riordan, Phys. Rev. Lett. **72** (1994).
- 39. R. Collina, R. Livi, and A. Mazzino, J. Stat. Phys. **118**, 451 (2005).
- 40. G. L. Eyink, J. Stat. Phys. **61**, 533 (1990).
- 41. C. Landim, Ann. I. H. Poincare B **55**, 615 (1991).
- 42. C. Landim, Ann. Probab. **20**, 206 (1992).
- 43. C. Landim, *Large fluctuations for Markov processes: an application in interacting particles systems* (F. Guerra, M. I. Loffredo, C. Marchioro, 1992).
- 44. G. Jona-Lasinio, C. Landim, and M. E. Vares, Probability Theory and Related Fields **97**, 339 (1993).
- 45. L. Joel and H. Spohn, J. Stat. Phys. **95**, 333 (1999).
- 46. B. Derrida, J. L. Lebowitz, and E. R. Speer, J. Stat. Phys. **107**, 599 (2002).
- 47. L. Rondoni and G. P. Morriss, Open Syst. Inf. Dyn. **10**, 105 (2003).
- 48. T. Bodineau and B. Derrida, Phys. Rev. Lett. **92**, 180601 (2004).
- 49. D. Gabrielli, G. Jona-Lasinio, C. Landim, and M. E. Vares, Atti Conveg. Lincei **131**, 79 (1997).
- 50. L. Bertini, A. De-Sole, D. Gabrielli, G. Jona-Lasinio, and C. Landim, Phys. Rev. Lett. **94**, 030601 (2005).

51. L. Bertini, A. De-Sole, D. Gabrielli, G. Jona-Lasinio, and C. Landim, *Phys. Rev. Lett.* **87**, 040601 (2001).
52. C. Paneni, D. J. Searles, and L. Rondoni, *J. Chem. Phys.* **124**, 114109 (2006).
53. C. Paneni, D. J. Searles, and L. Rondoni, *IEEE Proceedings of the 2006 International Conference on Nanoscience and Nanotechnology, Brisbane, Australia*, Ed. C. Jagadish and G. Q.M. Lu, (July 2006), 697-700, IEEE Publication Co, Piscataway, U.S.A (2006).
54. C. Paneni, D. J. Searles, and L. Rondoni, "Temporal asymmetry of fluctuations in nonequilibrium steady states: Fluctuation Paths, correlation functions and nonlinear response theory", Preprint (2007).
55. L. Onsager, *Phys. Rev. Lett.* **37**, 405 (1931).
56. L. Onsager, *Phys. Rev. Lett.* **38**, 2265 (1931).
57. L. Onsager and S. Machlup, *Phys. Rev. Lett.* **91**, 1505 (1953).
58. L. Onsager and S. Machlup, *Phys. Rev. Lett.* **91**, 1512 (1953).
59. D. Gabrielli, G. Jona-Lasinio, and C. Landim, *Phys. Rev. Lett.* **77**, 1202 (1996).
60. D. Gabrielli, G. Jona-Lasinio, and C. Landim, *J. Stat. Phys.* **95**, 639 (1999).
61. J. W. Dufty and J. M. Rubi, *Phys. Rev. A* **36**, 222 (1987).
62. L. Rondoni and E. G. D. Cohen, *Nonlinearity* **11**, 1395 (1998).
63. J. M. Rubí and A. Pérez-Madrid, *Phys. Rev. A* **43**, 7040 (1991).
64. J. W. Dufty, J. J. Brey, and M. C. Marchetti, *Phys. Rev. A* **33**, 4307 (1986).
65. T. Taniguchi and E. G. D. Cohen, *J. Stat. Phys.* **126**, 1 (2007).

- 66. R. C. Tolman, *The Principles of Statistical Mechanics*. (Oxford University Press, 1938).
- 67. M. J. Klein, Phys. Rev. Lett. **97** (6), 1446 (1955).
- 68. R. M. L. Evans, J. Phys. A: Math. Gen. **38**, 293 (2005).
- 69. L. Bertini, A. De-Sole, D. Gabrielli, G. Jona-Lasinio, and C. Landim, J. Stat. Phys. **107**, 635 (2002).
- 70. D. G. Luchinsky and P. V. E. McClintock, Nature **389**, 463 (1997).
- 71. M. I. Dykman, P. V. E. McClintock, V. N. Smelyanski, N. D. Stein, and N. G. Stocks, Phys. Rev. Lett. **68**, 2718 (1992).
- 72. M. I. Dykman, V. N. Smelyanskiy, D. G. Luchinsky, R. Mannella, P. V. E. McClintock, and N. D. Stein, Nonlinear Phenomenon in Complex systems **2**, 1 (1999).
- 73. D. G. Luchinsky, P. V. E. McClintock, and M. I. Dykman, Rep. Prog. Phys. **61**, 889–997 (1998).
- 74. I. A. Khovanov, D. G. Luchinsky, R. Mannella, and P. V. E. McClintock, Phys. Rev. Lett. **85**, 2100–2103 (2000).
- 75. M. Arrayas, M. I. Dykman, R. Mannella, P. V. E. McClintock, and N. D. Stein, Phys. Rev. Lett. **84**, 5470 (2000).
- 76. D. G. Luchinsky, Contemporary Physics **43**, 379–395 (2002).
- 77. D. G. Luchinsky, S. Beri, R. Mannella, P. V. E. McClintock, and I. A. Khovanov, Int. J. Bifurcat. Chaos **12**, 583–604 (2002).
- 78. I. A. Khovanov, N. A. Khovanova, E. V. Grigorieva, D. G. Luchinsky, and P. V. E. McClintock, Phys. Rev. Lett. **96**, 083903 (2006).

- 79. R. Mannella, Phys. Rev. E **59**, 2479 (1999).
- 80. D. G. Luchinsky, J. Phys. A: Math. Gen. **30**, 577 (1997).
- 81. A. Gamba and L. Rondoni, Physica A **340**, 274 (2004).
- 82. C. Giberti, L. Rondoni, and C. Vernia, Physica A **365** (1), 229 (2006).
- 83. P. Gaspard, "Time asymmetry in nonequilibrium statistical mechanics", to appear in Adv. Chem. Phys. (2006).
- 84. D. Szasz, Encyclopedia of Mathematical Sciences, Springer Verlag, Berlin (2000).
- 85. M. P. Allen and D. J. Tildesley, *Computer simulation of liquids*. (Clarendon Press, Oxford, 1987).
- 86. J. E. Bjorkholm, R. R. Freeman, A. Ashkin, and D. B. Pearson, Phys. Rev. Lett. **41**, 1361–64 (1978).
- 87. M. M. Millonas and D. R. Chialvo, Phys. Rev. E **53**, 2239 (1996).
- 88. M. G. McPhie, P. J. Daivis, I. K. Snook, J. Ennis, and D. J. Evans, Physica A **299**, 412 (2001).
- 89. A. Jachens, J. Schumacher, B. Eckhardt, K. Knobloch, and H. H. Fernhol, J. Fluid Mech. **547**, 55–64 (2006).
- 90. R. F. Blackwelder and L. S. G. Kovasznay, Phys. Fluids **15**, 1545 (1972).
- 91. G. P. Morris and D. J. Evans, Phys. Rev. A **35**, 792 (1987).
- 92. J. W. Dufty and J. A. McLennan, Phys. Rev. A **9**, 1266 (1974).
- 93. J. Lutsko and J. W. Dufty, Phys. Rev. A **32**, 3040 (1985).
- 94. A. Denisov, H. M. Castro-Beltran, and H. J. Carmichael, Phys. Rev. Lett. **88**, 243601 (2002).

95. H. B. G. Casimir, *Rev. Mod. Phys.* **17**, 343 (1945).
96. H. Ichimura, *Chinese Journal of Physics* **17**, 94 (1979).
97. D. Sanchez and M. Buttiker, *Phys. Rev. Lett.* **93**, 106802 (1979).
98. C. A. Marlow, R. P. Taylor, M. Fairbanks, I. Shorubalko, and H. Linke, *Phys. Rev. Lett.* **96**, 116801 (2006).
99. D. J. Evans, *Proceedings of NBS Conference on Nonlinear Fluid Properties*, *Physica A* **118**, 51 (1983).
100. J. D. Weeks, D. Chandler, and Andersen, *J. Chem. Phys.* **54**, 5237 (1971).
101. D. J. Evans and G. P. Morriss, *Statistical Mechanics of Nonequilibrium Liquids*. (Academic Press, New York, 1990).
102. D. J. Evans, W. G. Hoover, B. H. Failor, B. Moran, and A. J. C. Ladd, *Phys. Rev. A* **28**, 1016 (1983).
103. K. F. Gauss and J. R. Angew, *Mathematica* **4**, 232 (1829).
104. J. C. Butcher and G. Wanner, *Appl. Numer. Math.* **22**, 113 (1996).
105. A. W. Lees and S. F. Edwards, *J. Phys. C* **5**, 1921 (1972).
106. D. J. Evans, *J. Chem. Phys.* **78**, 3297 (1983).
107. B. D. Todd and P. J. Daivis, *J. Chem. Phys.* **24**, 194103 (2006).
108. B. D. Todd, D. J. Evans, K. P. Travis, and P. J. Daivis, *J. Chem. Phys.* **111**, 10730 (1999).
109. D. A. McQuarrie, *Statistical Mechanics* (Harper and Row, New York, 1976).